

## ABSTRACT

Title of Document: MINIATURIZED POWER ELECTRONIC INTERFACES FOR ULTRA-COMPACT ELECTROMECHANICAL SYSTEMS

Yichao Tang, Doctor of Philosophy, 2015

Directed By: Professor Alireza Khaligh, Department of Electrical and Computer Engineering

Advanced and ultra-compact electromechanical (EM) systems, such as kinetic energy harvesting and microrobotic systems are deemed as enabling solutions to provide efficient energy conversion. One of the most critical challenges in such systems is to develop tiny power electronic interfaces (PEIs) capable of addressing power conditioning between EM devices and energy storage units. This dissertation presents technologies and topological solutions toward fabricating miniaturized PEIs to efficiently regulate erratic power/voltage for kinetic energy harvesting and drive high-voltage actuators for microrobotic systems. High-frequency resonant-switching topologies are introduced as power stages of PEIs that allow small footprint of the circuit without suffering from switching losses. Two types of bridgeless resonant ac-dc converters are first introduced and developed to efficiently convert arbitrary input voltages into a regulated dc output voltage. The proposed topologies provide direct ac-dc power conversion with less number of components, in comparison to other resonant topologies. A 5-mm×6-mm, 100-mg, 2-MHz and 650-mW prototype is fabricated for validation of capability of converting

very-low ac voltages into a relatively higher voltage. A resonant gate drive circuit is designed and utilized to further reduce gating losses under high-frequency switching and light-load condition. The closed-loop efficiency reaches higher than 70% across wide range of input voltages and output powers. In a multi-channel energy harvesting system, a multi-input bridgeless resonant ac-dc converter is developed to achieve ac-dc conversion, step up voltage and match optimal impedance. Alternating voltage of each energy harvesting channel is stepped up through the switching LC network and then rectified by a freewheeling diode. The optimal electrical impedance can be adjusted through resonance impedance matching and pulse-frequency-modulation (PFM) control. In addition, a six-input standalone prototype is fabricated to address power conditioning for a six-channel wind panel. Furthermore, the concepts of miniaturization are incorporated in the context of microrobots. In a mobile microrobotic system, conventional bulky power supplies and electronics used to drive electroactive polymer (EAP) actuators are not practical as on-board energy sources for microrobots. A bidirectional single-stage resonant dc-dc step-up converter is introduced and developed to efficiently drive high-voltage EAP actuators. The converter utilizes resonant capacitors and a coupled-inductor as a soft-switched LC network to step up low input voltages. The circuit is capable of generating explicit high-voltage actuation signals, with capability of recovering unused energy from EAP actuators. A 4-mm  $\times$  8-mm, 100-mg and 600-mW prototype has been designed and fabricated to drive an in-plane gap-closing electrostatic inchworm motor. Experimental validations have been carried out to verify the circuit's ability to step up voltage from 2 V to 100 V and generate two 1-kHz, 100-V driving voltages at 2-nF capacitive loads.

MINIATURIZED POWER ELECTRONIC INTERFACES FOR ULTRA-COMPACT  
ELECTROMECHANICAL SYSTEMS

BY

YICHAO TANG

Dissertation submitted to the Faculty of the Graduate School of the  
University of Maryland, College Park, in partial fulfillment  
of the requirements for the degree of  
Doctor of Philosophy  
2015

Advisory Committee:  
Professor Alireza Khaligh, Chair/Advisor  
Professor Robert W. Newcomb  
Professor Isaak D. Mayergoyz  
Professor Behtash Babadi  
Professor Sung W. Lee, Dean's Representative

© Copyright by

Yichao Tang

2015

## ACKNOWLEDGEMENT

I would like to express my sincere gratitude to my advisor, Dr. Alireza Khaligh, for his guidance, supervision and encouragement throughout my thesis research and dissertation process. He not only offers me invaluable support including research topic guidance, constructive technical advices and dissertation writing instructions, but also serves on my committee to improve this work. I would like to thank my mother, Ms. Zhiqing Wu, and my father, Mr. Pengrong Tang, for their invaluable support and continuous encouragement throughout my entire education and research program. I am also grateful to the other faculty members, Dr. Robert W. Newcomb, Dr. Isaak D. Mayergoyz, Dr. Behtash Babadi, and Dr. Sung W. Lee, for their attendance of my proposal exam and dissertation defense. I would also like to thank the research group of Power Electronics, Energy Harvesting & Renewable Energies Laboratory for their help and suggestions on my technical review and preliminary research. In addition, I would like to appreciate the kindness of Dr. Sarah Bergbreiter and her research group of Micro Robotics Laboratory for accessing their research facility. This work is sponsored partly by the Maryland Industrial Partnerships (MIPS) Grant and the Minta Martin Aeronautical Research Program, which are gratefully acknowledged.

## TABLE OF CONTENTS

	Page
ACKNOWLEDGEMENT .....	ii
TABLE OF CONTENTS .....	iii
LIST OF TABLES .....	v
LIST OF FIGURES .....	vi
 CHAPTER	
1. INTRODUCTION .....	1
1.1. Description of Tiny Electromechanical Systems .....	2
1.1.1. Kinetic Energy Harvesting .....	3
1.1.2. Autonomous Mobile Microrobots .....	8
1.2. Challenges of PEI Design and Miniaturization .....	9
1.3. State of the Art of PEI Topologies for Energy Harvesting Generators .....	10
1.3.1. Voltage Rectifiers of Dual-stage AC-DC Converters .....	10
1.3.2. Single-stage AC-DC Switching Converters .....	13
1.3.3. PZ-specified Converters .....	17
1.3.4. ES-specified Converters .....	20
1.3.5. Soft-switching Converters .....	23
1.4. State of the Art of PEI Topologies for Driving High-voltage Actuators .....	25
1.4.1. Single-stage Drive Converter .....	25
1.4.2. Dual-stage Drive Converter .....	27
1.4.3. Resonant Drive Converter .....	28
1.5. Fabrication Techniques toward PEI Miniaturization .....	29
1.5.1. CMOS Technology .....	29
1.5.2. Bare Die and Chip-scale Package .....	33
1.5.3. Micro-coil and Micro-core .....	37
1.6. Thesis Objective and Contribution .....	40
1.7. Dissertation Overview .....	44
1.8. Summary .....	46
 2. MINIATURIZATION OF POWER ELECTRONIC INTERFACES FOR TINY ELECTROMECHANICAL SYSTEMS .....	 47
2.1. Design of Bridgeless Resonant AC-DC Converters .....	47
2.1.1. Circuit Description .....	47
2.1.2. Principle of Switching Operation .....	50
2.2. Circuit Analyses of Resonant AC-DC Converters .....	58
2.2.1. Steady-state Operating Characteristics .....	58
2.2.2. Electrical Stresses .....	64

2.3. Gate Drive and Controller .....	66
2.3.1. Resonant Gate Drive .....	66
2.3.2. Module On/Off Control Strategy .....	69
2.4. Testing and Discussion .....	73
2.4.1. Prototypes and Experimental Results .....	73
2.4.2. Efficiency Analyses .....	80
2.5. Summary .....	82
3. MINIATURIZED PEI DESIGN FOR MULTI-CHANNEL KINETIC ENERGY HARVESTING SYSTEMS .....	85
3.1. Electrical Model of Electromagnetic-reed Generators .....	85
3.2. Multi-channel Energy Harvesting Systems .....	87
3.3. Design of Multi-channel Energy Harvesting Power Stage .....	89
3.3.1. Multi-input Bridgeless Resonant AC-DC Converter .....	89
3.3.2. Principle of Operation .....	91
3.4. Optimal Impedance Matching .....	98
3.5. Testing and Discussion .....	103
3.5.1. Prototypes and Design Specification .....	103
3.5.2. Energy Harvesting Testbed .....	105
3.6. Summary .....	114
4. MINIATURIZED PEI DESIGN FOR AUTONOMOUS MOBILE MICROROBOTIC SYSTEMS .....	115
4.1. Operating Principle of Electrostatic Gap-closing Actuators .....	115
4.2. Design of Actuator Driving Power Stage .....	119
4.2.1. Bidirectional Resonant DC-DC Converter .....	119
4.2.2. Principle of Operation .....	121
4.2.3. Steady-state Analysis .....	124
4.3. Driving Strategies for Actuator-based Inchworm Motor .....	128
4.3.1. Voltage Driving Requirement .....	128
4.3.2. Driving Strategy with a Paralleled Topology .....	131
4.4. Testing and Discussion .....	136
4.4.1. Prototypes and Design Consideration .....	136
4.4.2. Open-loop Operation of Single Converter .....	138
4.4.3. Inchworm Motor Actuation Validation .....	142
4.5. Summary .....	147
5. CONCLUSIONS AND FUTURE WORKS.....	148
5.1. Conclusions .....	148
5.2. Future Works .....	150
BIBLIOGRAPHY .....	152
PUBLICATION .....	166

## LIST OF TABLES

	Page
1.1 Parameters of different electromagnetic generators .....	5
1.2 Parameters of different piezoelectric generators.....	6
1.3 Parameters of different electrostatic generators.....	7
1.4 Parameters of ac-dc conversion using CMOS technology .....	31
1.5 Parameters of dc-dc conversion using CMOS technology .....	32
1.6 Parameters of PEI using bare die or chip-scale package .....	36
2.1 Component parameters in resonant converter and driver .....	73
2.2 Power loss estimation of PEI .....	83
3.1 Component parameters of EMR generator and PEI .....	102
3.2 Electrical performance of PEI for multi-channel energy harvesting .....	105
3.3 Power loss estimation of PEI for multi-channel energy harvesting.....	110
4.1 Component parameters of dual-converter power stage .....	136
4.2 Comparison of power stages for driving high-voltage actuators .....	144

## LIST OF FIGURES

	Page
1.1 Equivalent circuits of generators: (a) EMA generators ( $v_{\text{mech}}$ : mechanical velocity, $m$ : proof mass, $k$ : spring stiffness, $b$ : damping, $F_{\text{mag}}$ : magnetic force, $V_{\text{EMF}}$ : EM force, $R_{\text{self}}$ : coil resistance, $L_{\text{self}}$ : self-inductance); and (b) PZ generators ( $F_{\text{mech}}$ : stress, $m$ : mass, $k$ : stiffness, $b$ : damping, $I_{\text{in}}$ : induced current, $C_p$ : shunt capacitance, $R_p$ : shunt resistance).....	4
1.2 Mock-up of a jumping microrobot.....	8
1.3 Voltage bridge rectifiers: (a) p-n junction diode rectifier, (b) diode-connected MOSFET rectifier, (c) cross coupled MOSFET rectifier, and (d) active diode rectifier.....	11
1.4 Voltage multiplying rectifiers: (a) Villard voltage multiplier, (b) Dickson voltage multiplier, and (c) bridge voltage doubler rectifier.....	12
1.5 Single-stage H-bridge ac-dc converters: (a) two-switch boost converter and (b) four-switch boost converter.....	14
1.6 Single-stage bridgeless ac-dc converters: (a) bridgeless boost converter, (b) bridgeless buck-boost converter, and (c) bridgeless switched-inductor boost converter.....	14
1.7 Single-stage bridgeless bidirectional switch ac-dc converters: (a) split output-capacitor boost converter, (b) auxiliary diode boost converter, (c) auxiliary switch boost converter, and (d) split output-capacitor buck-boost converter.....	15
1.8 Single-stage transformer-based rectifier: (a) center-tapped transformer full-wave passive rectifier, (b) center-tapped transformer full-wave phase controlled rectifier, and (c) transformer-based active boost rectifier.....	16
1.9 Resistive impedance matching converters: (a) diode full bridge followed by buck converter, (b) diode full bridge followed by buck-boost converter, (c) diode full bridge followed by flyback converter, and (d) voltage multiplier followed by buck converter.....	18
1.10 SSHI converters: (a) series-SSHI converter, (b) parallel-SSHI converter, (c) SSHI-MR converter, and (d) hybrid-SSHI converter.....	19
1.11 Rectifier free switched inductor converter.....	20
1.12 Charge constrained converters: (a) half-bridge buck converter and (b) modified flyback converter.....	21

1.13 Voltage constrained converters: (a) charge pump buck flyback converter and (b) charge pump buck-boost flyback converter .....	21
1.14 Battery constrained converters: (a) switched inductor buck-boost converter and (b) switched inductor boost converter .....	22
1.15 Soft-switching converters: (a) diode bridge cascaded with quasi-resonant dc-dc converter; (b) load-resonant ac-ac converter cascaded with diode bridge; (c) bridgeless resonant ac-dc converter .....	23
1.16 Single-stage converters: (a) a boost converter cascaded with a charge pump circuit, and (b) a bidirectional flyback converter .....	26
1.17 Dual-stage converters: (a) a cascaded boost converter followed by a half-bridge inverter, (b) a coupled-inductor boost converter followed by a half-bridge inverter, (c) a PZ transformer-based boost converter followed by a half-bridge inverter .....	28
1.18 Topologies for driving multiple EAP actuators: (a) paralleling bidirectional dc-dc switching converters, (b) a unidirectional dc-dc converter cascaded with half-bridge inverters, (c) paralleling bidirectional resonant converters .....	29
1.19 CMOS integrated circuit: (a) CMOS inverter, (b) cross-sectional schematic of two transistors and capacitors die chip, in an n-well CMOS process.....	30
1.20 Cross-sectional view of CSP: (a) lead frame based CSP, (b) rigid substrate based CSP with wire bonding, (c) rigid substrate based CSP with flip-chip, (d) flexible substrate based CSP, and (e) wafer-level CSP.....	34
1.21 2D spiral planar layouts: (a) conventional spiral, (b) conventional spiral with equal loop area, (c) interwound spiral, and (d) twin spiral .....	38
1.22 2D stacked planar layouts: (a) stacked spiral coils with same direction, and (b) multilayer coils with different directions .....	39
1.23 3D solenoid layouts: (a) micro-coil with air, (b) micro-coil with open-loop magnetic core, (c) micro-coil with closed-loop magnetic core, and (d) micro-coil with non-magnetic core .....	40
2.1 Proposed bridgeless resonant ac-dc step-up converters: (a) Type 1; (b) Type 2.....	48
2.2 Switching sub-intervals of Type 1 converter with a positive voltage input source, during one switching cycle .....	51

2.3 Switching sub-intervals for Type 2 converter with a positive voltage input source, during one switching cycle .....	52
2.4 (a) Simplified topology of Type 1 converter with a positive input voltage; (b) The voltage and current waveforms of Type 1 converter with a positive input voltage and different switching frequencies .....	54
2.5 (a) Simplified topology of Type 2 converter with a positive input voltage; (b) The voltage and current waveforms of Type 2 converter with a positive input voltage and different switching frequencies .....	56
2.6 The equivalent circuit models of Type 1 converter: (a1) corresponding to Stages I and V; (b1) Stage II; (c1) Stage III; (d1) Stage IV. The equivalent circuit models of Type 2 converter: (a2) corresponding to Stages I and V; (b2) Stage II; (c2) Stage III; (d2) Stage IV .....	58
2.7 Voltage gain characteristics of the resonant converter .....	63
2.8 Resonant gate drive circuit for Type 1 converter.....	67
2.9 Frequency response of the transfer function of the resonant tank .....	68
2.10 Block diagram of module on/off control and polarity identification for resonant switching and gating.....	70
2.11 Resonant gating signal corresponding to on/off control signal and polarity identification signal, in the case of Type 1 converter .....	71
2.12 Simulation waveforms of Type 1 converter with 2-V <sub>rms</sub> alternating input voltage, using module on/off control .....	72
2.13 Front ( $L_{r1}$ , $C_{r1}$ , $C_{r2}$ , $Q_{r1}$ and $Q_{r2}$ ) and back ( $L_{r2}$ , $D_r$ and $C_o$ ) views of 100-mg, 2-MHz experimental prototype of the proposed Type 1 resonant ac-dc converter, as well as its resonant driver and digital controller .....	74
2.14 Experimental waveforms of Type 1 converter operating with $V_{in}=3$ V (dc), $V_o=8.1$ V (dc), $R_{load}=100$ $\Omega$ , during 2-MHz switching: (a) $v_{gate}$ and $v_{gs}$ ; (b) $i_{in}$ and $V_o$ .....	76
2.15 Experimental waveforms illustrating resonant switching of Type 1 converter, during 2-MHz switching: (a) $i_{ds2}$ and $v_{ds2}$ ; (b) $i_{dr}$ and $v_{dr}$ .....	77
2.16 Voltage gain of Type 1 converter at $+3V_{dc}$ input under different load.....	78

2.17 Open-loop experimental waveforms of Type 1 converter operating with (a) $V_{in}=3 V_{rms}$ (20 Hz, ac), $V_o=7.6 V$ (dc), $R_{load}=100 \Omega$ ; (b) $V_{in}=0.25 V_{rms}$ (20 Hz, ac), $V_o=0.55 V$ (dc), $R_{load}=100 \Omega$ , during 2-MHz switching: $i_{in}$ , $v_{in}$ and $V_o$ .....	79
2.18 Closed-loop experimental waveforms of Type 1 converter operating with (a) voltage regulation for $V_o=5 V$ , $R_{load}=100 \Omega$ ; (b) module on/off control at 20-kHz modulation frequency .....	80
2.19 Closed-loop dynamic response of Type 1 converter operating with voltage regulation for $V_o=5 V$ , $R_{load}=100 \Omega$ .....	80
2.20 Open-loop output power and efficiency over input voltage of Type 1 converter at (a) $R_{load}=100 \Omega$ ; and (b) $R_{load}=500 \Omega$ .....	82
2.21 Closed-loop efficiency over (a) input voltage (at $P_{out}=0.25 W$ ); and (b) output power (at $V_{in}=3 V_{rms}$ ) .....	82
3.1 Equivalent circuit of one EMR generator ( $v_{mech}$ : mechanical velocity; $m$ : proof mass; $k$ : spring stiffness; $D_p$ : mechanical damping; $F_{mag}$ : magnetic force; $v_{emf}$ : EMF; $r_{EMR}$ : coil resistance; $L_{EMR}$ : self-inductance; $i_{EMR}$ : generator terminal current; $v_{EMR}$ : generator terminal voltage) .....	86
3.2 Multiple EMR generators and PEI system: (a) conventional PEI; and (b) proposed multi-input PEI.....	88
3.3 Impedance network of an EMR generator interfaced with (a) a diode bridge; and (b) a single-input resonant ac-dc converter ( $Z_r$ : characteristic impedance; $R_{load}$ : load resistance; $Z_{in}$ : equivalent input impedance).....	89
3.4 Illustrative scheme of the proposed multi-input converter ( $v_{emf}^{(i)}$ : EMF of #i channel; $r_{EMR}^{(i)}$ : coil resistance; $L_{EMR}^{(i)}$ : self-inductance; $i_{EMR}^{(i)}$ : channel terminal current; $v_{EMR}^{(i)}$ : channel terminal voltage; $C_{r1}^{(i)} = C_{r2}^{(i)}$ : resonant capacitors; $L_r$ : resonant inductor; $Q_{r1}^{(i)}$ , $Q_{r2}^{(i)}$ : MOSFETs; $D_r$ : output diode; $C_o$ : output capacitor) .....	90
3.5 (a) Simplified topology of dual-input resonant converter with a positive input and a negative input; (b)~(d) switching sub-subintervals during a switching cycle .....	93
3.6 Simulation waveforms of dual-channel system during a switching cycle .....	94
3.7 Switching average model of an $N$ -channel system .....	98
3.8 (a) An $N$ -channel EMR generator system connected with an $N$ -input resonant ac-dc converter; and (b) impedance network of an $N$ -channel system .....	99

3.9 Illustrative scheme of the MPPT control strategy and gate drive .....	101
3.10 Simulation waveforms of a six-input converter connected to a resistive load.....	102
3.11 Six-input standalone prototype of the proposed resonant ac-dc converter for a six-EMR-generator system.....	103
3.12 Experimental waveforms of switching operation: $v_{emf} = 1$ V, $f_s = 48$ kHz; X-axis: 4 $\mu$ s/div; Y-axis: (a) Ch1 = gate voltage of $Q_{r1}$ , 2 V/div; Ch3 = drain-to-source voltage ( $v_{qr1}$ ) of $Q_{r1}$ , 2.5 V/div; ChM = diode voltage ( $v_{dr}$ ) of $D_r$ , 5 V/div; (b) Ch1 = gate voltage of $Q_{r1}$ , 2 V/div; Ch2 = output voltage ( $V_o$ ), 2 V/div; Ch3 = input current ( $I_{EMR}$ ) of one input, 20 mA/div; Ch4 = inductor voltage ( $v_r$ ), 5 V/div; and (c) $f_s = 200$ kHz, Ch1 = gate voltage of $Q_{r1}$ , 2 V/div; Ch3 = drain-to-source voltage ( $v_{qr1}$ ) of $Q_{r1}$ , 2.5 V/div; Ch4 = inductor voltage ( $v_r$ ), 5 V/div; ChM = diode voltage ( $v_{dr}$ ) of $D_r$ , 5 V/div .....	107
3.13 Experimental waveforms of power amplifiers: $f_{in} = 20$ Hz; X-axis: 10 ms/div; Y-axis: (a) $v_{emf} = 3$ V <sub>rms</sub> ; Ch1 = output voltage ( $V_o$ ), 2.5 V/div; Ch2 = terminal voltage ( $v_{EMR}$ ) of channel #1, 10 V/div; Ch3 = input current ( $i_{EMR}$ ) of six channels, 50 mA/div; and (b) $v_{emf} = 0.5$ V <sub>rms</sub> ; Ch1 = output voltage ( $V_o$ ), 0.5 V/div; Ch2 = terminal voltage ( $v_{EMR}$ ) of channel #1, 5 V/div; Ch3 = sum of the input currents ( $i_{EMR}$ ) of six channels, 10 mA/div .....	109
3.14 Experimental waveforms of power amplifiers with step change: X-axis: 40 ms/div; Y-axis: (a) $v_{emf} =$ from 1 V <sub>rms</sub> to 2 V <sub>rms</sub> ; Ch1 = output voltage ( $V_o$ ), 1 V/div; Ch2 = terminal voltage ( $v_{EMR}$ ) of channel #1, 5 V/div; Ch3 = input current ( $i_{EMR}$ ) of six channels, 50 mA/div; and (b) $f_{in} =$ from 20 Hz to 50 Hz; Ch1 = output voltage ( $V_o$ ), 0.5 V/div; Ch2 = terminal voltage ( $v_{EMR}$ ) of channel #1, 5 V/div; Ch3 = input current ( $i_{EMR}$ ) of six channels, 50 mA/div .....	110
3.15 Power conversion efficiency of the power stage and the entire PEI (including controller losses) at different output power.....	112
3.16 Experimental waveforms of EMR generators: X-axis: (a) 20 ms/div; (b) 100 ms/div; Y-axis: (a) constant wind speed; (b) wind speed step change; Ch1 = terminal voltage ( $v_{EMR}$ ) of channel #2, 5 V/div; Ch2 = output voltage ( $V_o$ ), 1 V/div; Ch3 = terminal voltage ( $v_{EMR}$ ) of channel #1, 10 V/div; Ch4 = input current ( $i_{EMR}$ ) of channel #1, 10 mA/div .....	113
4.1 Mechanism of in-plane electrostatic gap-closing actuators (GCA) at one side of the shuttle.....	117

4.2 Electrostatic inchworm motor driven by two anti-phase drive signals.....	118
4.3 Proposed bidirectional resonant dc-dc converters for driving EAP actuators ..	120
4.4 a-(I)~a-(III) Equivalent circuits corresponding to the switching sub-intervals during boost operation (driving actuators); b-(I)~b-(III) equivalent circuits corresponding to the switching sub-intervals during buck operation (energy recovery) .....	122
4.5 The voltage and current waveforms of the proposed converter during (a) boost mode (actuator drive), and (b) buck mode (energy recovery) .....	123
4.6 Equivalent circuit model of each switching sub-interval. (a) equivalent circuit corresponding to Stage I (boost) and Stage II (buck); (b) equivalent circuit corresponding to Stage II (boost) and Stage I (buck); (c) equivalent circuit corresponding to Stage III (boost) and Stage III (buck) .....	125
4.7 Steady state average model for the converter connected with a resistive load.....	128
4.8 Paralleled topology for driving multiple EAP actuators.....	130
4.9 Alternative strategy for driving electrostatic multi-GCA inchworm motor .....	132
4.10 Logical flow chart of the alternative driving strategy during a half driving cycle .....	134
4.11 Simulation waveforms during one cycle of driving the electrostatic inchworm motor.....	135
4.12 Front ( $L_{in}$ , $C_{r1}$ , $C_{r2}$ , $Q_{r1}$ and $Q_{r2}$ ) and back ( $L_p$ and $L_s$ ) views of 100-mg, 1.5-MHz experimental prototype of the paralleled resonant dc-dc converters, as well as its driver and controller.....	136
4.13 Experimental waveforms operating with $V_{in}=2$ V, $V_o=100$ V, $R_{load}=16.8$ k $\Omega$ , during 1.5-MHz switching: (a) $i_{in}$ , $V_{in}$ and $V_o$ ; (b) the current $i_{ds1}$ and voltage $v_{ds1}$ of transistor $Q_{r1}$ ; (c) the current $i_{dq2}$ and voltage $v_{dq2}$ of body diode $D_{q2}$ .....	140
4.14 Conversion efficiency versus output power of the resonant converter at different output drive voltages: (a) boost mode; (b) buck mode .....	141
4.15 Input power demands of the converter at different driving frequencies and load capacitances .....	142

4.16 Electrostatic actuator driving test by utilizing the adopted PEI driver (500 mW, 63 mg, 31.5 mm <sup>2</sup> ) and its controller .....	143
4.17 SEM image of the electrostatic actuators for inchworm motor .....	144
4.18 Dynamic driving performance of two sets of GCAs during one alternative driving cycle.....	146
4.19 Dynamic motion of the shuttle of the inchworm motor during alternative driving process .....	147

## CHAPTER 1

### INTRODUCTION

Nowadays, advanced and ultra-compact electromechanical (EM) systems are utilized in various systems where both mechanical motion and electrical energy are required, such as automation, electricity meters, wireless sensors, kinetic energy harvesting and tiny robotic systems [1], [2]. In majority of modern applications, the utilization of EM devices can be classified into two categories: (1) EM generators or transducers that generate electricity to feed the loads or energy storage units; and (2) EM actuators or motors that need power supply from energy storage units to generate mechanical deformation [1]-[5]. The miniaturized power electronic interfaces (PEIs) need to be introduced and designed due to the necessity of developing tiny circuits for addressing power conditioning of EM devices.

One of the challenges toward developing advanced EM systems is the electrical compatibility among the system components, including energy storage units, electrical loads and EM devices. Majority of energy storages, such as battery cells and ultra-capacitors, have dc voltage outputs [6]. However, in the case of EM generators, the induced voltage is usually tiny, irregular, abrupt and alternating [3], [4], [7]. As for EM actuators, the voltage requirements for mechanical deformation are high, pulsatile and complicated [5], [8]. Therefore, a strong demand of developing circuitry interfaces for EM systems stems from the requirement of friendly electrical connections among system components.

Secondly, there is a motivation to scale down the EM systems into micro or meso level through miniaturization and integration of mechanical and electrical components.

Advanced electromechanical technologies, including electromagnetism and electroactive polymers, have been developed toward fabricating microelectromechanical systems (MEMS) and mesoelectromechanical systems that can be installed in very tiny spaces, such as mobile phone, MP3, electrical watch, medical pill camera and microrobotic insects [9]-[11]. Hence, the development of miniaturized PEI is of critical importance and emergence for miniaturization and integration of an ultra-compact EM system.

### **1.1 Description of Tiny Electromechanical Systems**

Electromechanics is a hybrid engineering combining electrical and mechanical processes and procedures. Typically, an electromechanical (EM) device is capable of carrying out the energy conversion between mechanical motion and electric power [2]. One EM device can either serve as an electrical generator or transducer that converts the mechanical motion of its moving parts into electricity; or, in a reversal direction, it performs as a mechanical actuator or motor that generates mechanical deformation by absorbing electric power [3]-[5].

Microelectromechanical systems (MEMS) and mesoelectromechanical systems have emerged from a strong demand for fabricating very tiny systems that can be installed in very limited spaces [2], [9]-[11]. EM devices at micro-scale range in size from 20 micrometers to 1 millimeter while those at meso-scale range in size from 1 millimeter to tens of millimeters. Advanced technologies toward fabricating miniature electromechanism, including electromagnetism, piezoelectricity, electrostatics, electrostriction, dielectric elastomer, etc., give rise to the popularity of tiny EM systems, such as implantable and wearable electronic devices, wireless network sensors and nodes, as well as autonomous mobile microrobots [12]-[14].

### **1.1.1 Kinetic Energy Harvesting**

For wearable electronic devices or self-powered wireless sensors, the bulky size of batteries and the difficulty to access them introduce a strong demand of replacing batteries with alternative power sources. Many renewable energy sources, including solar cells, micro-fuel cells, microturbine generators, etc., are introduced to serve as potential alternatives for electronic devices with smaller batteries or being battery free. Among these power source candidates, the kinetic energy harvesting has superiorities in terms of being clean, stable, available, and of small size [15]. In the majority of ambiences, kinetic energy exists in the form of vibration, regular and random displacements.

Kinetic energy generators are intended to convert mechanical movement present in the ambient vibration sources into electrical energy [16]. Typically, electromagnetic (EMA) and electroactive polymer (EAP) (including piezoelectric (PZ), electrostatic (ES) and dielectric elastomer) transduction mechanisms are used to convert kinetic energy into electricity [12]. These transducers or generators are generally composed of a stator anchored on the external holder and a proof mass physically connected to the stator through a mechanical damper [14]-[18]. The damper can generate a relative movement between the stator and the proof mass when an external force is applied on the stator. Therefore, an alternative potential is induced through the relative movement and electricity is delivered to the electrical loads.

EMA generators or micro EMA generators are based on the principle of Faraday electromagnetic induction [4]. Majority of EMA generators are inertial harvesters, where the mechanical energy is transduced through the inertia of proof mass. The acceleration of proof mass as a result of the mechanical damper generates a relative movement

between the winding coils and the permanent magnets. The coils cut the magnetic flux of permanent magnets, which induces an electromotive force (EMF) on the coil. Therefore, the current is generated when an electrical load is connected with the coils. In electrical domain, the equivalent model of an EMA generator, illustrated in Fig. 1.1(a), can be presented as a bipolar time-varying EMF ( $V_{EMF}$ ), a series internal resistance ( $R_{self}$ ) and a series self-inductance ( $L_{self}$ ) [18]. EMA generators have the advantages in terms of low output impedance (small resistance and inductance) and high output current; however, the output voltage is usually low [19]-[33].

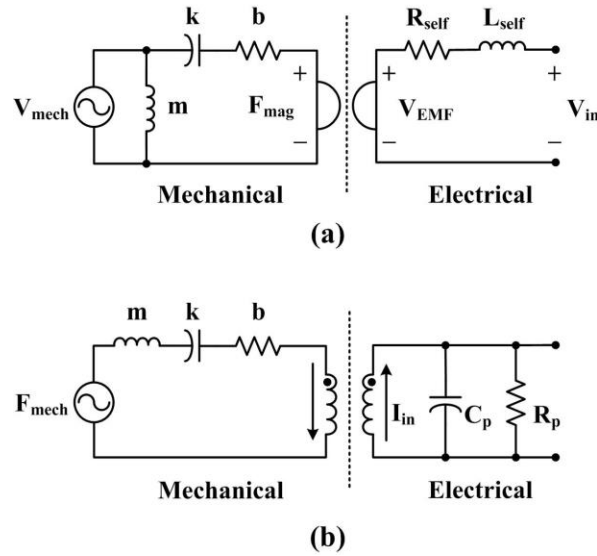


Figure 1.1. Equivalent circuits of generators: (a) EMA generators ( $v_{mech}$ : mechanical velocity,  $m$ : proof mass,  $k$ : spring stiffness,  $b$ : damping,  $F_{mag}$ : magnetic force,  $V_{EMF}$ : EM force,  $R_{self}$ : coil resistance,  $L_{self}$ : self-inductance); and (b) PZ generators ( $F_{mech}$ : stress,  $m$ : mass,  $k$ : stiffness,  $b$ : damping,  $I_{in}$ : induced current,  $C_p$ : shunt capacitance,  $R_p$ : shunt resistance) [18].

Tale 1.1 lists the prototype parameters of published EMA generators. The majority of EMA generators have volumes less than tens of centimeter cube and power capability above hundreds of micro watts. However, their output voltages range from 0.1

$V_{\text{rms}}$  to  $1 V_{\text{rms}}$  with optimum loads. Therefore, the voltage rectification is challenged as a result of the low generated voltage close to  $0.3 \cdot V_{\text{dc}}$  diode forward voltage.

TABLE 1.1  
PARAMETERS OF DIFFERENT ELECTROMAGNETIC GENERATORS

Reference	Output Power ( $\mu\text{W}$ )	Volume ( $\text{mm}^3$ )	Output Voltage ( $V_{\text{rms}}$ )	Frequency (Hz)	Fabrication
[19]	$380 \times 10^3$	/	0.7~3.5	2~10	non-MEMS
[20]	$8.5 \times 10^3$	/	0.5	5	non-MEMS
[21]	$7 \times 10^3$	$7.5 \times 10^3$	0.14	95	non-MEMS
[22]	$5 \times 10^3$	$69 \times 10^3$	0.1	54	non-MEMS
[23]	$2.46 \times 10^3$	$12.7 \times 10^3$	0.7	8	non-MEMS
[24]	830	$2 \times 10^3$	1	66	MEMS
[25]	750	$10 \times 10^3$	1.9	45	non-MEMS
[26]	545	$2.96 \times 10^3$	0.089	10	non-MEMS
[27]	400	200	0.3	25	non-MEMS
[28]	315	$8 \times 10^3$	1	78	non-MEMS
[29]	46	300	0.43	52	non-MEMS
[30]	5.6	170	0.07	383	MEMS
[31]	0.55	660	$14 \times 10^{-3}$	242	MEMS
[32]	$4 \times 10^{-3}$	600	$6 \times 10^{-3}$	50	MEMS
[33]	$0.12 \times 10^{-3}$	100	$1.4 \times 10^{-3}$	115	MEMS

PZ generators are smart materials that can generate a potential during expansion or suppression. Majority of PZ generators are direct force-driven harvesters, where mechanical energy is transduced by a directly applied force [34]-[44]. The external force ( $F_{\text{mech}}$ ) results in a deformation of the material that induces a potential on two electrode

sides and delivers the electric charge to the load. Bimorph cantilevers structures with intrinsic frequencies in a few hundred Hertz, are the most widespread PZ harvester structures. PZ bimorphs with two PZ layers mounted on a ceramic or metallic layer behave like a capacitor and are able to accumulate electric charges. In electrical domain, the model of a PZ generator, depicted in Fig. 1.1(b), is usually simplified as a bipolar time-varying current source ( $I_{in}$ ) with a shunt capacitor ( $C_p$ ) and a shunt resistor ( $R_p$ ) [18]. Generally, the induced bipolar time-varying potential of a PZ generator has high amplitude due to its high capacitive impedance. However, the high output impedance of capacitor reduces the output current and makes it difficult to extract maximum power.

The prototype parameters of different PZ generators are listed in Table 1.2. The output voltages of most PZ generators are higher than those of EMA generators; however, the power densities of PZ generators are relatively low. Therefore, the rectification efficiency becomes critical, especially at light-load condition.

TABLE 1.2  
PARAMETERS OF DIFFERENT PIEZOELECTRIC GENERATORS

Reference	Output Power ( $\mu\text{W}$ )	Volume ( $\text{mm}^3$ )	Output Voltage ( $V_{\text{rms}}$ )	Frequency (Hz)	Fabrication
[34]	$45 \times 10^3$	$200 \times 10^3$	40	100	non-MEMS
[35]	$3 \times 10^3$	$2.28 \times 10^3$	10	1	non-MEMS
[36]	98	186	1~3	/	non-MEMS
[37]	85	60	1.7	325	MEMS
[38]	60	0.58	1~3.5	572	MEMS
[39]	3.98	200	1.4	200	MEMS
[40]	2.765	0.38	0.6	256	MEMS
[41]	2.15	0.65	0.11	461	MEMS
[42]	2.1	264.5	0.2~1.2	80	non-MEMS

[43]	1.1	1	1.5	528	MEMS
[44]	0.53	16	0.16	42	MEMS

An ES generator is essentially a capacitor whose capacitance changes by moving its electrode plates. Initially, an amount of energy is stored in the ES generator as a result of a potential on two electrode plates. The capacitance decreases as soon as the external force increases the distance between electrode plates. Therefore, the electric charge is pumped to the load. The generator can restore the mechanical energy when the electrode plates return to the initial positions. The ES generators also have high output voltage; nevertheless, they require initial charge for starting [45]-[49]. Unlike those EMA and PZ generators, majority of ES generators generate unipolar time-varying voltages. The prototype parameters of ES generators, listed in Table 1.3, show that the rectification of ES generators has both challenges in terms of low-voltage rectification and light-load efficiency.

TABLE 1.3  
PARAMETERS OF DIFFERENT ELECTROSTATIC GENERATORS

Reference	Output Power ( $\mu\text{W}$ )	Volume ( $\text{cm}^3$ )	Output Voltage ( $\text{V}_{\text{rms}}$ )	Frequency (Hz)	Fabrication
[45]	400	25	/	6	MEMS
[46]	38	200	35	20	MEMS
[47]	5.5	30	0.6~1.2	1500	MEMS
[48]	1	17.3	0.35~1.5	596	MEMS
[49]	0.061	62	2	250	MEMS

### 1.1.2 Autonomous Mobile Microrobots

Autonomous mobile microrobots (defined as robots with millimeter-scale dimensions) can provide high maneuverability and access to spaces that are otherwise inaccessible due to their ultra-compact sizes [5], [8], [13]. Microrobots have numerous applications ranging from exploring environmental hazards, disaster relief, exploiting underground mines, microsurgery, and surveillance [13]. To perform these kind of tasks, microrobots will require 1) mechanisms like legs or wings to interface with the environment and move the robot forward, 2) actuator to move these mechanisms, 3) sensors and controllers to tell the robot where to go and how to move, and 4) tiny power supplies and electronics to provide energy to the actuators and robot, as shown in Fig. 1.2. Significant progress has been made toward fabricating microrobot mechanisms including both microelectromechanical systems (MEMS) approaches [9], [10] and non-MEMS approaches [11].

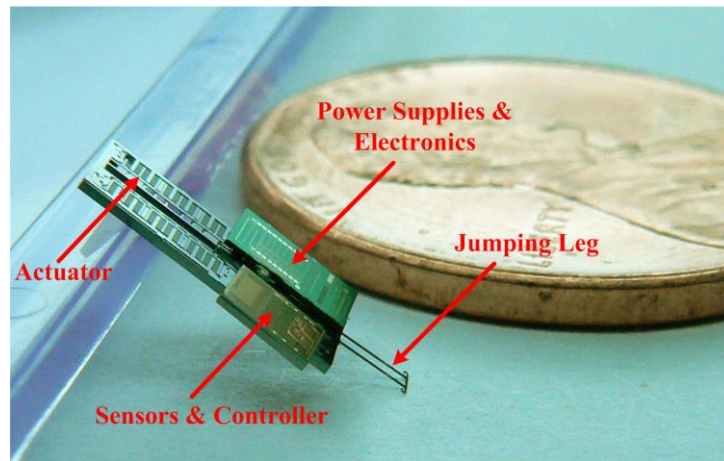


Figure 1.2. Mock-up of a jumping microrobot [112].

Unlike conventional robots, which are mostly driven by electromagnetic motors and solenoids [50], microrobots are driven through various dielectric electroactive

polymer (EAP) actuation schemes, including electrostatic [8], [51], piezoelectric [9], [52], electrostrictive and dielectric elastomer actuators [53]. Each type of actuation scheme has its unique advantages in terms of size, actuation strain, work/power density and efficiency [5]. A common inherent characteristic of EAP actuators is their capacitive nature. Depending on the applied voltage across these actuators, their capacitance changes and they compress or expand. Such deformation of actuators is used to create mechanisms like movement of artificial legs or wings in microrobots.

## **1.2 Challenges of PEI Design and Miniaturization**

Miniature power electronic interfaces (PEIs) are intended to address power conditioning for various types of low-voltage energy sources, such as tiny energy generators [3], and low-profile loads, such as microrobotic actuators [5]. Power density and light-load efficiency are important performance metrics of power converters, especially for low power applications. One of the main challenges toward fabricating ultra-compact power conditioning system is the miniaturization of PEIs with given energy storage and loss limitation of passive components [54]. An effective approach toward miniaturization requires the size and weight of semiconductors, inductive and capacitive components to be reduced through both topology design and fabrication process. Furthermore, energy conversion efficiency is of critical importance in low power PEI designs. Power loss reductions in transistors, passive components and gate drivers are challenging, due to small load and limited footprint.

In the case of low-power energy harvesting, the rectification of low-amplitude input voltage sources, such as electromagnetic (EMA) generators and electroactive polymer (EAP) generators, is difficult, inefficient, and in some cases impractical, to be

implemented by using conventional diode-bridge topologies. The forward voltage on diodes causes large amount of power loss, which in turn significantly lowers the power conversion efficiency.

As for microrobotic, the challenge of PEI design stems from the fact that most of efficient EAP actuation operate at high voltage. However, the output voltage of suitable on-board energy sources including chemical battery cells, super-capacitors, fuel cells, and solar cells is generally less than 5 V; in comparison, the typical driving voltage of EAP actuators is an order of magnitude higher than 5V. Therefore, a power converter with high step-up voltage-gain is required to place between the energy sources and the actuators. On the other hand, the light-load efficiency of a miniaturized PEI draws significant attention. Power losses are more serious in on-board PEI due to the miniature component size, light-load operation and unused energy stored in actuators.

### **1.3 State of the Art of PEI Topologies for Energy Harvesting Generators**

#### **1.3.1 Voltage Rectifiers of Dual-stage AC-DC Converters**

Typically, dual-stage power converters are utilized to address the electric power generated by electromagnetic (EMA) and piezoelectric (PZ) generators [54]. The first stage is a rectifier to convert an alternating time-varying voltage to a dc voltage while the second stage is a dc-dc converter to regulate the output voltage/current. Due to the fixed forward voltage of diodes (typically equal to 0.7V, or 0.3V for Schottky diode), using conventional diode bridge as the first stage is difficult and inefficient for low-amplitude voltage rectification of majority of EMA or PZ generators (see Fig. 1.3(a)). A full-wave diode bridge has twice of the diode forward voltage, which makes it impractical to

address the low-amplitude alternating voltage. Therefore, low-forward-voltage rectifiers are investigated for efficient rectification.

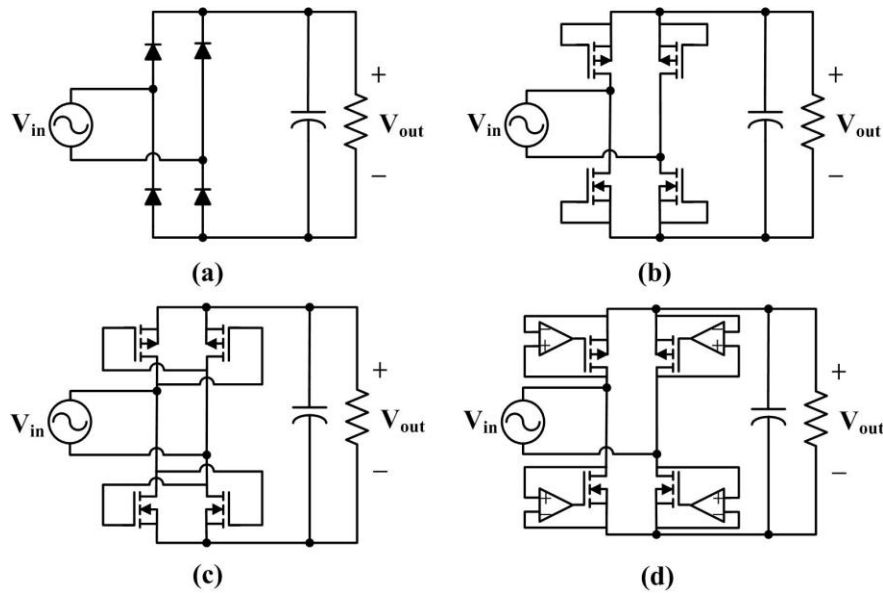


Figure 1.3. Voltage bridge rectifiers: (a) p-n junction diode rectifier, (b) diode-connected MOSFET rectifier [55], (c) cross coupled MOSFET rectifier [56], [57], and (d) active diode rectifier [58], [59].

One of the efforts is to replace the conventional p-n junction diode with diode-connected MOSFETs (see Fig. 1.3(b)) [55]. It can be achieved by connecting the gate node of one MOSFET to the source node of itself. As a result, the forward voltage is close to the MOSFET gate threshold voltage. However, a full-wave rectifier still suffers from the twice of MOSFET gate threshold voltage. Another effort is to utilize gate cross-coupled MOSFET pair instead of diode in each bridge leg, shown in Fig. 1.3(c) [56], [57]. The gate node of one MOSFET is connected to the drain node of another MOSFET of another leg. The MOSFET gates are passively driven by the large voltage swing at the drain node of another leg. Therefore, a forward voltage, lower than gate threshold voltage, can be acquired. However, the turn-on resistance of MOSFET is doubled by cross-

coupled MOSFET pair, resulting in additional voltage drop at turn-on resistance. In addition, the current may flow back to the input source if the input voltage is lower than the MOSFET threshold voltage.

Active diode, capable of eliminating the forward voltage, is another alternative for rectification. An active diode consists of a MOSFET and a comparator, where the MOSFET drain node is connected to the comparator anode, the source node to the cathode, and the gate node to the output (see Fig. 1.3(d)) [58], [59]. The MOSFET is turned on or off by the comparator which compare the drain and source voltage of MOSFET. This method eliminates the forward voltage caused by threshold voltage while leading to a low turn-on resistance. However, additional dc power supply is required to feed the comparator, which results in a startup circuit and increases power consumption.

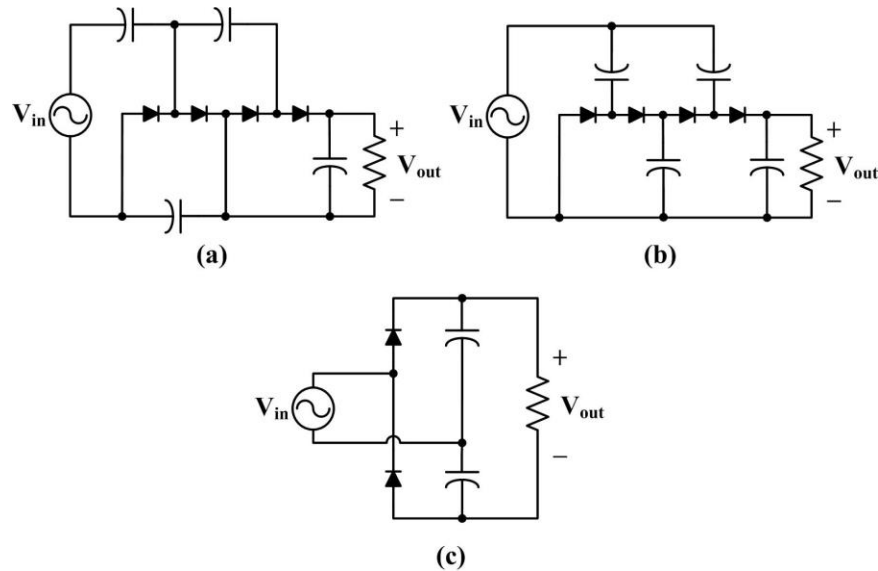


Figure 1.4. Voltage multiplying rectifiers: (a) Villard voltage multiplier [60], (b) Dickson voltage multiplier [61], and (c) bridge voltage doubler rectifier [62].

In addition to the bridge rectifiers, other research efforts focus on developing voltage multiplying rectifiers composed of capacitor and diode pairs. Villard and Dickson

voltage multipliers are the most commonly used topologies which share the same principle of operation, illustrated in Fig. 1.4 (a) and (b) [60], [61]. When the input generator's alternating voltage is at negative cycle, half of the diode string conducts and the input source charges the capacitors at high side of diode string. When the input voltage is at positive cycle, another half of the diode string conducts and the pre-charged capacitors at high side of diode string release the charge to the output at low side of diode string. As a result, the input voltage is multiplied by the capacitor pairs. Additionally, Fig. 1.4(c) demonstrates the bridge voltage doubler which is also capable of double the input voltage [62]. Although these topologies multiply the input voltage, they still suffer from the forward voltage of diode string. Furthermore, the large number of capacitor and diode pairs increases the circuit size.

### 1.3.2 Single-stage AC-DC Switching Converters

Despite of efforts on forward voltage reduction, all those voltage rectifiers are passive converters that thereby require a second stage to regulate the output voltage and current. Nevertheless, the dual-stage converter is inherently inefficient in comparison to the single-stage converter. Therefore, single-stage ac-dc switching converters that provide ac-dc conversion along with voltage/current regulation are investigated.

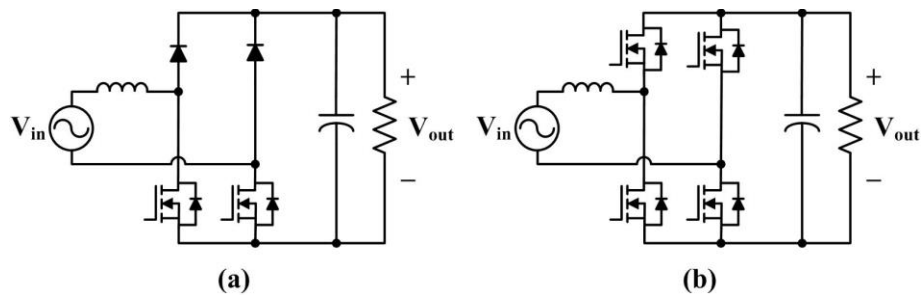


Figure 1.5. Single-stage H-bridge ac-dc converters: (a) two-switch boost converter [63] and (b) four-switch boost converter [64].

Two-switch and four-switch H-bridge ac-dc boost converters are the most commonly used topologies, presented in Fig. 1.5 (a) and (b) [63], [64]. When the low-side switches are turned on, the input source charges the input inductor; when one of the low-side switches is turned off, the inductor releases the energy to the output through the high-side diode. However, there are always two semiconductors in the current close loop during the charging and discharging of inductor, which increases the conduction losses. Moreover, each MOSFET operates in reverse conduction mode for half of operation period that increases the overall turn-on resistance.

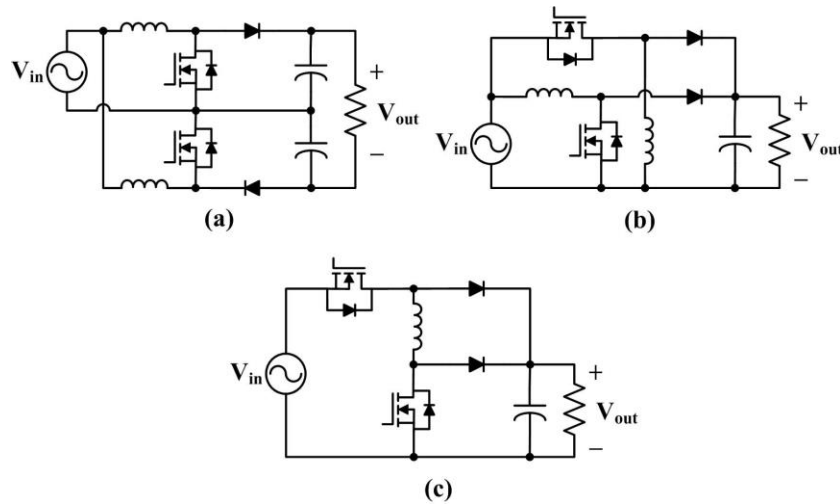


Figure 1.6. Single-stage bridgeless ac-dc converters: (a) bridgeless boost converter [65], (b) bridgeless buck-boost converter [66], and (c) bridgeless switched-inductor boost converter [67].

To overcome the disadvantages of H-bridge converters, single-stage bridgeless ac-dc converters are investigated, including ac-dc boost converter, ac-dc buck-boost converter, and ac-dc switch-inductor boost converter. Topologically, these converters parallel two dc-dc converters to condition alternating input voltage sources. During each cycle of input voltage, the converter operates as a dc-dc converter. The ac-dc boost

converter presented in Fig. 1.6(a) parallel two boost converters with two individual output capacitors [65]. In order to reduce the number of output capacitors, the ac-dc buck-boost converter illustrated in Fig. 1.6(b) is developed through paralleling a boost converter with a buck-boost converter [66]. The work is continuously improved by eliminating one inductor in the switch-inductor ac-dc boost converter shown in Fig. 1.6(c) [67]. However, the asymmetrical operation of two different converters (i.e. continuous input current of boost converter, discontinuous input current of buck-boost converter) increases the control complexity and instability issues.

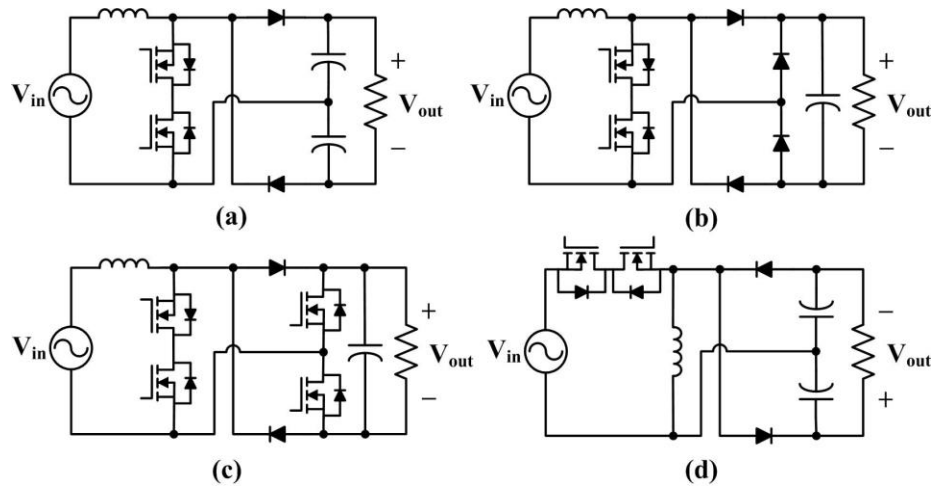


Figure 1.7. Single-stage bridgeless bidirectional switch ac-dc converters: (a) split output-capacitor boost converter, (b) auxiliary diode boost converter, (c) auxiliary switch boost converter, and (d) split output-capacitor buck-boost converter [68]-[70].

Using bidirectional switches is another approach toward bridgeless ac-dc converters. A bidirectional switch is achieved by connecting two MOSFETs (either P-channel or N-channel MOSFET) in series. The parasitic body diodes of two MOSFETs are opposite to each other that blocks the bias current through body diodes. Two MOSFETs are turned on and off simultaneously. Due to the MOSFET bidirectional

conducting capability, the current can flow through two MOSFETs back and forth. Bridgeless ac-dc boost and buck-boost converters using bidirectional switches are investigated (see Fig. 1.7(a)-(d)) [68]-[70]. Although these converters only use one inductor as switching energy storage, they all require additional components at the output. In addition, these converters demand high-side drive of MOSFETs, which complicates the gate driver design.

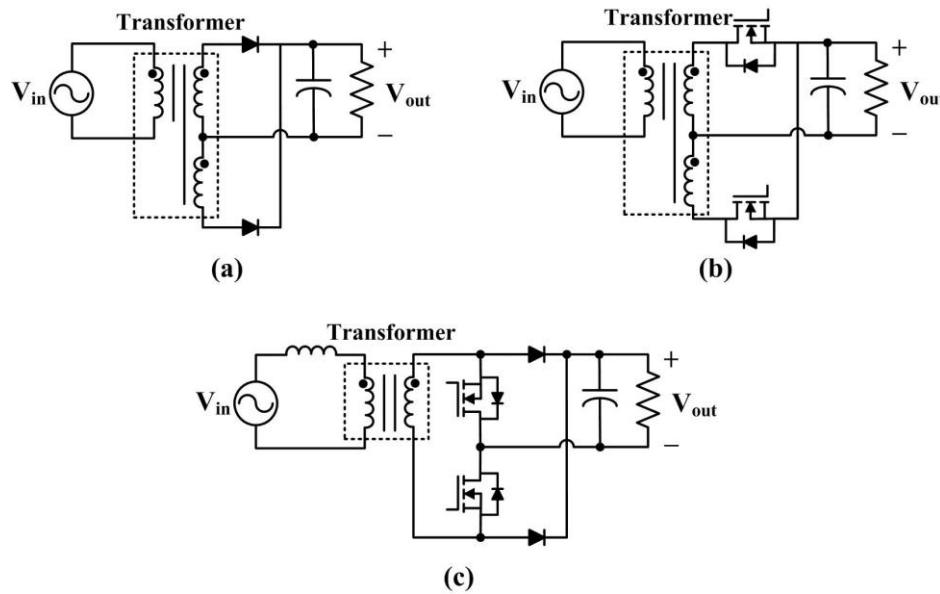


Figure 1.8. Single-stage transformer-based rectifier: (a) center-tapped transformer full-wave passive rectifier, (b) center-tapped transformer full-wave phase controlled rectifier [71], and (c) transformer-based active boost rectifier [72].

Single-stage transformer-based rectifiers, that use front-end transformers to step up the voltage, are developed by other research groups. In a center-tapped transformer passive rectifier, the generator voltage is first stepped up through the transformer and then rectified by the secondary diode bridge, as shown in Fig. 1.8(a). However, the passive rectifier is not able to regulate the output voltage. To regulate the output voltage, center-tapped transformer phase controlled rectifier is developed, as shown in Fig. 1.8(b)

[71]. Two low-frequency switches, typically thyristors, are used to chop the full-wave voltage with a controlled phase. However, when the switch is turned off, the input current is discontinuous and the energy cannot be extracted from the source during that interval. Further study on an active transformer-based ac-dc converter includes a bidirectional switch with synchronous switching at the secondary side (see Fig. 1.8(c)) [72]. By turning on or off two MOSFETs, the topology behaves as a boost ac-dc converter. However, the converter requires an external inductor and a transformer that increase the size of converter. In these transformer-based topologies, the transformer's operating frequency equals to the generator's low vibration frequency. Therefore, a bulky low-frequency transformer is required that increases the overall size and weight of converter. Moreover, the undesirable transformer leakage inductance causes the voltage to change with loading. In addition, a small dc bias from the input generator's voltage can lead to saturation of the magnetic core of transformer with the generation of harmonics.

### **1.3.3 PZ-specified Converters**

The voltage rectifiers and single-stage switching converters referred previously shows suitable for power conditioning of EMA and PZ generators. However, in the case of PZ generators, their high output impedances make it difficult for these converters to acquire optimal loads and extract maximum power. In order to match the output impedance of a PZ generator dominated by capacitive reactance, a significantly large inductance (tens of Henrys) may be required to create an optimal load. Hence, instead of using large inductance for impedance matching, the resistive impedance matching and resonant impedance matching are considered in the case where the excitation frequency couples with the intrinsic resonance of the generator.

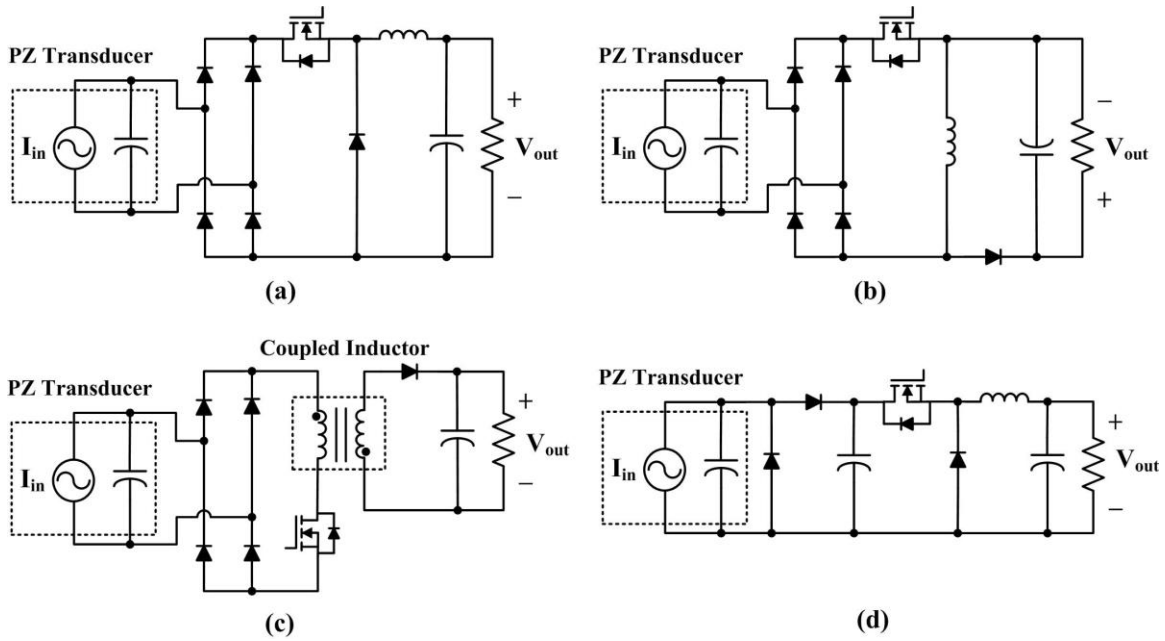


Figure 1.9. Resistive impedance matching converters: (a) diode full bridge followed by buck converter [73], (b) diode full bridge followed by buck-boost converter [74], (c) diode full bridge followed by flyback converter [75], and (d) voltage multiplier followed by buck converter [76].

First, the dual-stage topologies with resistive impedance matching are discussed to extract maximum power from PZ generators. These topologies are composed of a front diode bridge followed by a rear dc-dc switching converter. The rear dc-dc switching converters, such as buck, buck-boost and flyback converters (see Fig. 1.9(a)~(c)), perform as adjustable resistors when operating in discontinuous current mode (DCM) [73]-[75]. The diode full bridge can also be replaced with a voltage multiplier to boost the voltage, as shown in Fig. 1.9(d) [76]. Nevertheless, the front diode bridge and dual-stage configuration significantly reduce the efficiency. Furthermore, the unidirection of front diode bridge impedes the recharge of internal capacitance that limits the harvesting power.

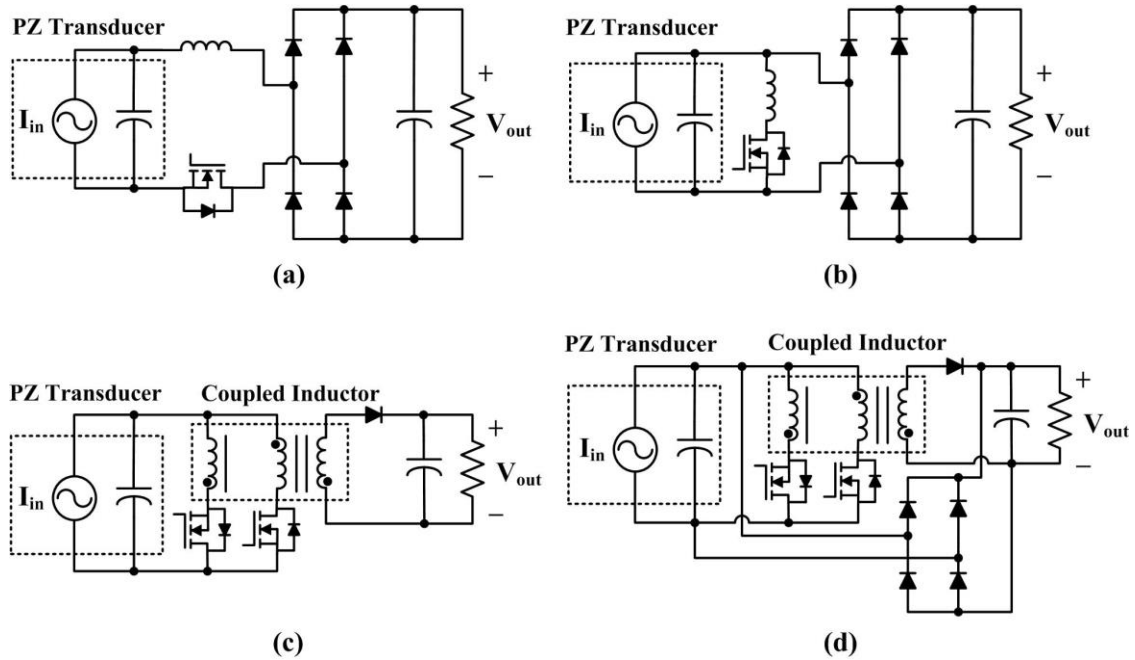


Figure 1.10. SSHI converters: (a) series-SSHI converter [77], (b) parallel-SSHI converter [78], (c) SSHI-MR converter [79], and (d) hybrid-SSHI converter [80].

In order to increase the efficiency and the possible harvesting power, synchronized switch harvesting on inductor (SSHI) converters with resonant impedance matching are investigated, such as series-SSHI and parallel-SSHI converters (see Fig. 1.10(a) and (b)) [77], [78]. The resonant rectifier, consisting of a front SSHI converter followed by a diode bridge, serves synchronized switch damping. Resonance at switching frequency occurs between the internal capacitor and the inductor of SSHI converter where only small inductance is necessary. The internal shunt capacitor is charged and discharged through resonance that results in a maximum generated voltage higher than open-circuit voltage. Therefore, it allows majority of the generated charge to be extracted from the PZ generators. In addition, the switching losses are reduced through the resonant switching. However, they still suffer from the diode forward voltage in the case of very-

low-amplitude voltage of PZ generators. The voltage stress of the switch also increases due to the resonance. Moreover, large inductance may be required when the internal shunt capacitance is small.

The transformer-based magnetic rectifier (MR) is utilized in SSHI-MR converters, as depicted in Fig. 1.10(c), to overcome the forward voltage issues [79]. The voltage is stepped up through the transformer before the diode bridge. The work is further improved through the hybrid-SSHI structure that increases the power gain (see Fig. 1.9(d)) [80]. However, the low-frequency transformer is required that increases the size and weight of converters; meanwhile, the transformer's coupling loss decreases the efficiency.

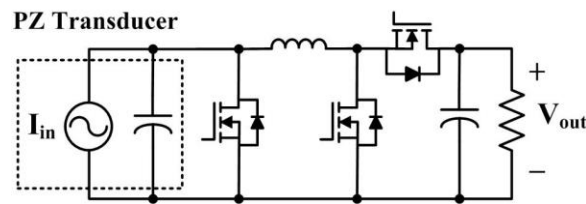


Figure 1.11. Rectifier free switched inductor converter [81].

Another approach to eliminate the diode bridge while maintaining resonant impedance matching is to use rectifier free switched inductor converter, as illustrated in Fig. 1.11 [81]. The MOSFETs are turned on or off depending on the condition of PZ generator. Although the converter avoids the diode bridge and low-frequency transformer, it adopts additional MOSFETs that increase the gating losses and the control complexity.

### 1.3.4 ES-specified Converters

Different from EMA and PZ generators, ES generators usually generate unipolar time-varying potentials that need dc-dc converters for voltage conditioning.

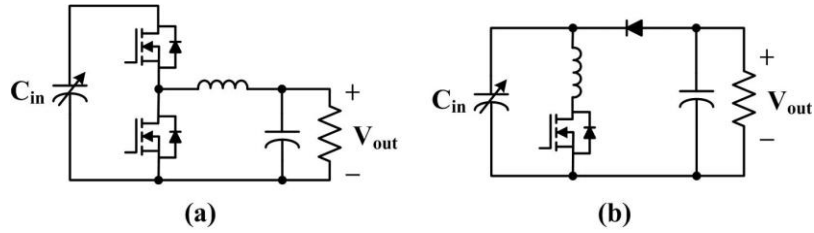


Figure 1.12. Charge constrained converters: (a) half-bridge buck converter [82] and (b) modified flyback converter [83].

Charge constrained ES generator is one type of ES generators of which the generated voltage may reach hundreds of volts with small amount of charge. Therefore, dc-dc step-down converter is required to buck the generator's high voltage to the battery cell voltage at a lower level. The most commonly used topology is a half-bridge buck converter, shown in Fig. 1.12(a) [82]. However, a reverse biased current through the parasitic diode of the low side MOSFET may cause additional loss. Furthermore, the high-side gate drive increases the design complexity. A modified version of the flyback converter, demonstrated in Fig. 1.12(b), is developed to prevent the reverse biased current and high-side gate drive [83]. Nevertheless, the parasitic capacitor of the diode reduces the efficiency.

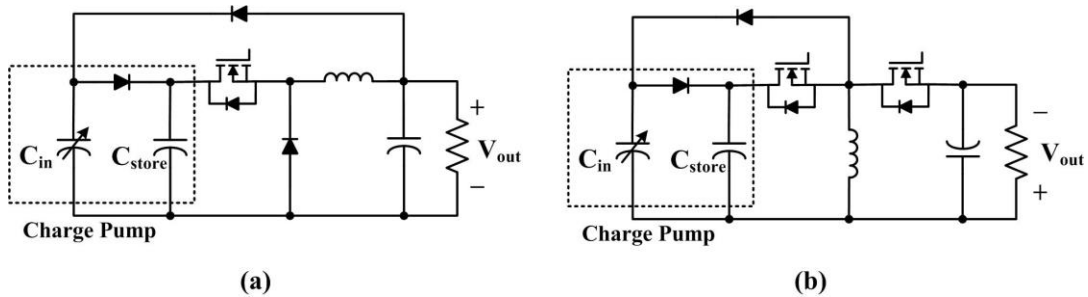


Figure 1.13. Voltage constrained converters: (a) charge pump buck flyback converter [84] and (b) charge pump buck-boost flyback converter [85].

Another type of ES generators is the voltage constrained ES generator of which the generated voltage is close to or lower than the battery cell voltage. Such generators usually need an asynchronous diode-based charge pump to first deliver the time-varying harvested power to a temporary storage capacitor  $C_{store}$ . Then, the energy stored in  $C_{store}$  is delivered to the load through a buck converter, shown in Fig. 1.13(a) [84]. A feedback diode is used to pre-charge the ES generator and constrain the generator voltage at the beginning of each harvesting cycle. Fig. 1.13(b) presents a similar topology with bidirectional buck-boost converter instead of unidirectional buck converter [85]. Thereby, the ES generator pre-charging is controllable and efficient. However, these converters suffer from the dominated losses in terms of inductor losses and switching losses.

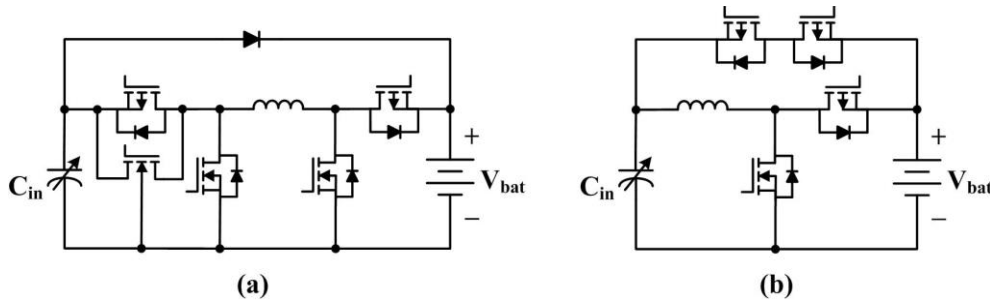


Figure 1.14. Battery constrained converters: (a) switched inductor buck-boost converter [86] and (b) switched inductor boost converter [87].

Battery constrained ES generators, where the generator's voltage is much lower than the battery cell voltage, also require generator pre-charging before the energy harvesting process begins. Due to the low-amplitude potential of generator, only one diode is used to deliver the harvesting energy to the load or battery. On the other hand, a buck-boost converter is used for controllable and efficient pre-charging of generator (see Fig. 1.14(a) [86]). The efficiency is improved by replacing the diode with a bidirectional

switch during energy harvesting process, shown in Fig. 1.14(b) [87]. Besides, the buck-boost converter is replaced by a boost converter for design simplicity. However, a large number of switches including bidirectional switches are required that increase the switching losses, gating losses and the complexity of gate drive.

### 1.3.5 Soft-switching Converters

Dual-stage ac-dc converters, single-stage ac-dc switching converters, ES-specified converters and majority of PZ-specified converters suffer from inefficient hard switching, which is even worse in the case of higher switching frequencies. The switching losses can be reduced through lower switching frequency; however, it accompanies bulky passive components, which in turn makes these topologies impractical for miniaturization [88]. Some of PZ-specified converters may have low switching losses due to resonant switching; however, they may require large inductance when the input sources have small shunt capacitance. Therefore, a soft-switching converter with small passive components is required.

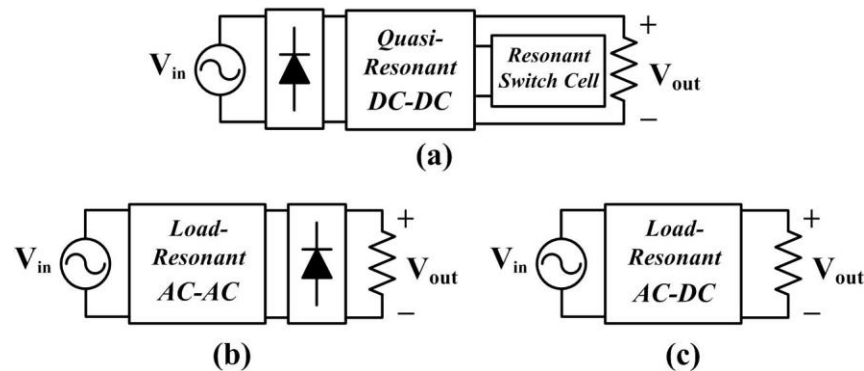


Figure 1.15. Soft-switching converters: (a) diode bridge cascaded with quasi-resonant dc-dc converter; (b) load-resonant ac-ac converter cascaded with diode bridge; (c) bridgeless resonant ac-dc converter.

Majority of investigations on soft-switching circuits have focused on modification of hard-switching converters by incorporating resonant switch cells (see Fig. 1.15(a)). These resonant-switch converters, referred as quasi-resonant converters, utilize auxiliary LC resonant circuit to primarily shape the current and voltage of main transistors during the turn-on and turn-off of the switching components [89]. Some of them connect passive resonant elements in series or in parallel with main transistors, such as quasi-resonant buck converters [90]-[92], while others adopt auxiliary transistors and diodes as active switch cells, such as ZVS-ZCS-PWM converters [93], [94]. However, additional switching losses or conduction losses in switch cell would degrade the efficiency. Switching losses of main transistors and diodes are reduced but not eliminated. The overall size of topology also increases by adding resonant switch cells while maintaining the main passive components. Moreover, the inefficient front diode bridge is still required.

Another approach of soft-switching adopts passive resonant networks as low impedance branches across transistors (see Fig. 1.15(b)), such as class D converters and class E converters, with purpose of energy transmission around resonant frequency [95]-[99]. Switching losses are reduced through the oscillating load voltage and current. The main passive components are not necessary in the operation. Load-resonant converters are simple and efficient at high-frequency or very-high-frequency operation. They have been discussed in SSHI converters, shown in Fig. 1.10. However, a post-positioned bridge rectification stage such as dual-stage resonant boost converter is required for ac-dc voltage conversion [97]. Unlike the quasi-resonant converters, the load has an influence on the voltage conversion of these load-resonant topologies. In addition, most of quasi-resonant and load-resonant converters suffer from high peak voltage and current

associated with the transistor and the resonant LC elements [100]. Therefore, a direct bridgeless resonant ac-dc converter, shown in Fig. 1.15(c), is a potential topological solution toward circuit miniaturization [101], [102].

## **1.4 State of the Art of PEI Topologies for Driving High-voltage Actuators**

### **1.4.1 Single-stage Drive Converters**

Conventional bulky power supplies and electronics used to drive electroactive polymer (EAP) actuators are not practical as on-board energy sources for microrobots. Miniaturized and efficient power electronic interfaces (PEI) are of critical importance to enable autonomous operation of microrobots [103]. One of the challenges of PEI design for such applications stems from the fact that most of the EAP actuators need to be excited with high voltage levels for efficient operation. However, the output voltage of suitable on-board energy sources including chemical battery cells, super-capacitors, fuel cells, and solar cells is generally less than 5V [104], [105]. In fact, the typical driving voltage of the EAP actuators is at least an order of magnitude higher than 5V [8]-[10], [106], [107]. Therefore, a tiny PEI with high-step-up voltage gain is required to be interfaced between the low-voltage energy source and the high-voltage actuators to not only step up the voltage but also satisfy the drive requirements of the actuator. Miniature power electronic converters suffer from low efficiencies particularly in light-loads [108]. In addition, due to the capacitive nature of the EAP actuators, majority of the transferred energy for excitation is unused and would be lost, if not retrieved [109]. Therefore, a bidirectional PEI could substantially enhance the actuator efficiency through recovering the unused energy during each cycle.

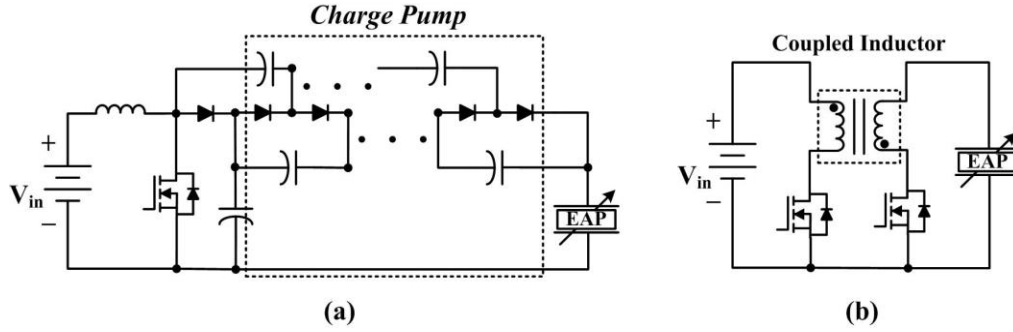


Figure 1.16. Single-stage converters: (a) a boost converter cascaded with a charge pump circuit [108], and (b) a bidirectional flyback converter [110].

Among prior research work on PEI topologies for driving high-voltage capacitive loads, researchers have studied utilizing a boost converter in series with a cascaded charge pump circuit (see Fig. 1.16(a)) [108]. The large number of capacitor-diode stages makes it impractical for miniaturization and efficient energy conversion. Furthermore, the converter is unable to recover the unused energy stored in capacitive actuators during each driving cycle, which consequently reduces the actuation efficiency. Researchers at the Harvard Microrobotic Laboratory at Harvard University implemented an energy recovery method using a bidirectional flyback converter for driving a single piezoelectric actuator (see Fig. 1.16(b)) [110]. However, the hard switching losses increase at higher switching frequency. At lower switching frequency, a relatively large inductance is required for transient energy storage that increases the coupled inductor size. Moreover, low coupling coefficient of inductor will increase leakage inductance that causes voltage spikes. On the other hand, high coupling coefficient of inductor may increase the fabrication difficulty.

### 1.4.2 Dual-stage Drive Converters

A unidirectional boost converter cascaded with a half-bridge inverter drive stage is adopted for driving bimorph piezoelectric (PZ) actuators [111] and electrostatic inchworm motors [112]. The boost converter is achieved by either cascading boost converters or using a coupled inductor (see Fig. 1.17(a) and Fig. 1.17(b)). Due to the circuit characteristics of half-bridge inverters, such topologies can only provide complementary signals and have to drive two actuators at same time. Moreover, the efficiency of the dual-stage converters is attenuated due to the hard switching, low coupling efficiency and cascaded topology. A boost converter using PZ transformer is also investigated as the first stage, illustrated in Fig. 1.17(c) [108]. Due to the limitation on fabrication techniques, a PZ transformer is typically larger than a discrete inductor or a coupled inductor at the same power level. Additionally, the converter has to operate at the optimal frequency of PZ transformer that otherwise cannot generate high voltage step-up ratio.

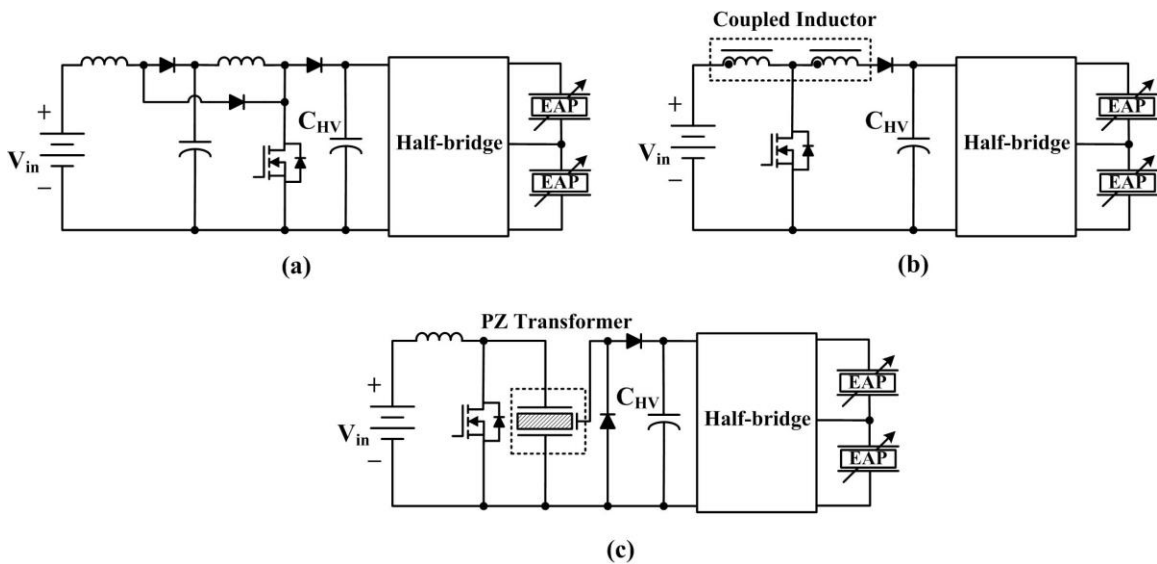


Figure 1.17. Dual-stage converters: (a) a cascaded boost converter followed by a half-bridge inverter, (b) a coupled-inductor boost converter followed by a half-bridge inverter [111], (c) a PZ transformer-based boost converter followed by a half-bridge inverter [108].

### 1.4.3 Resonant Drive Converters

Among the prior works, there are two approaches to drive multiple EAP actuators: (1) paralleling multiple single-stage converters (see Fig. 1.18(a)) [110]; and (2) using dual-stage converter with half-bridge inverters (see Fig. 1.18(b)) [111]-[113]. One common issue of these drive converters stems the tradeoff between the miniaturization and the inefficient energy conversion due to their hard-switching operation. Miniaturization and system integration of the PEIs are heavily dependent on the required number and size of inductive and capacitive passive components. The sizes of passive components depend on the amount of transient energy storage [88]. There is a motivation to increase the converter switching frequency, since the required transient energy storage decreases at a higher frequency. However, frequency-dependent device loss mechanisms, including switching loss and gate driving loss, constrain the switching frequency.

Soft switching techniques such as ZVS and ZCS are demanded to mitigate the voltage-current overlap and capacitive discharge losses [89], [90]. High-frequency resonant converters allow small size of energy storage without suffering from switching losses. Therefore, resonant converters with soft-switching capabilities are excellent alternatives, for high-frequency operation without sacrificing efficiency and size of the PEIs. Fig. 1.18(c) presents the paralleling resonant converters that have advantages upon other topologies in terms of: (1) single-stage topology; (2) resonant lossless switching; (3)

small value of passive components; (4) independent actuator drive; (5) simple gate drive; and (6) small battery current ripple.

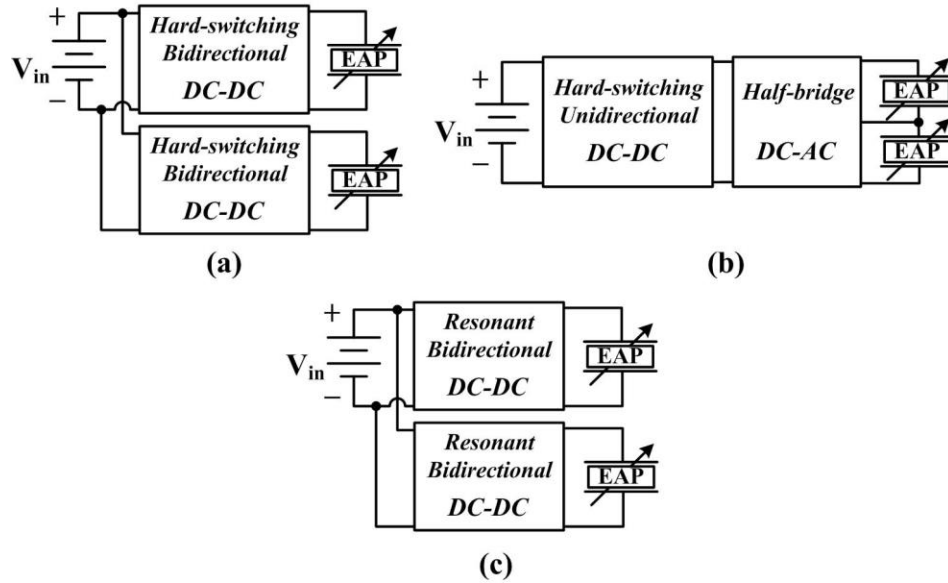


Figure 1.18. Topologies for driving multiple EAP actuators: (a) paralleling bidirectional dc-dc switching converters, (b) a unidirectional dc-dc converter cascaded with half-bridge inverters, (c) paralleling bidirectional resonant converters.

## 1.5 Fabrication Techniques toward PEI Miniaturization

Other than topology design, various fabrication processes toward PEI miniaturization are investigated to reduce the size and weight of semiconductors, inductive and capacitive components.

### 1.5.1 CMOS Technology

Complementary metal-oxide-semiconductor (CMOS) technology has been widely used in digital logic circuits and analog circuits to construct integrated circuit [55]-[59], [114]-[122]. CMOS integrated circuits have the distinctive features in terms of high noise immunity, low static power consumption and high density of logic function on a chip

[123]. Therefore, CMOS fabrication process is the most used technology to implement chip integration, where large amount of logic function and low power consumption of circuits is required in a tiny space. Fig. 1.19(a) illustrates a static CMOS inverter consisting of a complementary PMOS and NMOS pair.

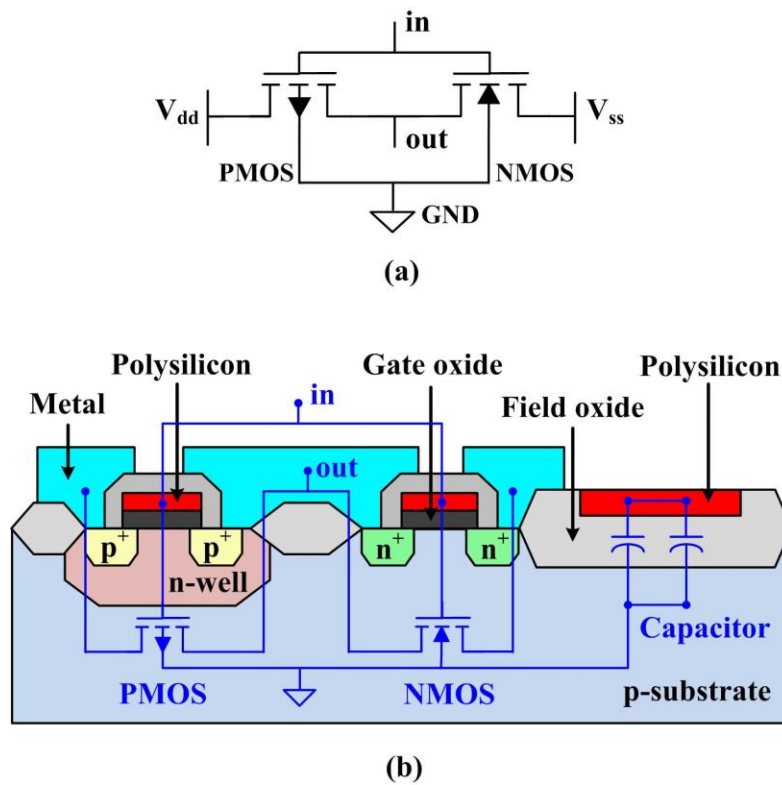


Figure 1.19. CMOS integrated circuit: (a) CMOS inverter, (b) cross-sectional schematic of two transistors and capacitors die chip, in an n-well CMOS process [123].

A CMOS integrated circuit is manufactured through CMOS fabrication process that stacking layers of various materials in a pre-specified sequence. Majority of layers, including substrate, field oxide, gate oxide, polysilicon and metal layers, are created and then patterned through lithographic process except for the doping layers. There are four dominant CMOS processes: n-well process, p-well process, twin-tub process and silicon on insulator (SOI), each of which has different features. For instance, in n-well process,

an NMOS device is fabricated on a p-type substrate while a PMOS device is fabricated on the same substrate with an n-type well, depicted in Fig. 1.19(b) [123]. In addition, the capacitor can be fabricated by adding a polysilicon layer on top of the filed oxide. Hence, CMOS transistor pairs and capacitors can be fabricated on one substrate that saves the chip area and acquires high density of chip components.

CMOS manufacturing process can also be classified based on the maximum length or width of transistors. The most commonly used process can create transistors with 0.1~0.5 $\mu\text{m}$  length or width. Ultra small CMOS transistors with length as small as 5nm can be fabricated. Table 1.4 and Table 1.5 list the previous works using different CMOS technologies for ac-dc and dc-dc conversion, respectively.

TABLE 1.4  
PARAMETERS OF AC-DC CONVERSION USING CMOS TECHNOLOGY

Reference	Output Power ( $\mu\text{W}$ )	Die Chip Area ( $\text{mm}^2$ )	Input Voltage ( $V_{\text{rms}}$ )	Output Voltage (V)	Peak Efficiency	Fabrication Process
[55]	22	0.04	0.85	1	86%	0.25 $\mu\text{m}$ CMOS Non-inductor
[56]	600	0.52	0.9	1	/	0.13 $\mu\text{m}$ CMOS Non-inductor
[57]	460	1.72	0.88	0.96	76%	0.18 $\mu\text{m}$ CMOS Non-inductor
[58]	$40 \times 10^3$	1.03	0.8~1.7	1~2	95%	0.35 $\mu\text{m}$ CMOS Non-inductor
[59]	$19 \times 10^3$	2.25	3.5	4.36	84.8%	0.5 $\mu\text{m}$ CMOS Non-inductor

[115]	45	4.25	1.7	3.2	/	0.35 $\mu\text{m}$ CMOS External inductor
[116]	25	4.53	0.85	2	70%	0.5 $\mu\text{m}$ CMOS External inductor

TABLE 1.5  
PARAMETERS OF DC-DC CONVERSION USING CMOS TECHNOLOGY

Reference	Output Power ( $\mu\text{W}$ )	Chip Area ( $\text{mm}^2$ )	Input Voltage (V)	Output Voltage (V)	Peak Efficiency	Fabrication
[86]	1.6	4.84	3	3.4	/	1.5 $\mu\text{m}$ CMOS External inductor
[117]	$500 \times 10^3$	5.48	1.8	3.3	87%	0.6 $\mu\text{m}$ CMOS Non-inductor
[118]	$400 \times 10^3$	4.16	4	1.5	87%	0.25 $\mu\text{m}$ CMOS External inductor
[119]	$11.2 \times 10^3$	0.72	1.2	7	37%	0.13 $\mu\text{m}$ CMOS Micro-inductor
[120]	$1 \times 10^3$	2.56	0.3	1.1	70%	0.18 $\mu\text{m}$ CMOS Non-inductor
[121]	400	1.2	0.2	1.2	36%	0.18 $\mu\text{m}$ CMOS External inductor
[122]	175	0.4	0.1	1	75%	0.13 $\mu\text{m}$ CMOS External inductor

Due to the extreme small area and low power consumption of die chips, the circuits using CMOS fabrication process can acquire high power density and medium efficiency. However, majority of these chips can only handle very-low power (usually less than 100mW) due to CMOS fabrication architecture. Furthermore, the power supply

of a CMOS chip (typically less than 5V) constrains its capability of handling voltage higher than that of power supply. Besides, there is a limitation on fabricating low-loss inductive components on chip.

In the case of electromechanical systems, the power stage of a PEI may need to handle power and voltage much higher than logic level. Since the power stage is logically simple, there is no need to require high density of logic function. On the other hand, the power and voltage of gate drives and controllers are close to logic level; meanwhile, they demand high density of logic function. Therefore, CMOS technology is well suitable for miniaturization of gate drives and controllers rather than the power stage.

### **1.5.2 Bare Die and Chip-scale Package**

In addition to CMOS integrated circuits, using miniature surface-mounted (SMT) discrete components on an optimal-designed printed circuit board (PCB) is another approach toward fabricating miniaturized PEI, especially the power converters [67], [124]. A die of a single semiconductor is the smallest unit in the circuit packaging. Typically, it is massively produced by cutting the processed wafer into many pieces. Despite of its small size, a component in bare die is not commonly used on PCB due to the mechanical instability and failure. An external package is needed to provide protection from interference and increase mechanical robustness.

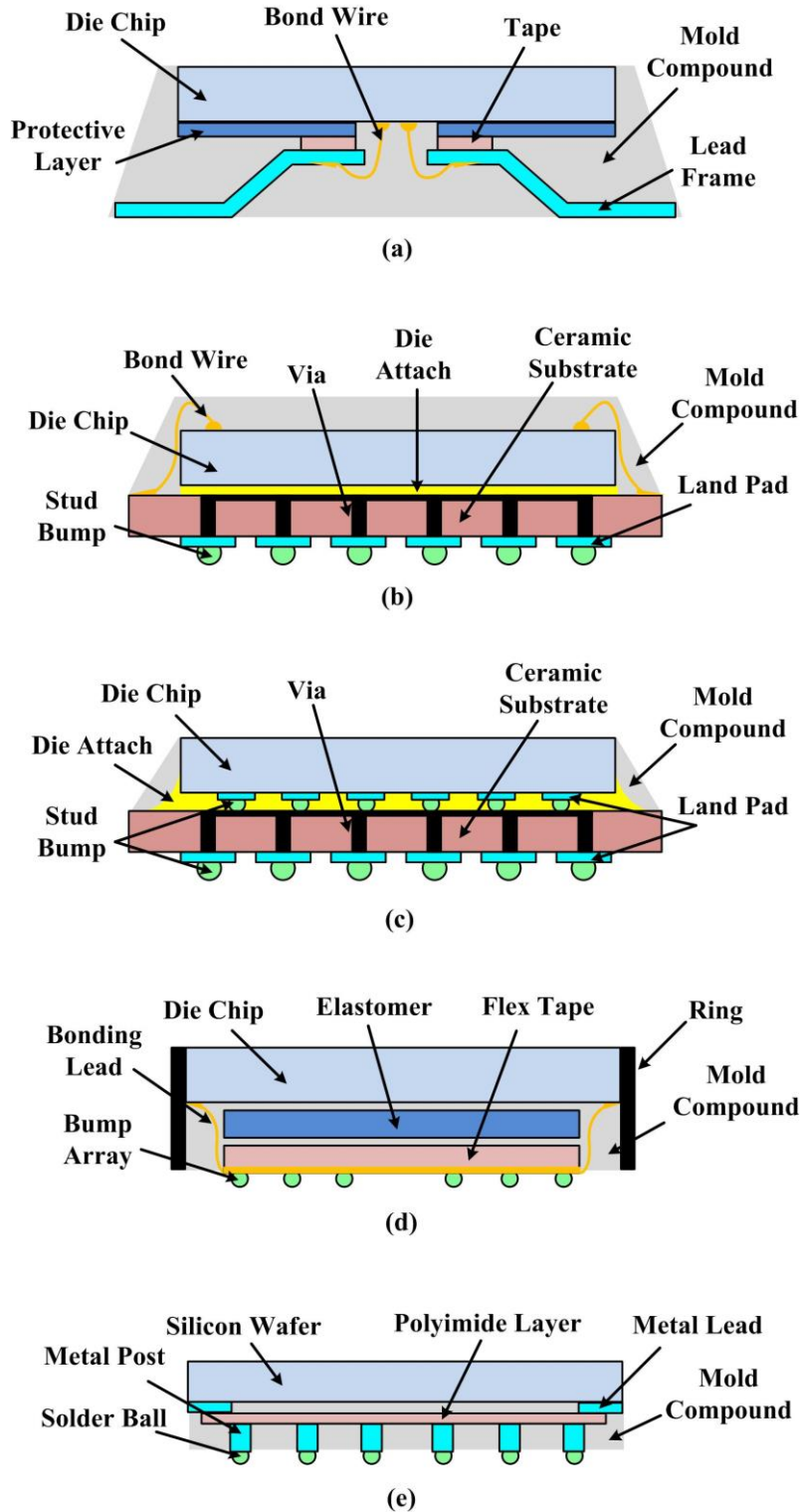


Figure 1.20. Cross-sectional view of CSP: (a) lead frame based CSP, (b) rigid substrate based CSP with wire bonding, (c) rigid substrate based CSP with flip-chip, (d) flexible substrate based CSP, and (e) wafer-level CSP [125].

In order to minimize the size of package, chip-scale package (CSP), which is direct surface mountable and has an area no greater than 1.2 times that of a single die, is an excellent choice [125]. The CSP has advantages in terms of high density I/O counts, small propagation delay and low cost. Four different CSP styles emerge as market leaders: lead frame based CSP (LFCSP), rigid substrate based CSP, flexible substrate based CSP, and wafer-level CSP (WLCSP).

LFCSP is fabricated based on modified lead frame that are created during the package assembly process, shown in Fig. 1.20(a). Wire bonding is used for chip interconnection. However, the lead frame usually wastes area that in turn reduces the I/O counts density. Its electrical performance is low due to the large capacitance and inductance of large interconnection size. Therefore, rigid substrate based CSP, illustrated in Fig. 1.20(b), is investigated that uses a ceramic substrate with solder bumps instead of lead frame. Such package has high I/O counts, high electrical performance and high thermal performance, owing to the solder bumps underneath the package. The package is further improved by replacing the wire bonding with solder bumps for chip interconnection (see Fig. 1.20(c)).

Flexible substrate based CSP that is based on flexible laminated interposer is usually used in flexible PCB, depicted in Fig. 1.20(d). The features of flexible material bring the benefits of small thickness and fine-line imaging of circuit patterns. However, it can be very cost-effective. In the case of WLCSP (see Fig. 1.20(e)), the chip assembly takes place at wafer level rather than at individual chip level. The pads of a WLCSP are etched or printed directly onto a silicon wafer. Hence, the package size is very close to

the size of a silicon die. In comparison to other CSPs, WLCSP has high area-effectiveness and low cost-effectiveness.

Table 1.6 lists the PEIs in prior works using bare die or CSP components. In comparison to CMOS technologies, higher voltage and power are acquired in these PEIs while their size and efficiency are still promising. Moreover, mounting discrete components on a PCB makes these PEIs more flexible to be replaced than an integrated chip. However, the circuit fabrications in these works are not area-effective. In majority of these works, the inductive components are heavy and bulky. Despite this, CSP components show well suitable for miniaturization of PEI power stage.

TABLE 1.6  
PARAMETERS OF PEI USING BARE DIE OR CHIP-SCALE PACKAGE

Reference	Output Power (mW)	Chip Area (cm <sup>2</sup> )	Input Voltage (V <sub>rms</sub> )	Output Voltage (V)	Peak Efficiency	Fabrication
[62]	1	1.54	0.1~1	0.3~2.8	70%	CSP semiconductor Non-inductor
[67]	54.5	4	0.4	3.3	71%	CSP semiconductor SMT inductor
[73]	1.5	6	1.6	4.8	78%	Through-hole (TH) components
[108]	100	3.5	5	250	61%	CSP semiconductor SMT inductor
[110]	200	0.63	3.7	200	50%	Bare Die CSP semiconductor Micro-transformer
[124]	0.2	3	4	2	/	CSP semiconductor TH inductor

### **1.5.3 Micro-coil and Micro-core**

Among the electronic components of a power electronic converter, inductive components, such as inductors and transformers, usually occupy the majority of size and weight of a circuit due to its large amount of transient energy storage [100], [126]. Thereby, reducing the size and weight of inductive components is an effective approach for PEI miniaturization. In addition to size reduction of inductive components by using high-frequency resonant topology, the micro-fabrication method can further reduce the footprint of inductive components while maintaining high electrical performance [127].

In standard fabrication process, electromagnetic integration of magnetic cores is an efficient approach toward miniaturization and integration while enhancing electrical performance. However, in micro-fabrication, such method loses its ascendant due to the complexity of material processing and patterning [128]. Besides, material losses of integrated magnetic cores significantly reduce the electromagnetic performance in and above the MHz regime. As a result, optimized fabrication strategies that create ultra-compact coils with easy processing and patterning are developed for fabricating miniature inductive components. High quality and high coupling factors of inductive components at very high frequency (VHF) can be acquired through the optimized fabrication process [128].

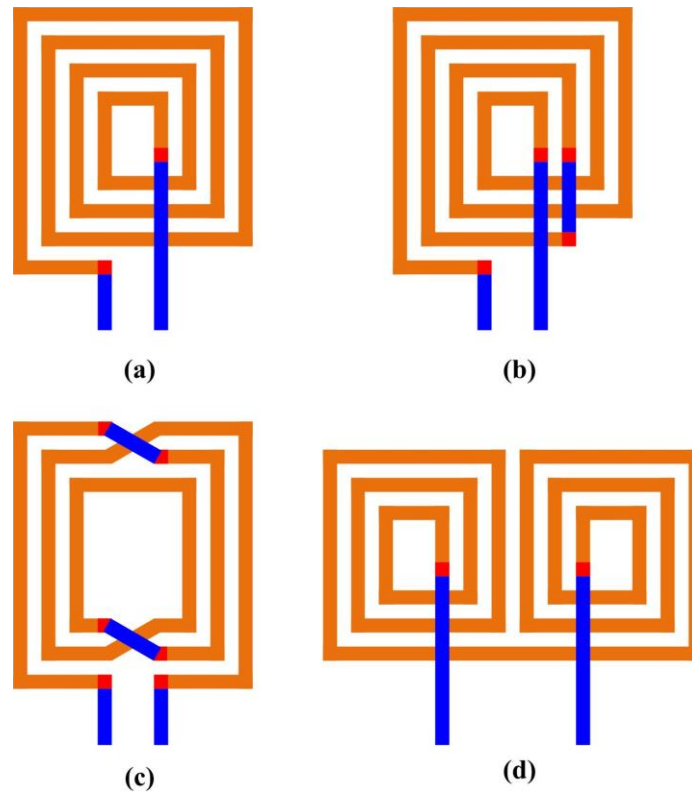


Figure 1.21. 2D spiral planar layouts: (a) conventional spiral, (b) conventional spiral with equal loop area, (c) interwound spiral, and (d) twin spiral [130].

2D planar layouts, including spiral planar coils [129], [130] and stacked planar coils [131], have been widely used to realize miniaturization by saving 3D space. Flat coils are fabricated by electroplating multiple metal layers with thicknesses of several microns inside an insulating substrate such as PCB. Fig. 1.21 presents commonly used 2D spiral planar layouts [130]. In order to save area and increase electrical performance, multilayer flat coils can be stacked in multilayer PCB to create a stacked planar coil, shown in Fig. 1.22 [131]. Electrical performance can be further enhanced by inserting magnetic cores in the center of flat coils. In addition, 2D planar process is compatible with MEMS fabrication. However, flat inductive components suffer from the relatively low quality factor and large footprint in area.

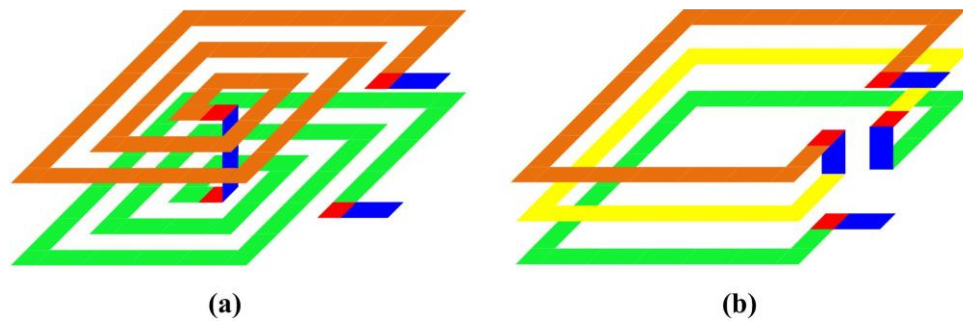


Figure 1.22. 2D stacked planar layouts: (a) stacked spiral coils with same direction, and (b) multilayer coils with different directions [131].

Another approach toward fabricating micro-coils is to produce 3D solenoids with different cross-sectional shapes, such as circle and polygon, and different micro-cores. In spite of time-consuming fabrication process, 3D micro inductive components show promising due to their high electrical performance and small footprint [132]. Prior research presents a success on fabricating a micro-coil with axis perpendicular to the PCB (see Fig. 1.23(a)) [133]. The work is continuously expanded into magnetic-core based micro-transformer where micro-coil is wound on a thermoplastic filled with ferrite nanoparticles, illustrated in Fig. 1.23(b) [134]. Fig. 1.23(c) demonstrates a closed-loop magnetic core that is utilized to enhance the electromagnetic performance. To reduce the component weight and fabrication complexity, a micro-coil fabricated on a SU-8 polymer core is reported with the same performance as air-core transformer, shown in Fig. 1.23(d) [134].

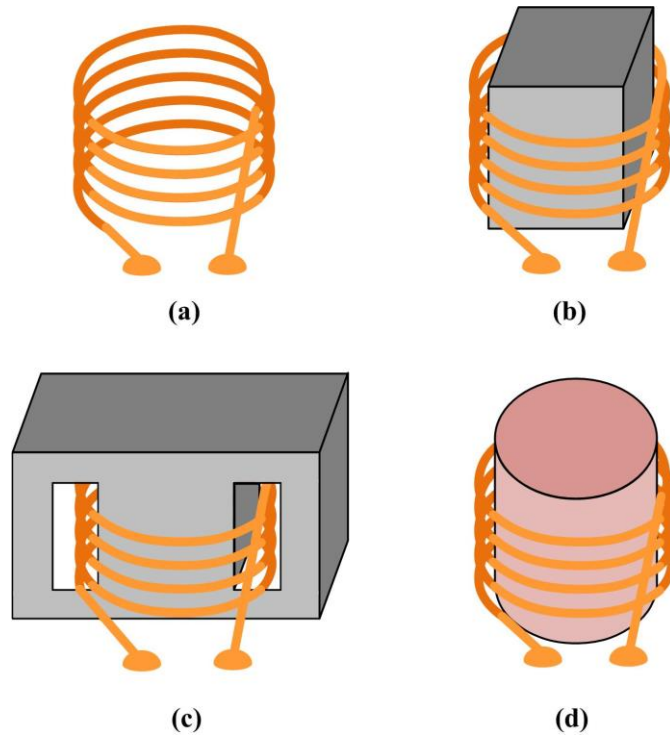


Figure 1.23. 3D solenoid layouts: (a) micro-coil with air [133], (b) micro-coil with open-loop magnetic core, (c) micro-coil with closed-loop magnetic core, and (d) micro-coil with non-magnetic core [134].

3D layouts have superiorities upon 2D planar counterparts in terms of higher inductance density and higher coupling effect. A micro inductive component fabricated through optimized 3D solenoid process can provide miniaturization without sacrificing electrical performance. Therefore, the 3D solenoid is an excellent potential approach toward fabricating inductive component for miniaturized PEI.

## 1.6 Thesis Objective and Contribution

In this dissertation, the technology toward miniaturization of PEI for tiny EM systems is investigated in order to provide the potential of ultra-compact system integration. High-frequency resonant switching technologies, including zero-voltage-

switching and zero-current-switching, and novel resonant converter topologies are outlined as potential solutions for PEI miniaturization. Designs and implementations of unique miniaturized PEI are presented for validation of ultra-compact system integration in both low-voltage energy harvesting and autonomous mobile microrobots.

Two types of bridgeless resonant ac-dc step-up converters are first introduced and developed to efficiently convert arbitrary input voltages of EM generators into a regulated dc output voltage suitable for energy storage units. The proposed topologies provide direct ac-dc power conversion with less number of components, in comparison to other resonant topologies. Meanwhile, they provide reasonably high efficiency from light-load to full-load condition. Moreover, resonant switching operation at MHz level allows the miniaturization and reasonable efficiency of converters through using substantially smaller capacitive and inductive passive components.

In the second part of the dissertation, the work is extended to developing multi-input power electronic converters as interfaces for multi-channel electromagnetic energy harvesting systems. The resonant topological concept is expanded through introducing a multi-input bridgeless resonant ac-dc converter capable of achieving ac-dc conversion; boosting input voltages; addressing mutual interference of multiple generators; and matching optimal impedance for a multiple-channel electromagnetic energy harvesting system. It also achieves optimal impedance matching through adjusting the resonance impedance. The multi-input converter can take advantage of the self-inductance of input electromagnetic sources, and only utilizes one external magnetic component and one diode.

The third part of the dissertation extends the concepts of miniaturization to the field of microrobotics. Conventional bulky power supplies and electronics are not practical as on-board energy sources to drive high-voltage actuators in microrobots. Miniaturized and efficient PEI is of critical importance to enable autonomous operation of microrobots. A bidirectional single-stage resonant dc-dc step-up converter is invented and developed to efficiently drive high-voltage actuators. The converter utilizes resonant capacitors and a coupled-inductor as a soft-switched LC network to acquire high step-up voltage gain. The circuit is capable of stepping up low voltage of energy storage units, generating explicit high-voltage actuation signals, and recovering unused energy remained in the capacitive actuators.

In this dissertation, innovative and miniaturized PEIs are introduced to address efficient power conditioning for low-voltage energy harvesting and high-voltage microrobotic actuating. The contributions mainly focus on size miniaturization of power converter with high efficiency, which can be summarized as:

1. Introduced and developed a PEI for low-voltage EM energy harvesting
  - Proposed a novel single-stage bridgeless resonant ac-dc converter with advantages in terms of (i) capability of efficient operation in the case of alternating low-amplitude input voltages; (ii) capability of high-frequency switching operation; (iii) small number and size of passive components; (iv) low voltage stresses on transistors; and (v) simple gate drive.
  - Provided theoretical operation principle, modeling and stress analyses of the proposed converter.

- Developed a 5mm×6mm, 2MHz prototype capable of converting an alternating, erratic, irregular, low-voltage ( $0.25 V_{ac} \sim 5 V_{ac}$ ), low-power (less than 650 mW) input into a regulated dc output with high efficiency (up to 83%).
- 2. Introduced and developed a PEI for multi-channel energy harvesting systems
  - Proposed a novel single-stage multi-input bridgeless resonant ac-dc converter with advantages in terms of (i) capability of interfacing and conditioning the output power of multiple EM generators; (ii) no need for inefficient diode bridge at each channel; (iii) small number and value of passive components; (iv) high step-up gain at 0.5 switching duty cycle; and (v) simple gate drive.
  - Provided fundamental operational principles of the multi-channel ac-dc converter, modeling and impedance analyses of the proposed interface.
  - Developed a prototype capable of addressing ac-dc conversion for a six-channel, low-voltage ( $0.5 V_{ac} \sim 5 V_{ac}$ ), low-power (less than 30 mW) wind energy harvesting panel with high efficiency (up to 86.3%).
- 3. Introduced and developed a PEI for driving high-voltage actuators in mobile microrobots
  - Proposed a novel single-stage bidirectional resonant dc-dc step-up converter with advantages in terms of (i) capability of efficient driving high-voltage actuators; (ii) capability of recovering unused energy of actuators; (iii) small number and size of passive components; (iv) very

high step-up gain with medium turn-ratio coupled inductors; and (v) simple gate drive.

- Proposed theoretical analyses and fundamental operation principle, modeling and driving strategy design of the innovative converter.
- Developed a 4mm×8mm, 1.5MHz prototype capable of driving high-voltage actuator-based electrostatic inchworm motor with high voltage-gain (up to 50), high driving frequency (1 kHz ~ 10 kHz) and high efficiency (up to 81%).

## **1.7 Dissertation Overview**

The contents of the dissertation are divided into several parts to discuss the PEI design for ultra-compact EM systems step by step. Chapter 1 discusses the intension, significance and challenges of the PEI design and miniaturization for ultra-compact EM systems. It provides the detailed overview of challenges in topology design and the state of art of topologies for both kinetic energy harvesting and autonomous mobile microrobots. Furthermore, a comprehensive review of current micro-fabrication technologies toward miniature PEIs is presented.

Chapter 2 is to design and develop a miniature PEI to efficiently addressing ac-dc conversion for energy harvesting generators that can be installed in wearable electronic devices. Novel bridgeless resonant ac-dc topologies are introduced to address power conditioning of low-voltage energy sources. The principle of operation, steady-state characteristics and electrical stresses are mathematically analyzed through a comprehensive circuit modeling. A resonant gate driver and a module on/off control strategy are designed to further increase the circuit efficiency through the efficient gating

and controlling. A miniature prototype of PEI, including resonant power stage, resonant driver and controller, is developed for validation of its capability of efficiently addressing low-voltage energy sources with good resonant switching performance and fast transient response.

Chapter 3 presents the design and implementation of a miniature multi-input PEI to address power conditioning for multi-channel energy harvesting systems. The modeling of an electromagnetic generator and a multi-channel energy harvesting system are investigated. A novel multi-input bridgeless resonant ac-dc topology is proposed to provide multi-channel ac-dc conversion for an electromagnetic energy harvesting system. Circuit switching sub-intervals, steady-state analyses and optimal impedance matching are discussed. The design specification for a six-input prototype and experimental results on a wind energy harvesting system are carried out.

Chapter 4 presents the design and implementation of a miniature PEI for driving high-voltage actuators in mobile microrobotic systems. A bidirectional single-stage resonant dc-dc step-up converter is proposed to step up the low voltage of energy storage unit and generate high-voltage pulsatile signals. The specific requirement and strategies to drive electrostatic inchworm motor are introduced. The analysis and control scheme of the adopted drive circuit are elaborated. Furthermore, the design guideline of the driving topology and the experimental validation of the prototype are presented, respectively, for validation of driving high-voltage electrostatic inchworm motor with energy recovery capability.

Chapter 5 represents the conclusions and contributions of miniature PEI design and implementation for energy harvesting and microrobotic systems. In addition, the future prospects of the miniaturized PEI are presented.

## **1.8 Summary**

This chapter provides comprehensive review of circuit topologies and fabrication processes for PEI miniaturization of tiny electromechanical systems. Distinctive features of PEI topologies for energy harvesting systems, including dual-stage ac-dc converters, single-stage ac-dc switching converters, PZ-specified converters as well as ES-specified converters, are presented. Majority of these topologies suffer from inefficient diode bridges, switching losses, bulky passive components, inefficient coupling inductor and complicated gate drive, which can be improved by introducing an innovative single-stage bridgeless ac-dc resonant converter. Furthermore, prior works on driving high-voltage actuators of microrobot, including single-stage switching converters and dual-stage switching converters, are analytically discussed. There are a large number of challenges, including large switching losses, bulky passive components, inefficient coupling inductor, actuator drive limitation and energy recovery of actuator, which can be improved by introducing an innovative bidirectional single-stage dc-dc resonant converter. In addition to the topology design, the fabrication processes are surveyed and discussed, including CMOS integrated circuit, miniaturized packages of discrete components and optimized micro-coil fabrication. According to the distinctive advantages of each process, the components of power stage of a PEI are preferred to use chip-scale package and 3D micro-coil, while CMOS technology is preferable to fabricate the gate drive and controller.

## CHAPTER 2

### MINIATURIZATION OF POWER ELECTRONIC INTERFACES FOR TINY ELECTROMECHANICAL SYSTEMS

According to the summary of Chapter 1, a promising topological solution toward PEI miniaturization can be a bridgeless high-frequency resonant ac-dc converter, which has superiorities upon others in terms of: (1) single-stage topology; (2) no need for inefficient diode bridge; (3) resonant lossless switching; (4) small value of passive components; (5) relatively low stress on transistors; (6) simple gate drive; and (7) both ac-dc and dc-dc conversion. This chapter presents novel design of resonant topologies toward fabricating miniaturized PEI for tiny electromechanical systems.

#### 2.1 Design of Bridgeless Resonant AC-DC Converters

##### 2.1.1 Circuit Description

Fig. 2.1 illustrates two types of single-stage bridgeless resonant ac-dc step-up converters. These two topologies share the same principle of operation. Both circuits are capable of operating with multi-resonant switching. Each topology is formed by two resonant inductors, two resonant capacitors, two power transistors and one diode. The input source is a low-frequency alternating voltage with high-order harmonic distortions [3], [15]. The input inductor  $L_{r1}$  is sharply tuned with one resonant capacitor, contributing to half of the resonant oscillation. The resonant inductor  $L_{r2}$  is tuned with two split resonant capacitors  $C_{r1}$  and  $C_{r2}$  to resonate near the fundamental component of switching frequency  $f_s$ . Ideally, the components  $L_{r2}$ ,  $C_{r1}$  and  $C_{r2}$  present a lossless low drain-to-source impedance branch across transistors near  $f_s$ .  $C_{r1}$  and  $C_{r2}$  are in parallel with the transistors and the diode to ensure ZVS at turning-on and turning-off. Switching losses

are eliminated through the oscillating voltage and current, while the input energy is stored and released to the load through the active LC network. Furthermore, the tuned networks eliminate overvoltage spikes as well as diode reverse recovery issues while simultaneously maintaining low peak voltage stresses on the power transistors.

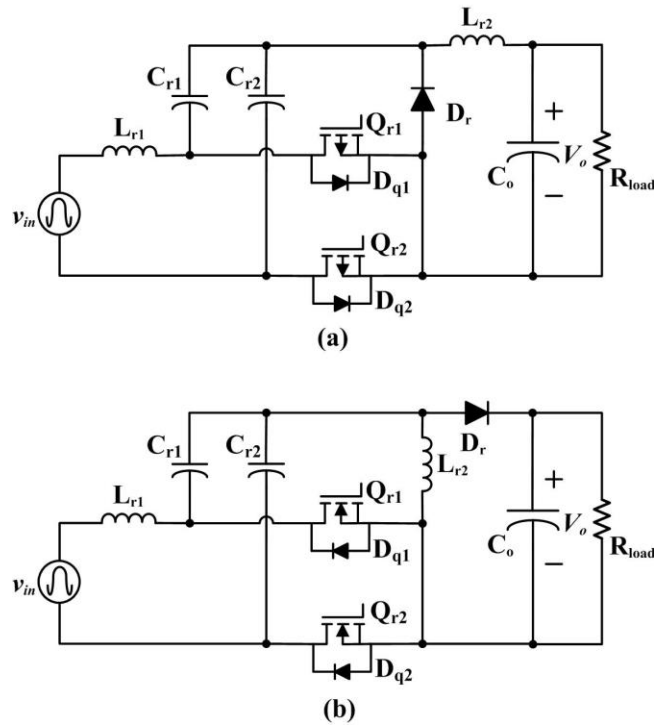


Figure 2.1. Proposed bridgeless resonant ac-dc step-up converters: (a) Type 1; (b) Type 2.

Power transistors  $Q_{r1}$  and  $Q_{r2}$  are actively turned on and off in order to generate drain-to-source pulse voltage at the input of LC network. The amplitude of drain-to-source pulse voltage is higher than  $v_{in}$  due to the energy stored in  $L_{r1}$ . The fundamental component of drain-to-source pulse voltage passes through the LC network and generates an amplified oscillating voltage near the switching frequency  $f_s$  across the rectifier diode  $D_r$ . ZVS and ZCS operation of  $Q_{r1}$  and  $Q_{r2}$  provide energy recovery to drain-to-source parasitic capacitor  $C_{ds}$  of power transistors, which in turn increases the efficiency. The

overvoltage spikes on drain-to-source voltage is eliminated, thereby no snubber circuit is required. The diode  $D_r$  rectifies the amplified oscillating voltage after the tuned network into a dc output voltage. It generates freewheeling path for the resonant inductor current as well as charging path for the resonant capacitors. The rectifier diode  $D_r$  can be replaced with a transistor if bidirectional configuration is required. The body diodes  $D_{q1}$  and  $D_{q2}$  serve as freewheeling diodes for ZVS and ZCS, when the switching frequency is higher than the resonant frequency.

According to the directions of body diodes and source nodes of transistors, p-channel MOSFETs are preferred for Type 1 converter while n-channel MOSFETs are preferable for Type 2 converter, for the ease of gate driver design. Due to the different doping processes of p-type and n-type, n-channel MOSFETs usually have faster transient response than p-channel MOSFETs. In addition, p-channel MOSFETs require negative gate drive voltage, which increases the complexity of gate driver design. Therefore, Type 2 converter has advantages over Type 1 in terms of higher switching frequency capability and easier gate driver design.

To address the challenges referred in Chapter 1, the proposed topologies bring several advantages: (1) capability of efficient operation in the case of alternating low-amplitude input voltages; (2) capability of high-frequency switching operation; (3) small number and size of passive components; (4) theoretically no switching losses; (5) low loss caused by diode forward voltage; (6) no need for additional snubber circuits; (7) no diode reverse recovery issues; and (8) low voltage stresses on transistors.

### 2.1.2 Principle of Switching Operation

The switching sub-intervals of Type 1 as well as Type 2 converters during one switching cycle with a positive input voltage are shown in Fig. 2.2 (I)~(V) and Fig. 2.3 (I)~(V), respectively. The simulation waveforms of transient voltage and current, with different switching frequencies of Type 1 as well as Type 2 converters, are demonstrated in Fig. 2.4 and Fig. 2.5, respectively.

There are two resonant frequencies in these circuits,  $f_r'$  is the resonant frequency of  $L_{r2}C_{r1}C_{r2}$  network and  $f_r$  ( $f_{r1}=f_{r2}=f_r$ ) is the resonant frequency of  $L_{r1}C_{r2}$  and  $L_{r2}C_{r1}$  networks. Depending on the switching frequency ( $f_s$ ), there are three different operating regions: (a)  $f_s < f_r'$ , (b)  $f_r' < f_s < f_r$ , and (c)  $f_s > f_r$ . In the case of  $f_s < f_r'$  and  $f_s > f_r$ , there are four switching sub-intervals in one switching cycle, while the case of  $f_r' < f_s < f_r$  is composed of five switching sub-intervals (*Stage I ~ Stage V*). Each switching sub-interval of Type 1 converter for  $f_r' < f_s < f_r$  is described briefly below, as it contains all the other sub-intervals in the case of  $f_s < f_r'$  and  $f_s > f_r$ .

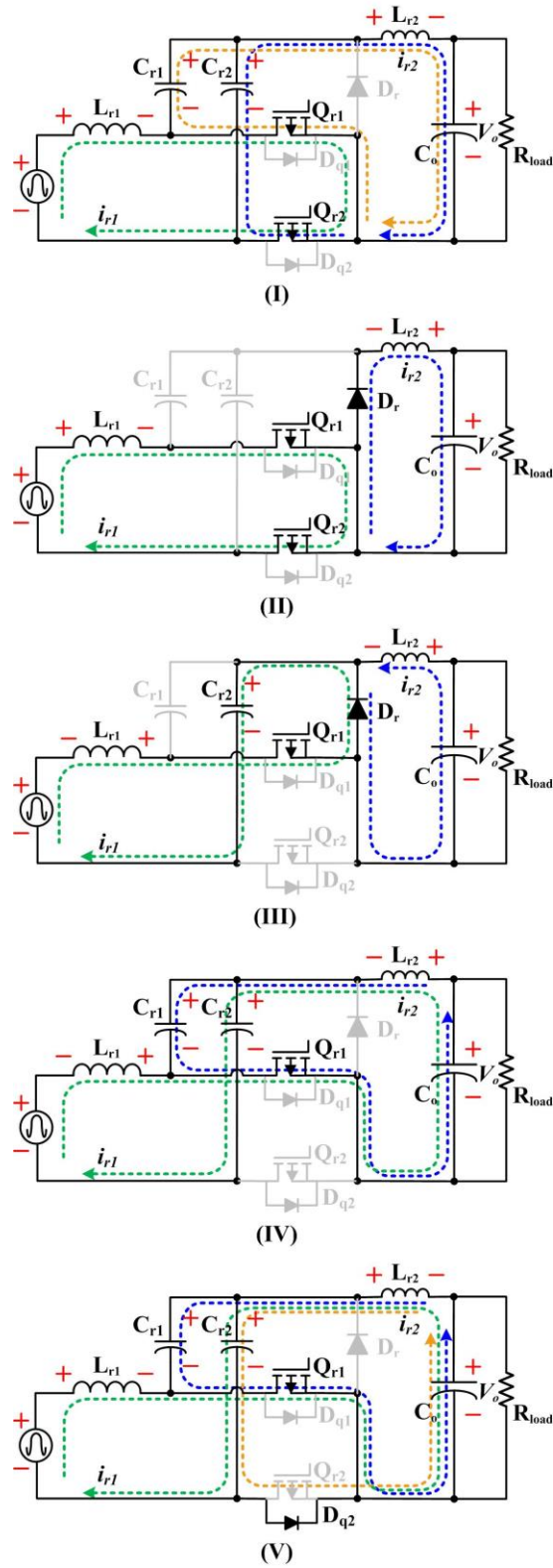


Figure 2.2. Switching sub-intervals of Type 1 converter with a positive voltage input source, during one switching cycle.

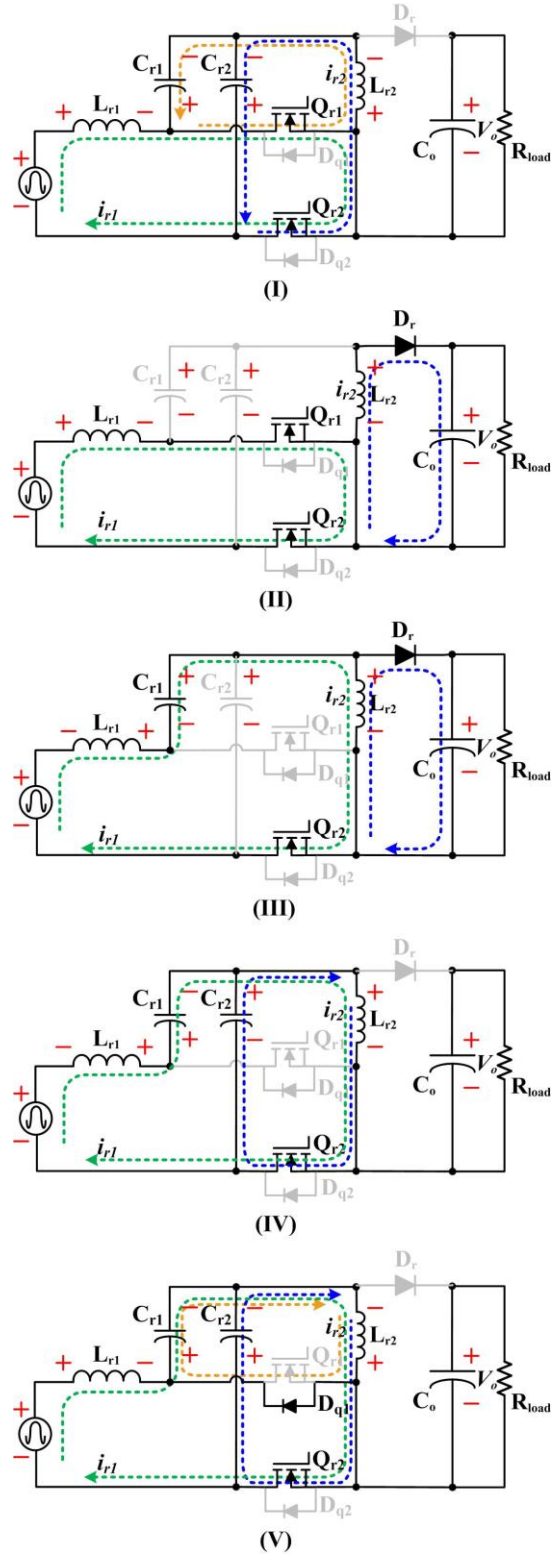


Figure 2.3. Switching sub-intervals for Type 2 converter with a positive voltage input source, during one switching cycle.

At  $t_0$ : (Circuit initial state) Assume that  $i_{r1}$  has an initial value and  $i_{r2}$  is equal to zero.  $v_{cr1}$  and  $v_{cr2}$  have the same maximum positive value.  $Q_{r1}$  is conducting in the entire switching cycle during a positive input voltage. The simplified topology of Type 1 converter with a positive input voltage is illustrated in Fig. 2.4 (a).

*Stage I ( $t_0 \sim t_1$ ):* At  $t_0$ ,  $Q_{r2}$  is turned on at zero voltage [ $v_{ds2}(t_0)$ ] (equal to [ $v_{cr1}(t_0) - v_{cr2}(t_0)$ ]) and zero current [ $i_{ds2}(t_0)$ ].  $L_{r1}$  starts to be charged by the input voltage source, thereby  $i_{r1}$  increases linearly.  $C_{r1}$ ,  $C_{r2}$  ( $C_{r1} = C_{r2}$  are small resonant capacitors) and  $L_{r2}$  begin to resonate near  $f_s$  while  $C_{r1}$  and  $C_{r2}$  release the stored transient energy to  $C_o$ .  $v_{cr1}$  and  $v_{cr2}$  are equal and decrease sinusoidally.

*Stage II ( $t_1 \sim t_2$ ):* At  $t_1$ ,  $v_{cr1}$  and  $v_{cr2}$  drop to zero.  $D_r$  turns on at zero voltage [ $v_{dr}(t_1)$ ], allowing  $i_{r2}$  to freewheel through  $D_r$  ( $i_{dr} = i_{r2}$ ).  $i_{r1}$  continuously increases and  $i_{r2}$  linearly decreases until  $t_2$ .

*Stage III ( $t_2 \sim t_3$ ):* At  $t_2$ ,  $Q_{r2}$  is turned off at zero voltage [ $v_{ds2}(t_2)$ ].  $i_{r1}$  begins to freewheel through  $D_r$  ( $i_{dr} = i_{r1} - i_{r2} > 0$ ).  $L_{r1}$  and  $C_{r2}$  begin to resonate.  $C_{r2}$  stores the energy from  $L_{r1}$  and  $v_{cr2}$  increases; while  $v_{cr1}$  is still zero.  $i_{r2}$  reverses the direction and increases linearly.

*Stage IV ( $t_3 \sim t_4$ ):* At  $t_3$ ,  $i_{r1}$  is less than  $i_{r2}$ .  $D_r$  turns off at both zero voltage [ $v_{dr}(t_3)$ ] and zero current [ $i_{dr}(t_3)$ ].  $L_{r2}$  resonates with  $C_{r1}$  and its energy is transferred to  $C_{r1}$ .  $v_{cr1}$  continuously increases until it is equal to  $v_{cr2}$  at  $t_4$ , where  $v_{ds2}$  is equal to zero.

*Stage V ( $t_4 \sim t_5$ ):* From  $t_4$  to  $t_5$ ,  $v_{cr1}$  and  $v_{cr2}$  increase equally. At  $t_4$ , the body diode  $D_{q2}$  is conducting at zero voltage [ $v_{ds2}(t_4)$ ].  $C_{r1}$ ,  $C_{r2}$  and  $L_{r2}$  again resonate near  $f_s$  while  $C_{r1}$  and  $C_{r2}$  store the transient energy.  $v_{cr1}$  and  $v_{cr2}$  increases sinusoidally until they reach

the maximum value at  $t_5$ .  $L_{r1}$  stores the energy from the input source and  $i_{r1}$  linearly increases to its initial value.

At  $t_5$ :  $D_{q2}$  turns off, followed by turning on  $Q_{r2}$ , both at zero voltage and zero current. Then, the circuit returns to the original state.

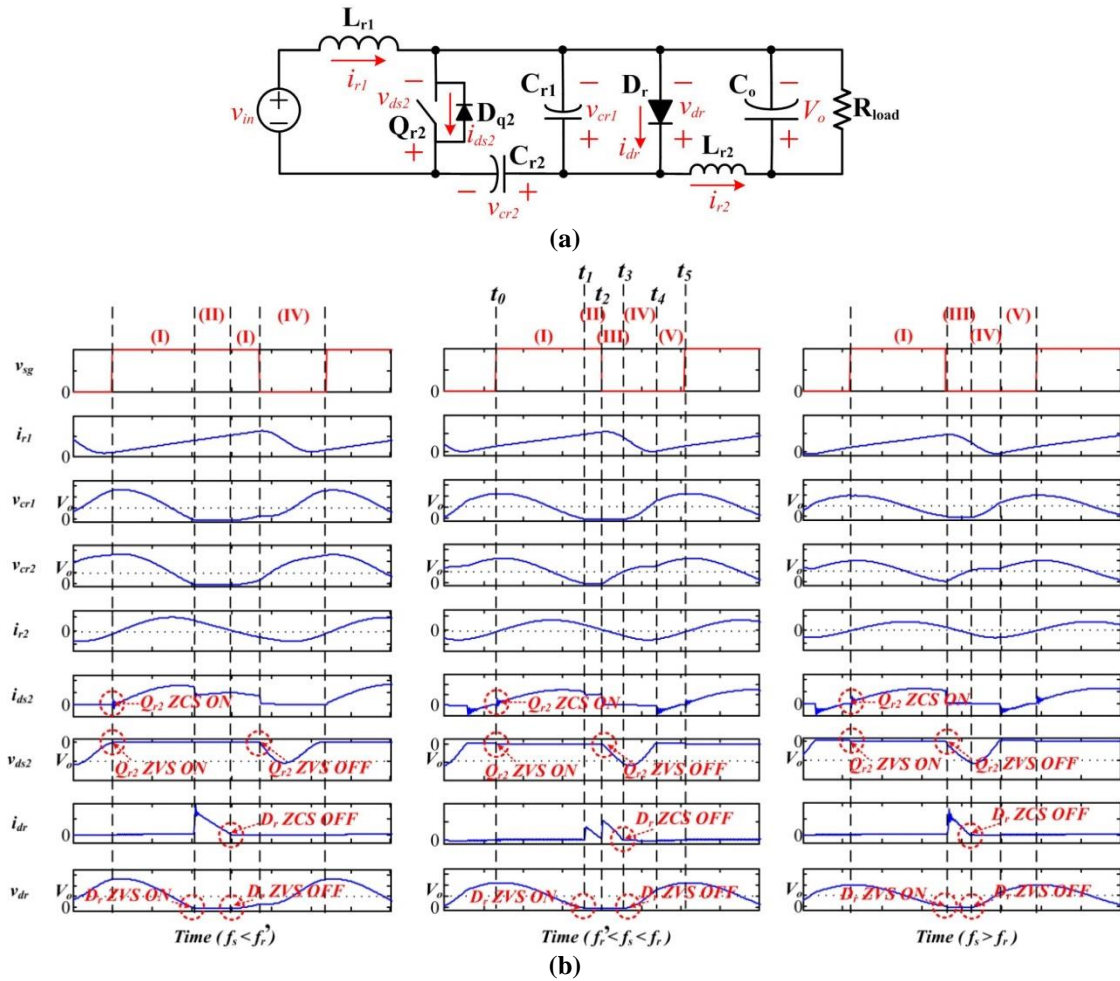


Figure 2.4. (a) Simplified topology of Type 1 converter with a positive input voltage; (b) The voltage and current waveforms of Type 1 converter with a positive input voltage and different switching frequencies.

$L_{r2}$ ,  $C_{r1}$  and  $C_{r2}$  serve as a lossless low drain-to-source impedance branch across  $Q_{r2}$  near the switching frequency. The fundamental component of  $v_{ds2}$  passes through the  $L_{r2}C_{r1}C_{r2}$  network, and then it is rectified to a dc voltage by  $D_r$ . The tuned network stops

resonating in Stage II due to zero state of  $v_{cr1}$  and  $v_{cr2}$ . The input energy is first stored in  $L_{r1}$  during Stages I, II, and V. Afterwards, the transient energy of  $L_{r1}$  is released to the tuned network during Stages III and IV. The LC network transfers the energy to the load through the rectifier diode  $D_r$  during Stages II and III.

When  $f_s < f_r'$ ,  $Q_{r2}$  is turned off after  $i_{r2}$  drops to zero. The circuit returns to Stage I after Stage II; in other words,  $L_{r2}$ ,  $C_{r1}$  and  $C_{r2}$  begin to resonate again after  $i_{r2}$  drops to zero. As soon as  $Q_{r2}$  is tuned off, no current freewheels through  $D_r$  and the circuit jumps into Stage IV instead of Stage III. For the case of  $f_s > f_r$ ,  $Q_{r2}$  is turned off at the end of Stage I, while  $v_{cr1}$  and  $v_{cr2}$  drop to zero, thereby eliminating Stage II.

During the negative voltage input source, the operational circuit of each sub-interval is similar to that in Fig. 2.2. The direction of  $i_{r1}$  is reversed.  $Q_{r2}$  is conducting in the entire switching cycle, while  $Q_{r1}$  is switching analogues to  $Q_{r2}$  during positive input voltage cycle. In other words,  $Q_{r1}$  changes its role with  $Q_{r2}$ . Meanwhile,  $C_{r1}$  switches its role with  $C_{r2}$ .

Type 2 converter has a modified topology in terms of  $D_r$ ,  $L_{r2}$  and transistor body diodes, which consequently changes the transient states of operation. Each switching sub-interval of Type 2 converter for  $f_r' < f_s < f_r$  with a positive voltage input source (see Fig. 2.3) is presented below.

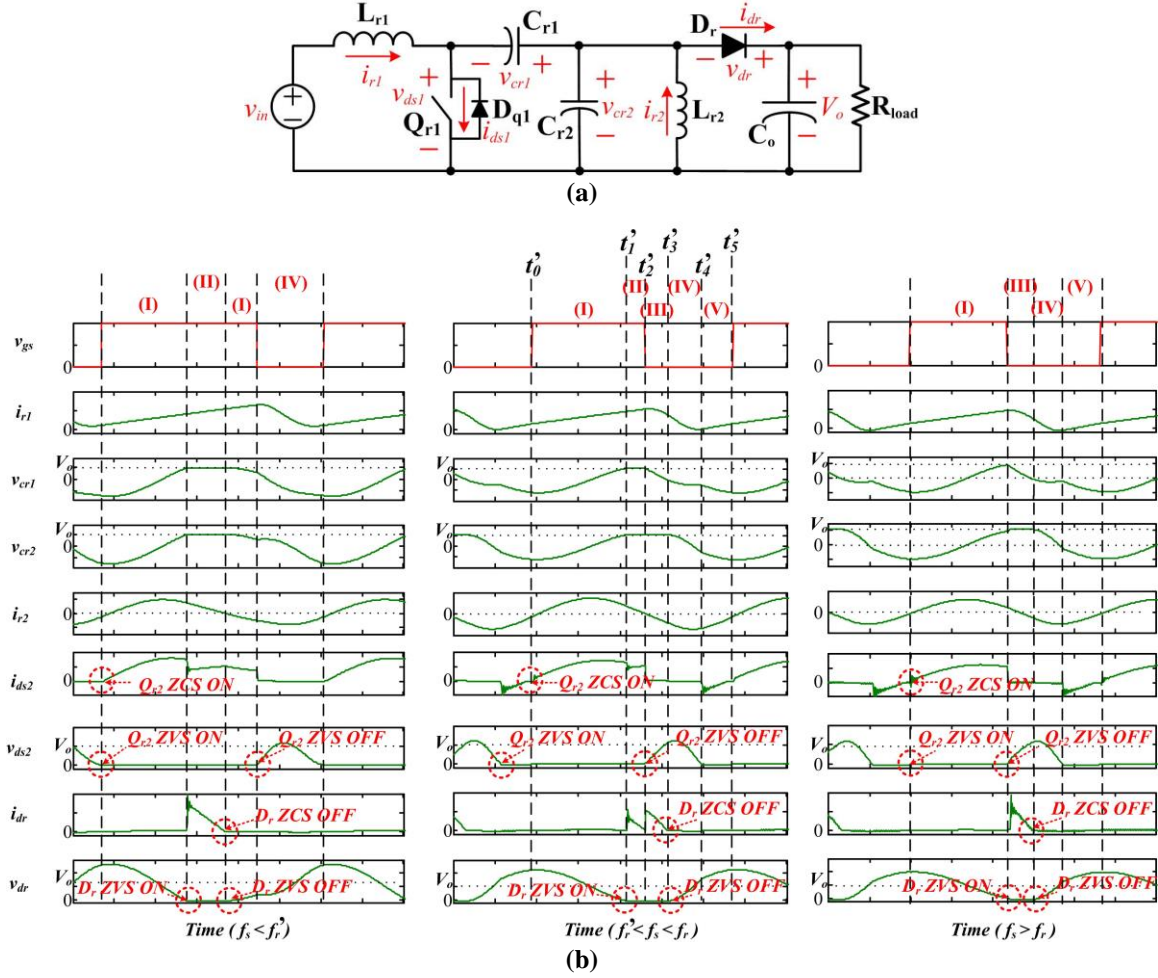


Figure 2.5. (a) Simplified topology of Type 2 converter with a positive input voltage; (b) The voltage and current waveforms of Type 2 converter with a positive input voltage and different switching frequencies.

At  $t_0'$ : (Circuit initial state) Assume that  $i_{r1}$  has an initial value and  $i_{r2}$  is equal to zero. Initially,  $v_{cr1}$  and  $v_{cr2}$  have the same maximum negative value.  $Q_{r2}$  is conducting in the entire switching cycle during a positive input voltage. Fig. 2.5 (a) depicts the simplified topology of Type 2 converter with a positive input voltage.

Stage I ( $t_0' \sim t_1'$ ): At  $t_0'$ ,  $Q_{r1}$  is turned on at zero voltage [ $v_{ds1}(t_0')$ ] (equal to [ $v_{cr2}(t_0') - v_{cr1}(t_0')$ ]) and zero current [ $i_{ds1}(t_0')$ ].  $L_{r1}$  begins to store energy, thereby  $i_{r1}$  increases linearly.  $C_{r1}$ ,  $C_{r2}$  and  $L_{r2}$  resonate at a frequency close to  $f_s$ , while  $C_{r1}$  and  $C_{r2}$

release the transient energy to  $L_{r2}$ .  $v_{cr1}$  and  $v_{cr2}$  are equal and vary sinusoidally until they are equal to  $V_o$  at  $t_1'$ .

*Stage II ( $t_1' \sim t_2'$ ):* From  $t_1'$ ,  $v_{cr1}$  and  $v_{cr2}$  are equal to  $V_o$ .  $D_r$  turns on at zero voltage [ $v_{dr}(t_1')$ ], allowing  $i_{r2}$  to freewheel through  $D_r$  ( $i_{dr}=i_{r2}$ ).

*Stage III ( $t_2' \sim t_3'$ ):* At  $t_2'$ ,  $Q_{r1}$  is turned off at zero voltage [ $v_{ds1}(t_2')$ ].  $i_{r2}$  reverses the direction and linearly increases, but it is less than  $i_{r1}$ . The current freewheels through  $D_r$  ( $i_{dr}=i_{r1}-i_{r2}>0$ ) to compensate the difference between  $i_{r1}$  and  $i_{r2}$ .  $L_{r1}$  and  $C_{r1}$  begin to resonate.  $C_{r1}$  releases the energy to  $C_o$  and  $v_{cr1}$  decreases; however,  $v_{cr2}$  is still equal to  $V_o$ .

*Stage IV ( $t_3' \sim t_4'$ ):* From  $t_3'$  to  $t_4'$ ,  $i_{r1}$  is less than  $i_{r2}$ , leaving no current to freewheel through  $D_r$ .  $D_r$  turns off at both zero voltage [ $v_{dr}(t_3')$ ] and zero current [ $i_{dr}(t_3')$ ] at  $t_3'$ .  $L_{r2}$  and  $C_{r2}$  resonate until  $v_{cr2}$  is equal to  $v_{cr1}$  at  $t_4'$ .

*Stage V ( $t_4' \sim t_5'$ ):* From  $t_4'$  to  $t_5'$ ,  $v_{cr1}$  and  $v_{cr2}$  are negative and equally increase until they reach the maximum. At  $t_4'$ , the body diode  $D_{q1}$  is conducting at zero voltage [ $v_{ds1}(t_4')$ ].

At  $t_5'$ :  $D_{q1}$  turns off, followed by turning on  $Q_{r1}$  both at zero voltage and zero current. Then the circuit returns to the original state.

During the negative voltage input source, the direction of  $i_{r1}$  is reversed.  $Q_{r1}$  is conducting in the entire switching cycle, while  $Q_{r2}$  is switching analogues to  $Q_{r1}$  during a positive input voltage cycle. The LC network in Type 2 converter serves the same functionality as that in Type 1 converter. However,  $v_{cr1}$  and  $v_{cr2}$  are alternating, which leads to smaller root-mean-square (RMS) value than those in Type 1 converter.

## 2.2 Circuit Analyses of Resonant AC-DC Converters

### 2.2.1 Steady-state Operating Characteristics

The analyses of the steady-state characteristics are based on equivalent circuit models corresponding to different switching sub-intervals, illustrated in Fig. 2.6. All the analyses are based on Type 1 converter in the operating region  $f_r' < f_s < f_r$  (see Fig. 2.4), while similar procedure can be adapted for Type 2 converter.  $C_o$  has much smaller impedance at switching frequency in comparison to  $R_{load}$ , thereby it performs similar to a voltage source  $V_o$ . The values of  $C_{r1}$  and  $C_{r2}$  are set equal to  $C_r$  for the symmetry of the configuration. The transient waveforms and time intervals are inspected from Fig. 2.4.

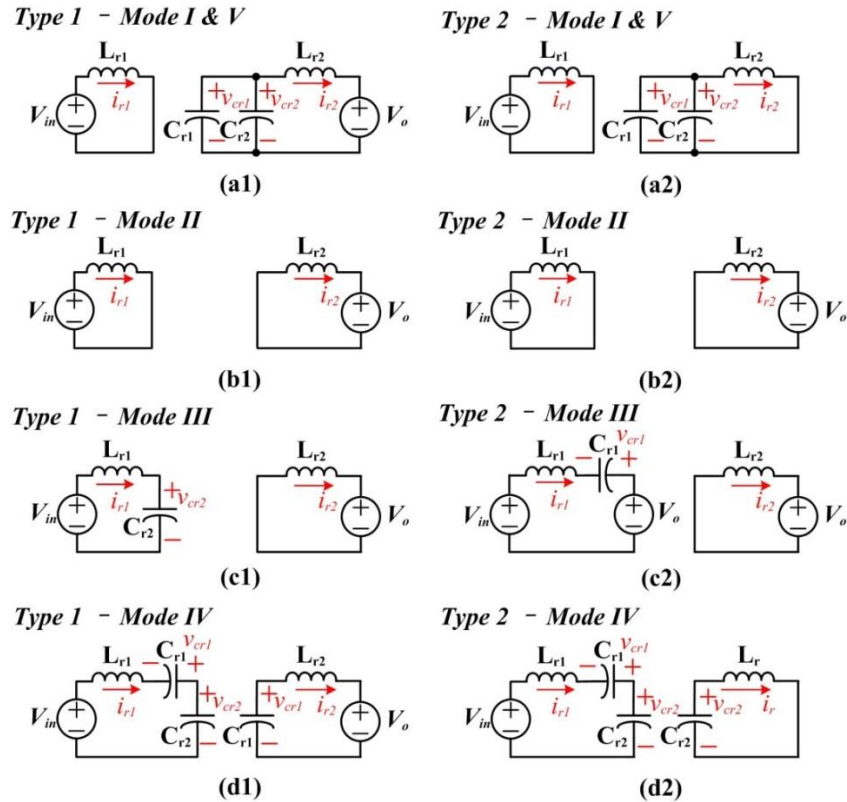


Figure 2.6. The equivalent circuit models of Type 1 converter: (a1) corresponding to Stages I and V; (b1) Stage II; (c1) Stage III; (d1) Stage IV. The equivalent circuit models of Type 2 converter: (a2) corresponding to Stages I and V; (b2) Stage II; (c2) Stage III; (d2) Stage IV.

In Stages I and V,  $L_{r1}$  is directly connected to  $V_{in}$  while the network  $L_{r2}C_{r1}C_{r2}$  is connected to  $V_o$  (see Fig. 2.6(a1)).  $C_{r1}$  and  $C_{r2}$  release the energy to the load during resonance. The governing equations in terms of  $i_{r1}$ ,  $i_{r2}$ ,  $v_{cr1}$  and  $v_{cr2}$  are presented as

$$\left\{ \begin{array}{l} \frac{di_{r1}(t)}{dt} = \frac{V_{in}}{L_{r1}} \end{array} \right. \quad (2-1)$$

$$\left\{ \begin{array}{l} \frac{di_{r2}(t)}{dt} = \frac{v_{cr1}(t) - V_o}{L_{r2}} \end{array} \right. \quad (2-2)$$

$$\left\{ \begin{array}{l} \frac{dv_{cr1}(t)}{dt} = -\frac{i_{r2}(t)}{2C_r} \end{array} \right. \quad (2-3)$$

$$\left\{ \begin{array}{l} v_{cr2}(t) = v_{cr1}(t) \end{array} \right. \quad (2-4)$$

Applying the initial condition  $i_{r2}(t_0)=0$ , the transient states can be written as

$$\left\{ \begin{array}{l} i_{r1}^I(t) = \frac{V_{in}}{L_{r1}}(t - t_0) + i_{r1}(t_0) \end{array} \right. \quad (2-5)$$

$$\left\{ \begin{array}{l} i_{r2}^I(t) = \frac{v_{cr1}(t_0) - V_o}{Z_{r1}} \sqrt{2} \sin \frac{1}{\sqrt{2}} \omega_{r1}(t - t_0) \end{array} \right. \quad (2-6)$$

$$\left\{ \begin{array}{l} v_{cr1}^I(t) = v_{cr2}^I(t) = [v_{cr1}(t_0) - V_o] \cos \frac{1}{\sqrt{2}} \omega_{r1}(t - t_0) + V_o \end{array} \right. \quad (2-7)$$

where,  $\omega_{r1}=1/\sqrt{L_{r2}C_r}$  is the angular resonant frequency of  $L_{r2}C_r$  network, and  $Z_{r1}=\sqrt{L_{r2}/C_r}$  is the characteristic impedance of  $L_{r2}C_r$  network.

During Stage II (see Fig. 2.6(b1)), the voltage across  $L_{r1}$  is  $V_{in}$  and the voltage across  $L_{r2}$  is  $V_o$ . The governing equations can be written as

$$\left\{ \begin{array}{l} \frac{di_{r1}(t)}{dt} = \frac{V_{in}}{L_{r1}} \end{array} \right. \quad (2-8)$$

$$\left\{ \begin{array}{l} \frac{di_{r2}(t)}{dt} = -\frac{V_o}{L_{r2}} \end{array} \right. \quad (2-9)$$

The transient states are calculated as

$$\left\{ \begin{array}{l} i_{r1}''(t) = \frac{V_{in}}{L_{r1}}(t-t_1) + i_{r1}(t_1) \end{array} \right. \quad (2-10)$$

$$\left\{ \begin{array}{l} i_{r2}''(t) = -\frac{V_o}{L_{r2}}(t-t_1) + i_{r2}(t_1) \end{array} \right. \quad (2-11)$$

$$\left\{ \begin{array}{l} v_{cr1}''(t) = v_{cr2}''(t) = 0 \end{array} \right. \quad (2-12)$$

During Stage III (see Fig. 2.6(c1)),  $C_{r2}$  stores the energy from  $L_{r1}$ , while  $L_{r2}$  releases the energy to the load. The governing equations are presented as

$$\left\{ \begin{array}{l} \frac{di_{r1}(t)}{dt} = \frac{V_{in} - v_{cr2}(t)}{L_{r1}} \end{array} \right. \quad (2-13)$$

$$\left\{ \begin{array}{l} \frac{di_{r2}(t)}{dt} = -\frac{V_o}{L_{r2}} \end{array} \right. \quad (2-14)$$

$$\left\{ \begin{array}{l} \frac{dv_{cr2}(t)}{dt} = \frac{i_{r1}(t)}{C_r} \end{array} \right. \quad (2-15)$$

Therefore,  $i_{r2}$  decreases linearly to zero and  $v_{cr2}$  linearly increases, with the boundary condition  $v_{cr2}(t_2)=0$ , yielding

$$\left\{ \begin{array}{l} i_{r1}'''(t) = i_{r1}(t_2) \cos \omega_{r2}(t-t_2) + \frac{V_{in}}{Z_{r2}} \sin \omega_{r2}(t-t_2) \end{array} \right. \quad (2-16)$$

$$\left\{ \begin{array}{l} i_{r2}'''(t) = -\frac{V_o}{L_{r2}}(t-t_2) + i_{r2}(t_2) \end{array} \right. \quad (2-17)$$

$$\left\{ \begin{array}{l} v_{cr1}'''(t) = 0 \\ v_{cr2}'''(t) = -V_{in} \cos \omega_{r1}(t-t_2) + i_{r1}(t_2)Z_{r2} \sin \omega_{r2}(t-t_2) + V_{in} \end{array} \right. \quad (2-18)$$

where,  $\omega_{r2}=1/\sqrt{L_{r1}C_r}$  is the angular resonant frequency of  $L_{r1}C_r$  network, and  $Z_{r2}=\sqrt{L_{r1}/C_r}$  is the characteristic impedance of  $L_{r1}C_r$  network.

In Stage IV,  $L_{r1}$  is resonating with  $C_{r1}$  and  $C_{r2}$ , while  $L_{r2}$  is resonating with  $C_{r1}$  (see Fig. 2.6(d1)), yielding

$$\left\{ \begin{array}{l} \frac{di_{r1}(t)}{dt} = \frac{V_{in} + v_{cr1}(t) - v_{cr2}(t)}{L_{r1}} \end{array} \right. \quad (2-20)$$

$$\left\{ \begin{array}{l} \frac{di_{r2}(t)}{dt} = \frac{v_{cr1}(t) - V_o}{L_{r2}} \end{array} \right. \quad (2-21)$$

$$\left\{ \begin{array}{l} \frac{dv_{cr1}(t)}{dt} = -\frac{i_{r1}(t) + i_{r2}(t)}{C_r} \end{array} \right. \quad (2-22)$$

$$\left\{ \begin{array}{l} \frac{dv_{cr2}(t)}{dt} = \frac{i_{r1}(t)}{C_r} \end{array} \right. \quad (2-23)$$

By applying boundary conditions  $v_{cr1}(t_3)=0$ ,  $v_{cr2}(t_3)=V_o$ ,  $i_{r1}(t_3)+i_{r2}(t_3)=0$ , one can find that

$$\left\{ \begin{array}{l} i_{r1}^{IV}(t) = i_{r1}(t_3) \cos \omega_{r2}(t-t_3) + \frac{V_{in} - V_o}{Z_{r2}} \sin \omega_{r2}(t-t_3) \end{array} \right. \quad (2-24)$$

$$\left\{ \begin{array}{l} i_{r2}^{IV}(t) = i_{r2}(t_3) \cos \omega_{r1}(t-t_3) - \frac{V_o}{Z_{r1}} \sin \omega_{r1}(t-t_3) \end{array} \right. \quad (2-25)$$

$$\left\{ \begin{array}{l} v_{cr1}^{IV}(t) = -V_o \cos \omega_{r1}(t-t_3) + V_o \end{array} \right. \quad (2-26)$$

$$\left\{ \begin{array}{l} v_{cr2}^{IV}(t) = [V_o - V_{in}] \cos \omega_{r2}(t-t_3) + i_{r1}(t_3) Z_{r2} \sin \omega_{r2}(t-t_3) + V_{in} \end{array} \right. \quad (2-27)$$

$L_{r1}$  and  $L_{r2}$  are set equal to  $L_r$  for ease of calculation ( $\omega_{r1}=\omega_{r2}=\omega_r$  and  $Z_{r1}=Z_{r2}=Z_r$ ).

The analysis is valid when  $L_{r1}$  is slightly different from  $L_{r2}$ . However, the switching sub-intervals and analyses can be different when  $L_{r1} \gg L_{r2}$ , which is discussed in Chapter 3.

In steady-state operation, the integral of the resonant inductor voltage ( $v_{Lr1}$ ) over one switching period must be zero, which yields

$$\int_{t_0}^{t_0+T_s} v_{Lr1}(t) dt = \int_{t_0}^{t_0+T_s} [v_{cr1}(t) - v_{cr2}(t) + V_{in}] dt = 0 \quad (2-28)$$

By setting the resonant period  $t_{r2}=t_4-t_3=T_{r2}/4=\pi/2\omega_r$ , one can find that

$$F[V_{in}, V_o, i_{r1}(t_2)] = 0 \quad (2-29)$$

On the other hand, the integral of the output capacitor current ( $i_{cro}$ ) over one switching period being zero, yields

$$\int_{t_0}^{t_0+T_s} i_{cro}(t) dt = \int_{t_0}^{t_0+T_s} [i_{dr}(t) - \frac{V_o}{R_L}] dt = 0 \quad (2-30)$$

Applying the boundary condition  $v_{cr2}(t_3)=V_o$ , one can find another relationship that

$$G[V_{in}, V_o, i_{r1}(t_2), R_L, f_s] = 0 \quad (2-31)$$

Solving Eqs. (2-29)~(2-31) yields

$$\left\{ \begin{aligned} A_x \left( \frac{1}{f_s} + \frac{2-\pi}{2\omega_r} + \frac{\sin \theta_y}{\omega_r} \right) + A_y \frac{\pi-4}{2\omega_r} - A_x A_y \frac{2}{f_s R_L} + \frac{Z_r (\cos \theta_y - 2)}{\omega_r} = 0 \end{aligned} \right. \quad (2-32)$$

$$\left\{ \begin{aligned} A_x (1 - \cos \theta_y) - A_y + Z_r \sin \theta_y = 0 \end{aligned} \right. \quad (2-33)$$

where, the ratio of input voltage to input current is  $A_x=V_{in}/i_{r1}(t_2)$ , the ratio of output voltage to input current is  $A_y=V_o/i_{r1}(t_2)$ , and  $\theta_y=2\omega_r V_o/f_s R_L i_{r1}(t_2)$ . Therefore, using Eq. (2-32) and Eq. (2-33), the dc-dc instantaneous voltage gain ( $A=A_y/A_x$ ) of the converter in steady state can be calculated as

$$A = 1 + \frac{1}{\frac{1}{4Q} \left[ 1 - \sqrt{(1+2Q)^2 - 8Q \left( 1 + \frac{8-\pi}{4\pi} \gamma \right)} \right] - \frac{1}{2}} \quad (2-34)$$

where,  $Q=Z_r/R_L$  is the characteristic impedance of multi-resonant network,  $\gamma=f_s/f_r$  denotes the normalized switching frequency. The voltage ratio is load-dependent; meanwhile, it increases as the switching frequency decreases, shown in Fig. 2.7. The steady-state analyses are valid for Type 2 converter, even though their transient states are different.

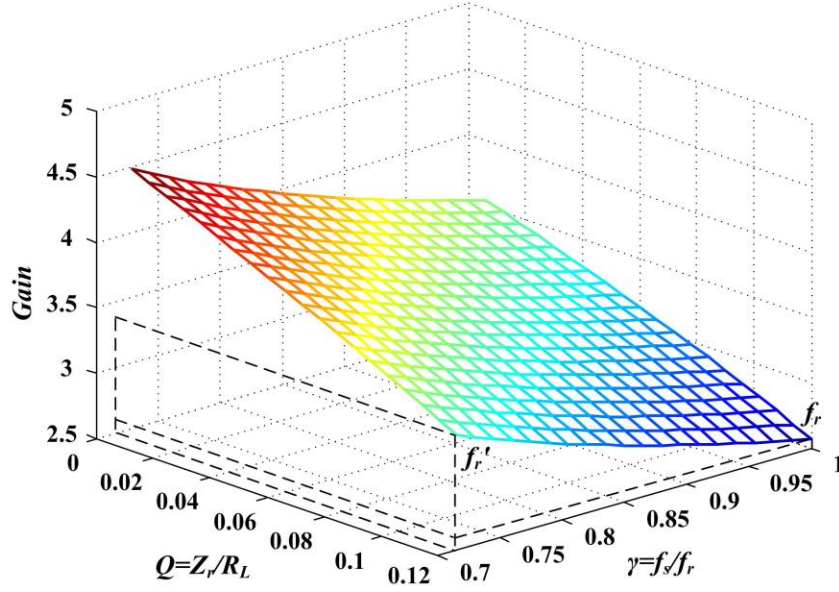


Figure 2.7. Voltage gain characteristics of the resonant converter.

By applying boundary condition  $i_{r2}(t_0)=0$  and setting the transistor turn-on period to  $t_{on}=t_1-t_0=T_s/2$  in Eq. (2-6) and Eq. (2-7), one can find that  $f_r=\sqrt{2}f_r'$ . The switching period should be larger than addition of the resonant periods, corresponding to  $f_r$  and  $f_r'$ .

$$t_r + t_r' < \frac{1}{f_s} \quad (2-35)$$

Therefore, the soft-switching frequency range can be presented as

$$\frac{1}{\sqrt{2}} < \gamma < 1 \quad (2-36)$$

According to Eq. (2-34), the load impedance should match the network impedance and satisfy Eq. (2-37).

$$Q < \frac{1}{2} + \frac{8-\pi}{4\pi} \gamma - \frac{1}{2} \sqrt{\left(1 + \frac{8-\pi}{2\pi} \gamma\right)^2 - 1} \quad (2-37)$$

At wide range of loads and input voltages, output voltage can be regulated at a constant value by adjusting the switching frequency. The range of voltage gain may be

limited by the switching frequency region; however, it can be increased by using module on/off control, which is discussed in Section 2.3.2.

### 2.2.2 Electrical Stresses

For Type 1 converter, the maximum values of voltages across the resonant capacitors, at  $t_0$ , are equal, and by applying the boundary condition  $v_{cr1}(t_1)=0$  into Eq. (2-7), one can find that

$$v_{cr1,max} = v_{cr2,max} = (1 - \cos^{-1} \frac{\pi}{\sqrt{2}\gamma}) AV_{in} \quad (2-38)$$

$v_{cr1,max}$  and  $v_{cr2,max}$  are close to twice of  $V_o$  if  $\gamma$  is close to  $1/\sqrt{2}$ . Since the transistors  $Q_{r1}$  and  $Q_{r2}$  are in parallel with two resonant capacitors, the drain-to-source voltage across each transistor ( $v_{ds}$ ) is equal to the voltage compensation between two capacitors,

$$v_{ds}(t) = v_{cr1}(t) - v_{cr2}(t) \quad (2-39)$$

The transistor voltage reaches its maximum value during Stage IV. By applying the boundary condition  $v_{cr1}(t_4) - v_{cr2}(t_4) = 0$  into Eq. (2-26) and Eq. (2-27), one can find the maximum voltage stress on the transistor from the differential equation  $[v_{cr1}^{IV}(t) - v_{cr2}^{IV}(t)]' = 0$ :

$$v_{ds,max} = -[(2 - \frac{1}{A}) \sqrt{\frac{1}{1 + (\frac{A-1}{2A-1})^2}} + (1 - \frac{1}{A}) \sqrt{\frac{1}{1 + (\frac{2A-1}{A-1})^2}} - (1 - \frac{1}{A})] AV_{in} \quad (2-40)$$

$v_{ds,max}$  is close to  $-V_o$ , which is half of  $-v_{cr1,max}$ . Note that  $v_{cr1,max}$  and  $v_{cr2,max}$  increase as the switching frequency increases while  $v_{ds,max}$  remains nearly constant. Since the rectifier diode is in parallel with one resonant capacitor, the maximum voltage stress on diode is equal to the maximum voltage stress on the resonant capacitor.

$$v_{dr,max} = v_{cr1,max} \quad (2-41)$$

For Type 2 converter, the maximum voltage stresses on resonant capacitors are

$$v_{cr1,max} = v_{cr2,max} = (\cos^{-1} \frac{\pi}{\sqrt{2}\gamma}) AV_{in} \quad (2-42)$$

$v_{cr1,max}$  and  $v_{cr2,max}$  are close to  $-V_o$  if  $\gamma$  is close to  $1/\sqrt{2}$ . However,  $v_{ds,max}$  is the same as that in Type 1 converter. Therefore, Type 2 converter has less voltage stresses across resonant capacitors and rectifier diode in comparison to Type 1 converter; nevertheless, the voltage stresses across transistors are equal. In addition, both converters have less voltage stresses on the transistors due to existence of two split resonant capacitors.

For both two converters, when the converter is operating in steady-state condition, one can obtain from the input/output power balance that

$$V_{in} I_{in} = \frac{V_o^2}{R_L} \quad (2-43)$$

Therefore, the average current in a switching period carried by  $L_{r1}$  can be obtained as

$$i_{r1,avg} = \frac{A^2}{R_L} V_{in} \quad (2-44)$$

Since the peak current  $i_{r1,pk}$  carried by  $L_{r1}$  appears at  $t_2$ , it can be calculated by solving Eqs. (2-5), (2-30) and (2-44):

$$i_{r1,pk} = i_{r1}(t_2) = \frac{V_{in}}{2} \left[ \frac{A^2}{R_L} + \frac{1}{2L_r f_s} - \frac{1}{8L_r f_r} + \sqrt{\left( \frac{A^2}{R_L} + \frac{1}{2L_r f_s} - \frac{1}{8L_r f_r} \right)^2 - \frac{4A}{f_s L_r R_L}} \right] \quad (2-45)$$

Due to the fact that  $L_{r2}$  is in series with the load, the average current in a switching period carried by  $L_{r2}$  is equal to that carried by  $R_L$ , therefore

$$i_{r2,avg} = \frac{A}{R_L} V_{in} \quad (2-46)$$

The peak current  $i_{r2,peak}$  carried by  $L_{r2}$  appears during Stage I where  $i_{r2}(t)$  satisfies Eq. (2-4), yielding

$$i_{r2,pk} = \sqrt{2} \frac{v_{cr1}(t_0) - V_o}{R_L} = -\sqrt{2} (R_L \cos \frac{\pi}{\sqrt{2}\gamma})^{-1} AV_{in} \quad (2-47)$$

According to the analyses in Chapter 2.2.1, the current through the transistors would be

$$i_{ds}(t) = i_{r1}(t) + \frac{1}{2}i_{r2}(t) \quad (2-48)$$

Thereby, the average current and the peak current through the transistors can be acquired from Eqs. (2-5), (2-6), (2-10) and (2-11) as

$$\begin{cases} i_{ds,avg} = \frac{1}{T_{s,II,V}} \int [i_{r1}(t) + \frac{1}{2}i_{r2}(t)]dt = [\frac{\pi}{4Z_r\gamma} + \frac{A\gamma}{2\pi Z_r} (1 - \cos^{-1} \frac{\pi}{\sqrt{2}\gamma})]V_{in} \end{cases} \quad (2-49)$$

$$\begin{cases} i_{ds,pk} \approx \frac{1}{2}i_{r1,pk} + \frac{1}{2}i_{r2,pk} \end{cases} \quad (2-50)$$

Moreover, the average current and the peak current through the diode can be expressed as

$$\begin{cases} i_{dr,avg} = i_{r2,avg} = \frac{A}{R_L}V_{in} \end{cases} \quad (2-51)$$

$$\begin{cases} i_{dr,pk} \approx \max(i_{r1,pk}, i_{r2,pk}) \end{cases} \quad (2-52)$$

Note that the current stress on the diode is much less than those on the transistors. The diode is conducting for rectification during a very short period in comparison to quasi-resonant topologies.

In summary, the electrical stresses of active components and passive components are load-dependent. They can be adjusted through a variable switching frequency. One can reduce the stresses by either increasing the switching frequency or reducing the load resistance. Furthermore, the voltage stresses across the transistors and the current stress on the diode are less than other resonant topologies [89]-[91], [97]-[99].

## 2.3 Gate Drive and Controller

### 2.3.1 Resonant Gate Drive

The effect of gate drive on overall performance and efficiency of the converter is critical, especially in high switching frequency operation. Large amount of energy is

dissipated by using conventional square voltage hard-switched gating, since there is no energy recovery [135], [136]. At high switching frequency, resonant gating can significantly reduce the gate drive losses by recovering gate charge energy each cycle. Many of efforts focus on designing active RGD circuits, which consist of auxiliary switch bridges and passive components [135]-[140]. In these circuits, the turning-on and turning-off times are controllable, which makes them suitable to adjust duty ratio or switching frequency. However, the auxiliary switch bridges require additional drivers, which consequently increase the circuit size and losses. Furthermore, at high switching frequency, it becomes difficult to catch zero voltage and zero current crossing by using an active bridge drive.

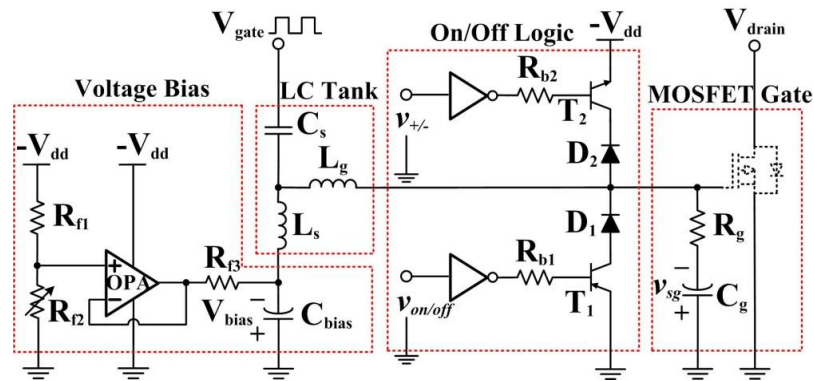


Figure 2.8. Resonant gate drive circuit for Type 1 converter.

To reduce driver complexity, passive RGD circuits are investigated for fixed frequency and fixed duty ratio gate drives [97]-[99]. Such drive circuits utilize LC resonant tank to generate trapezoidal or sinusoidal voltage gating. The gate signals, which are generated by relaxation oscillators, pass through LC resonant tanks. The LC networks behave as pass filters to acquire the demanded harmonics of gate signals, which cause no mutation in gating voltage. Passive RGD circuits generate gating signals with fixed

frequency and fixed duty ratio. They are suitable for converters where fixed switching operation is demanded to acquire maximum efficiency, i.e. the proposed converter in this dissertation. The power control strategy can be achieved by using simple module on/off control, which has advantages in terms of fast response, easy implementation and high stability.

A low-loss passive RGD circuit is adopted in the proposed design to achieve resonant gating (see Fig. 2.8). A tuned LC tank sets the transfer function from the oscillator to the transistor gate. The resonant tank is designed to extract the fundamental component of the gate signal, which consequently generates a sinusoidal gating. The input capacitor  $C_s$  is resonant with the shunt inductor  $L_s$  to perform as a high-pass filter.  $L_g$  is selected to resonate with the parasitic gate capacitor  $C_g$  for a sinusoidal gating at fundamental component of switching frequency. Second resonant frequency apparent in the transfer function is damped by  $L_g$  and the gate resistance  $R_g$ , in order to avoid higher frequency oscillation. The frequency response of the transfer function is depicted in Fig. 2.9. By properly adjusting  $C_s$  and  $L_s$ , one can set the magnitude and the bandwidth of oscillation.

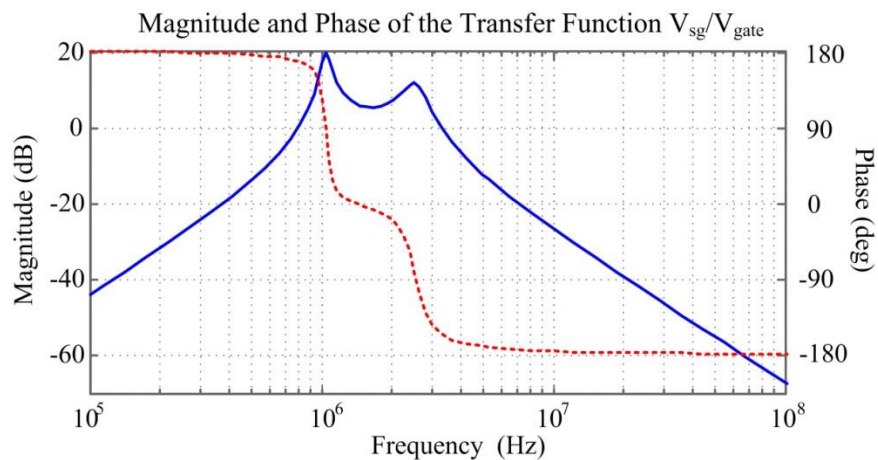


Figure 2.9. Frequency response of the transfer function of the resonant tank.

A blocking capacitor  $C_{bias}$  is connected to  $L_s$  in the shunt leg.  $C_{bias}$  is charged by a voltage follower, thereby maintaining a bias voltage close to MOSFET threshold voltage at its gate. By adjusting the resistor  $R_{f2}$  of the voltage divider, the bias voltage of the resonant gating can be regulated, which in turn sets the switching duty ratio. The damping resistor  $R_{f3}$  is located between  $C_{bias}$  and the voltage follower in order to block high-order harmonic feedback. In addition,  $R_{f3}$  and  $C_{bias}$  should be carefully selected to acquire fast transient response.

### 2.3.2 Module On/Off Control Strategy

The converter is intended to operate at fixed switching frequency and fixed switching duty ratio to achieve high efficiency operation, though the voltage gain can be regulated by variable switching frequency. On the other hand, module on/off control strategy realizes the advantages in terms of easy implementation, fast transient response, wide load range and higher efficiency [97], [140]. The output voltage regulation is achieved through enabling the converter module and delivering power when the output voltage falls below a demanded threshold. When the output voltage rises above the threshold, the module is disabled, leaving the output capacitor to feed the load.

This control scheme separates the control and the power processing, which in turn increases the circuit efficiency and operation accuracy. When the module is enabled, the converter operates at a fixed high-efficiency point; when disabled, no power is delivered through the circuit, which consequently removes additional loss. A module hysteretic on/off control is a varied-module-frequency control and dependent on feedback sampling frequency. In comparison to hysteretic control, module PWM on/off control is a fixed-module-frequency control and is superior in terms of faster response and more accuracy

[141]. Functionally, the converter module is enabled and disabled at a fixed on/off frequency and an adjustable on/off duty ratio. The load power is regulated by adjusting the module on/off duty ratio.

To achieve the PWM on/off control strategy, a logical on/off module is added on the gate driver for Type 1 converter, as demonstrated in Fig. 2.8. The directions of BJT-diode bridges are reversed in the case of Type 2 converter. The PWM comparator delivers the enabling signal  $v_{on/off}$  to  $T_1$ , according to the controller feedback. When  $T_1$  is turned on, the MOSFET gate is pulled to ground and disabled. High output resistance of  $D_1$  and  $T_1$  blocks the high-frequency oscillating signal from the LC tank. When  $T_1$  is turned off, the voltage follower starts to charge  $C_{bias}$ , thereby the biased resonant gating is recovered at MOSFET gate. The values of  $R_{f3}$  and  $C_{bias}$  determine the charging time, corresponding to the transient response to enable energy recovery.

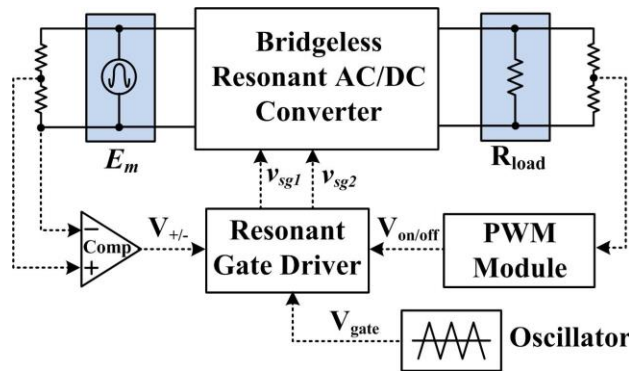


Figure 2.10. Block diagram of module on/off control and polarity identification for resonant switching and gating.

Another logical bridge including  $T_2$  and  $D_2$  is added on the gate driver to implement input polarity identification. Based on the polarity of input, the comparator delivers  $v_{+/-}$  to  $T_2$  with choice of either leaving the gate resonant or enabling the gate all

the time. Fig. 2.10 presents the block diagram of the control system. The resonant gating signals, generated by the gate driver and control scheme, consist of three main frequency components (see Fig. 2.11). During each half cycle of  $v_{in}$ , one of the MOSFETs is enabled all the time while the other one is disabled during PWM module-off time. During the module-on time, one MOSFET gate is resonant at a switching frequency much higher than on/off modulation frequency.

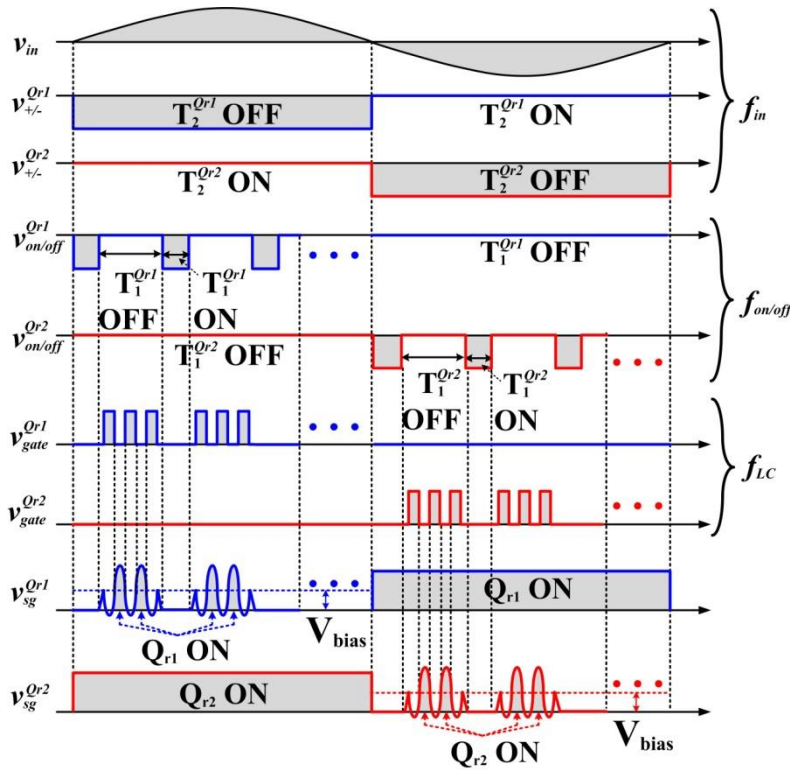


Figure 2.11. Resonant gating signal corresponding to on/off control signal and polarity identification signal, in the case of Type 1 converter.

The closed-loop simulation with a low-frequency alternating input voltage is demonstrated in Fig. 2.12. The results confirm the fast transient response of module PWM on/off control scheme as well as good performance of the power converter at low-amplitude input voltages. Increasing the on/off modulation frequency can decrease the

size of output capacitor. However, the driver efficiency decreases as the modulation frequency increases, which brings the tradeoff between the driver efficiency and capacitor size. In spite of this, most of main power components are based on high soft-switching frequency, enabling miniaturization and high efficiency operation.

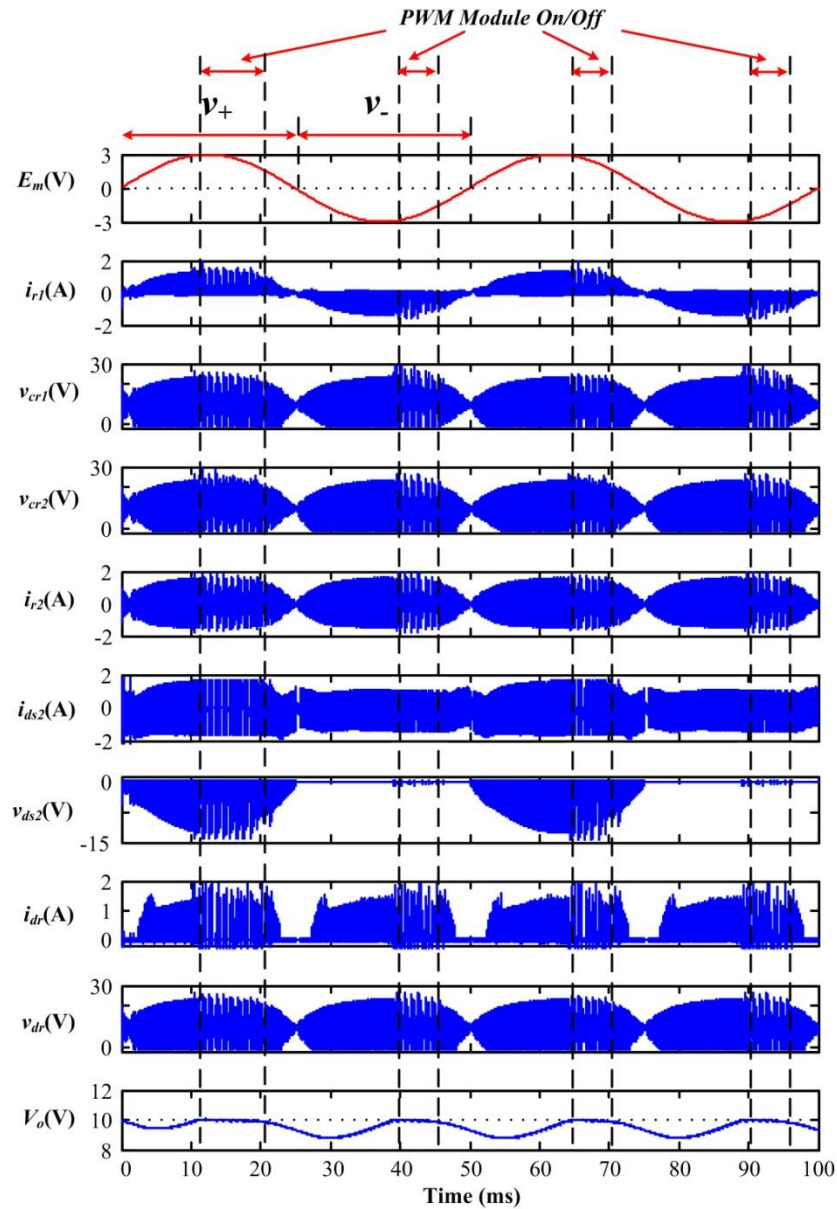


Figure 2.12. Simulation waveforms of Type 1 converter with 2-Vrms alternating input voltage, using module on/off control.

## 2.4 Testing and Discussion

### 2.4.1 Prototypes and Experimental Results

Experimental tests are presented in this section to elaborate performance of the proposed converter particularly under light-load condition and limited footprint. A 5-mm  $\times$  6-mm, 100-mg prototype of power stage, illustrated in Fig. 2.13, is developed to validate 2-MHz resonant operation of Type 1 converter. Table 2.1 lists parameters of all the components adopted in resonant power stage and resonant gate driver. The resonant switching frequency is set to 2 MHz with consideration of gate charge speed and miniature package of the commercially available transistors. Higher switching frequency can be achieved through radio frequency transistors with larger package sizes. According to the input energy sources referred in Chapter 1.1.1, the input voltage is set to a range of 0.25-3  $V_{\text{rms}}$  while the maximum average current reaches up to 300 mA. A power amplifier circuit is fabricated to emulate the alternating input energy source.

TABLE 2.1  
COMPONENT PARAMETERS IN RESONANT CONVERTER AND DRIVER

Circuit Component	Nominal Value	Part Number
$L_{r1}$	0.68 $\mu\text{H}$	Coilcraft PFL1609-681
$L_{r2}$	0.68 $\mu\text{H}$	Coilcraft PFL1609-681
$C_{r1}, C_{r2}$	4.7 nF	MLCC Array, 50V
$C_o$	22 $\mu\text{F}$	X7R Ceramic, 10V
$Q_{r1}, Q_{r2}$		AOC2411 (P-channel)
$D_r$		CDBER0130L
$L_s$	4.7 $\mu\text{H}$	Coilcraft PFL1609-472
$L_g$	4.7 $\mu\text{H}$	Coilcraft PFL1609-472

$C_s$	3.3 nF	COG Ceramic, 10V
$C_{bias}$	10 nF	COG Ceramic, 10V
$R_{f1}$	100 k $\Omega$	Standard SMD
$R_{f2}$	22 k $\Omega$	Standard SMD
$R_{f3}$	10 $\Omega$	Standard SMD
$R_{b1}, R_{b2}$	100 $\Omega$	Standard SMD
$T_1, T_2$		EMZ1T2RCT-ND (NPN/PNP)
$D_1, D_2$		DSF01S30SC

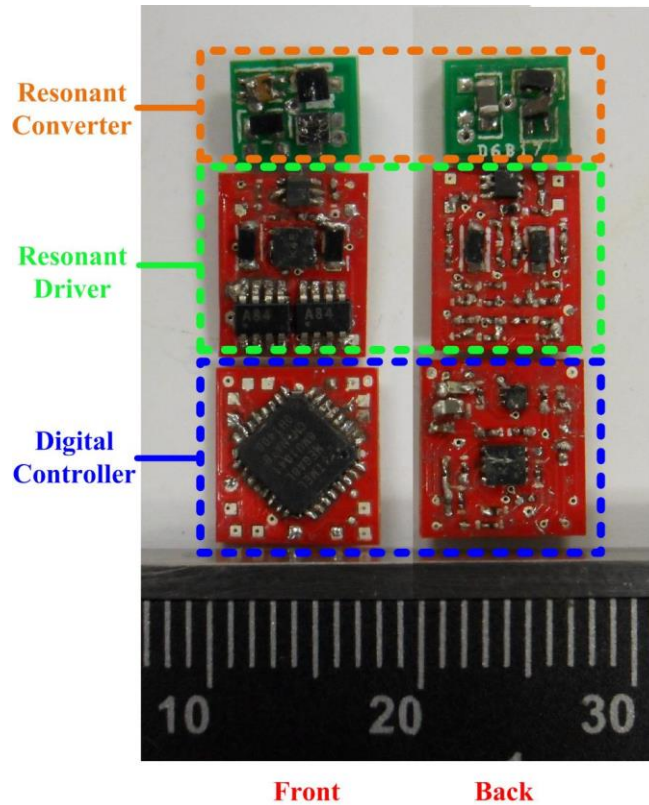


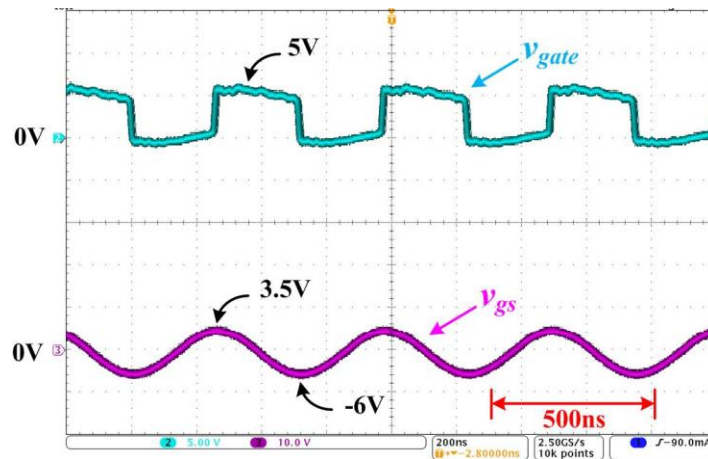
Figure 2.13. Front ( $L_{r1}$ ,  $C_{r1}$ ,  $C_{r2}$ ,  $Q_{r1}$  and  $Q_{r2}$ ) and back ( $L_{r2}$ ,  $D_r$  and  $C_o$ ) views of 100-mg, 2-MHz experimental prototype of the proposed Type 1 resonant ac-dc converter, as well as its resonant driver and digital controller.

In the majority of tiny electromagnetic (EMA) or electroactive polymer (EAP) generators, low output impedance and low self-inductance is acquired [3], [11]. Therefore, a discrete inductor  $L_{r1}$  is required in the converter. The PEI design in this section is specified for EMA generators; however, the converters are adaptable for EAP generators with alternating output voltages.

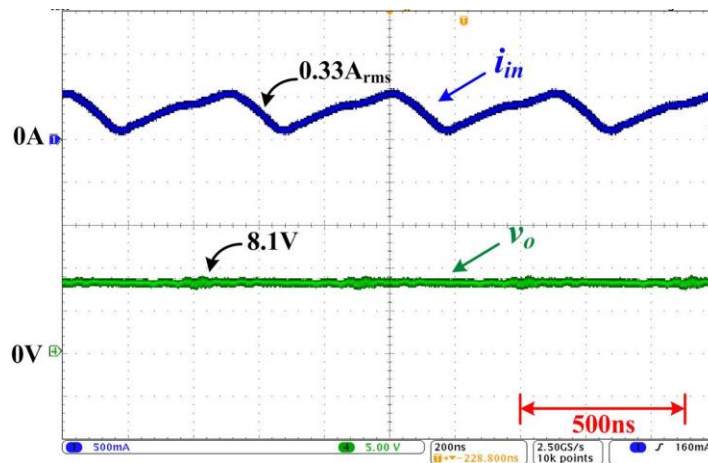
An 8-mg chip inductor (Coilcraft PFL1609-681), with 680 nH at 0.9 A<sub>sat</sub>, is selected as the resonant inductor  $L_{r1}$  (or the self-inductance  $L_m$  of an EMA generator) due to its low dc resistance, small footprint and good EMI performance. The ferrite shield of the inductor keeps the magnetic field within the package, thereby reducing the EMI noises. The same inductor is chosen as  $L_{r2}$ . A 4.7-nF/50-V ceramic capacitor array (MLCC Array) is used as resonant capacitors  $C_{r1}$  and  $C_{r2}$  while a 22- $\mu$ F/10-V ceramic capacitor is selected as the output capacitor  $C_o$ .

The transistors and diode are selected based on the stress analyses in Chapter 2.2.2. The p-channel enhancement mode MOSFET (AOC2411) with ball-grid-array (BGA) surface-mount package is selected due to its fast transient response and compactness. The transistor has capability of handling -30-V drain-to-source breakdown voltage and 3.4-A continuous current. Its 52-m $\Omega$  excellent on-resistance (tested at -4.5-V  $V_{gs}$ ), owing to the advanced trench technology, brings benefits in low conduction losses. The low gate charge and low gate voltage (as low as -2.5 V) cause fast transient response and low driver power dissipation. A 2-mg schottky barrier diode (CDBER0130L) with 0503 package is selected as the rectifier diode  $D_r$  due to its low forward voltage and small footprint.

Type 1 converter waveforms during 2-MHz switching with +3-V dc input voltage are presented in Fig. 2.14 and Fig. 2.15. According to the experimental waveforms, the topology provides good ZVS and ZCS characteristics with resonant gate drive at 2-MHz switching frequency. Both transistor and diode achieve ZVS turn-on and ZVS turn-off. In addition, ZCS is achieved during transistor turn-on and diode turn-off. An 8.1-V maximum output voltage is acquired through a 100- $\Omega$  resistive load, with 66.3% open-loop dc-dc conversion efficiency. The voltage gain tested at different resistive load condition is illustrated in Fig. 2.16.

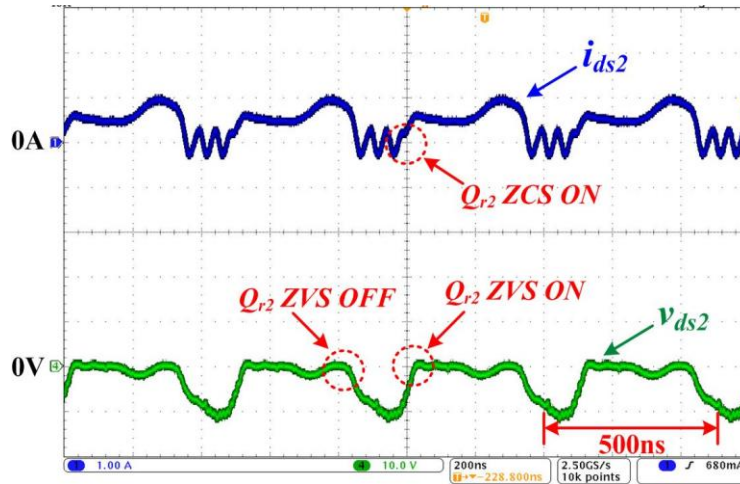


(a)

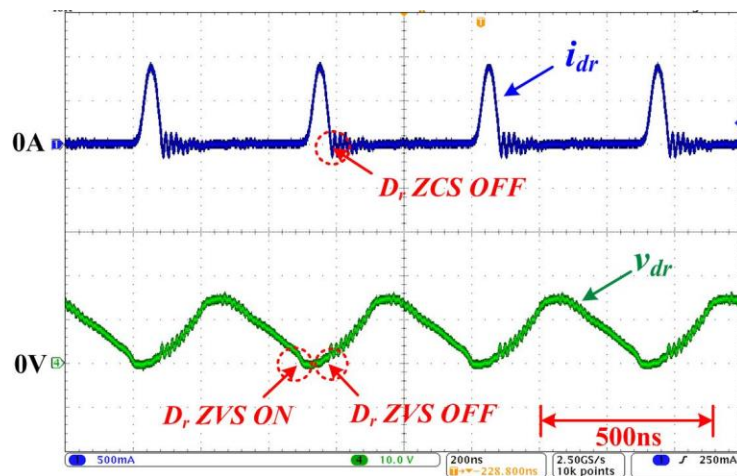


(b)

Figure 2.14. Experimental waveforms of Type 1 converter operating with  $V_{in}=3$  V (dc),  $V_o=8.1$  V (dc),  $R_{load}=100$   $\Omega$ , during 2-MHz switching: (a)  $v_{gate}$  and  $v_{gs}$ ; (b)  $i_{in}$  and  $V_o$ .



(a)



(b)

Figure 2.15. Experimental waveforms illustrating resonant switching of Type 1 converter, during 2-MHz switching: (a)  $i_{ds2}$  and  $v_{ds2}$ ; (b)  $i_{dr}$  and  $v_{dr}$ .

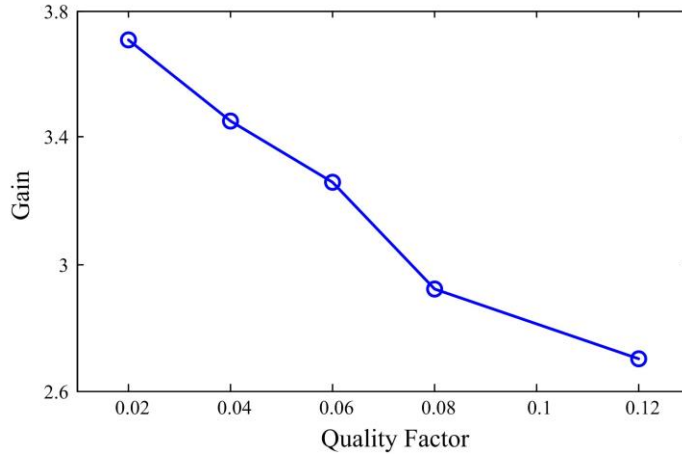
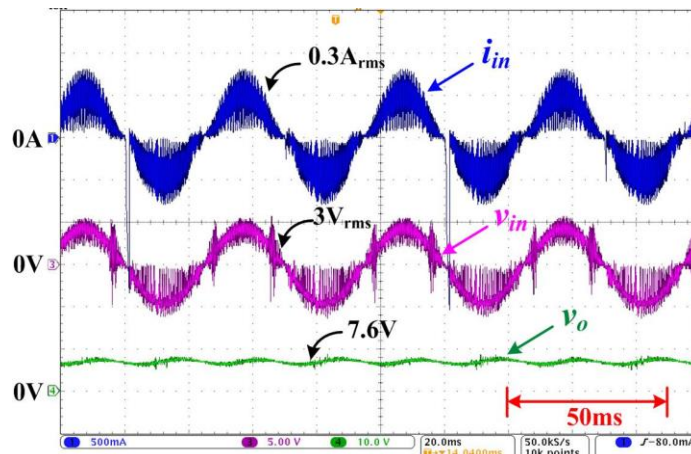
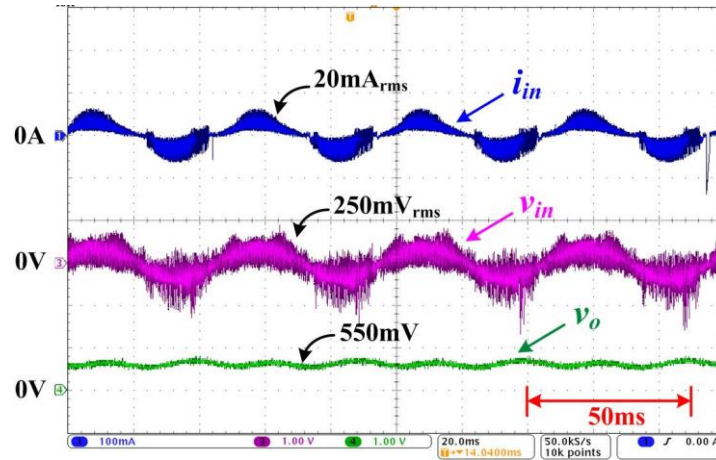


Figure 2.16. Voltage gain of Type 1 converter at +3V<sub>dc</sub> input under different load conditions.

A power amplifier circuit in conjunction with  $L_{rl}$  is utilized to emulate the EMA generator. The open-loop converter waveforms at a 20-Hz alternating input voltage with high-order harmonic distortion is presented in Fig. 2.17. The polarity identification module is adopted in the open-loop testing to achieve ac-dc conversion. The 20-Hz frequency corresponding to low mechanical vibration frequency of an EMA generator is selected to investigate the case of ambient energy harvesting. The converter shows good performance on rectification of a wide range of alternating input voltage. The ac-dc conversion efficiency is above 60% under very-low input voltages.

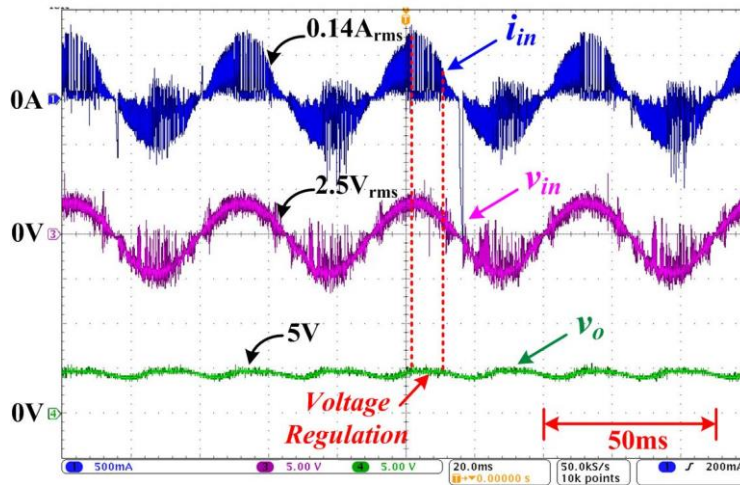


(a)

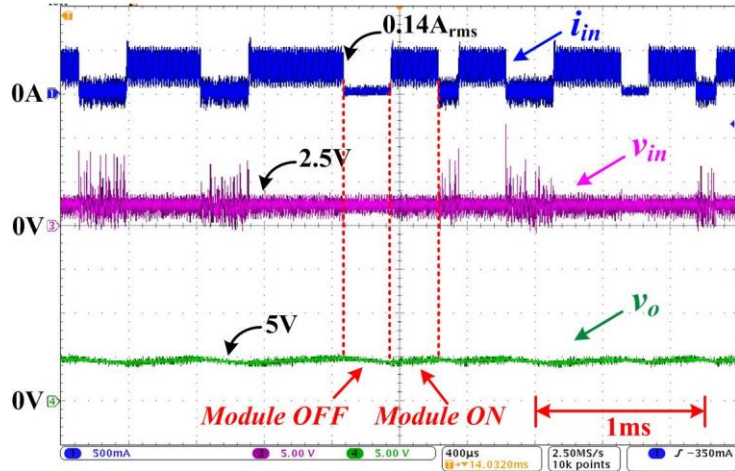


(b)

Figure 2.17. Open-loop experimental waveforms of Type 1 converter operating with (a)  $V_{in}=3\text{ V}_{\text{rms}}$  (20 Hz, ac),  $V_o=7.6\text{ V}$  (dc),  $R_{load}=100\ \Omega$ ; (b)  $V_{in}=0.25\text{ V}_{\text{rms}}$  (20 Hz, ac),  $V_o=0.55\text{ V}$  (dc),  $R_{load}=100\ \Omega$ , during 2-MHz switching:  $i_{in}$ ,  $v_{in}$  and  $V_o$ .



(a)



(b)

Figure 2.18. Closed-loop experimental waveforms of Type 1 converter operating with (a) voltage regulation for  $V_o=5$  V,  $R_{load}=100$   $\Omega$ ; (b) module on/off control at 20-kHz modulation frequency.

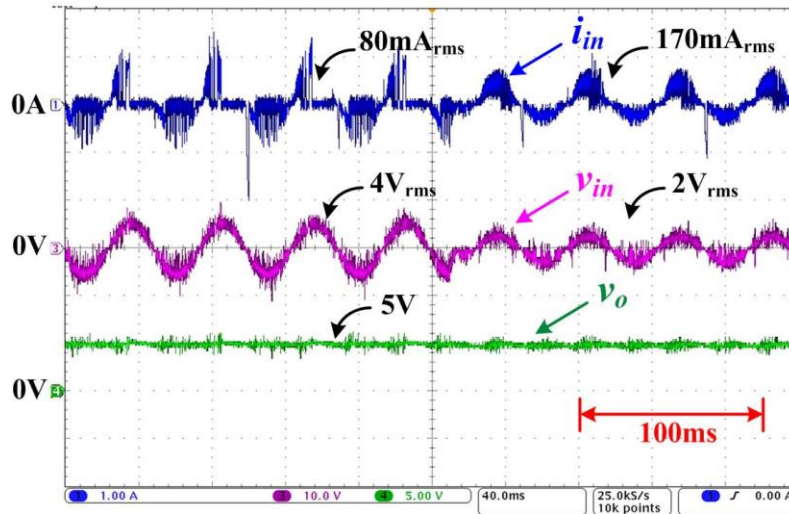


Figure 2.19. Closed-loop dynamic response of Type 1 converter operating with voltage regulation for  $V_o=5$  V,  $R_{load}=100$   $\Omega$ .

The closed-loop experimental waveforms with output voltage regulation are illustrated in Fig. 2.18. The output voltage is regulated at 5 V through the module on/off

control strategy. When  $V_o$  exceeds 5 V, the gate driver pulls the transistor gate to ground and thereby the module is disabled. When  $V_o$  is below 5 V, the gate driver returns to the resonant gating condition and the converter starts to transfer energy. Therefore, the input current and power are discontinuous with the module on/off control. The module PWM on/off frequency is set to 20 kHz. The closed-loop voltage regulation indicates a fast dynamic response with an instantaneous step change of input voltage (see Fig. 2.19).

#### **2.4.2 Efficiency Analyses**

Fig. 2.20 shows the open-loop efficiency (including power stage and gate driver) and the output power at different input voltages. The output power is nearly proportional to the square of the input voltage, which thereby matches the steady-state analyses. The conversion efficiency at very-low input voltages is above 60% and increases as the input voltage increases. In the case of very-low alternating input voltages, the converter has a large dead zone where the input voltage is close to zero, and the fundamental resonant component (much higher than the input voltage) is smaller than the forward voltage of the rectifier diode. The rectification of the converter fails at dead zone even though the converter is enabled, which in turn degrades the efficiency. On the other hand, the efficiency decreases after the output power exceeds certain value. The conduction losses and inductor core losses increase and become dominant as the current increases. Furthermore, the light-load efficiency is higher than the full-load efficiency at high input voltages, due to the dominant conduction losses and inductor core losses; however, they are close at low input voltages.

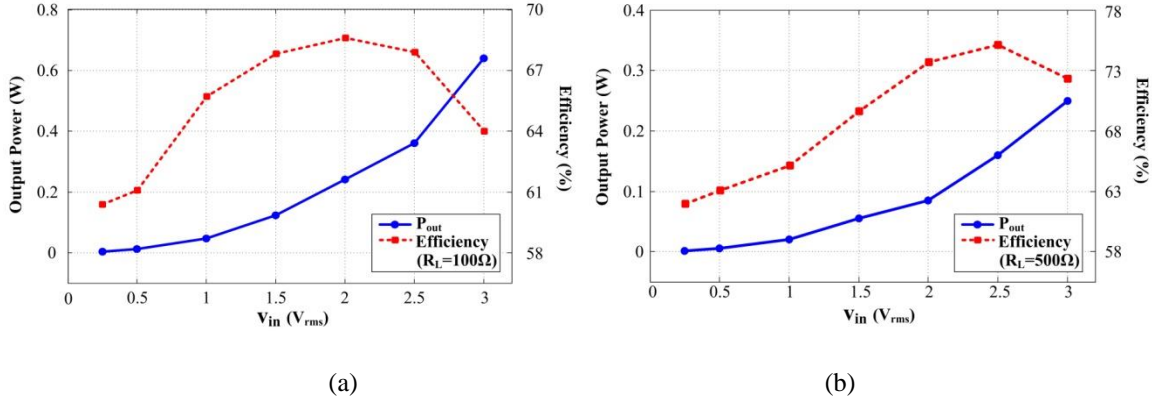


Figure 2.20. Open-loop output power and efficiency over input voltage of Type 1 converter at (a)  $R_{load}=100 \Omega$ ; and (b)  $R_{load}=500 \Omega$ .

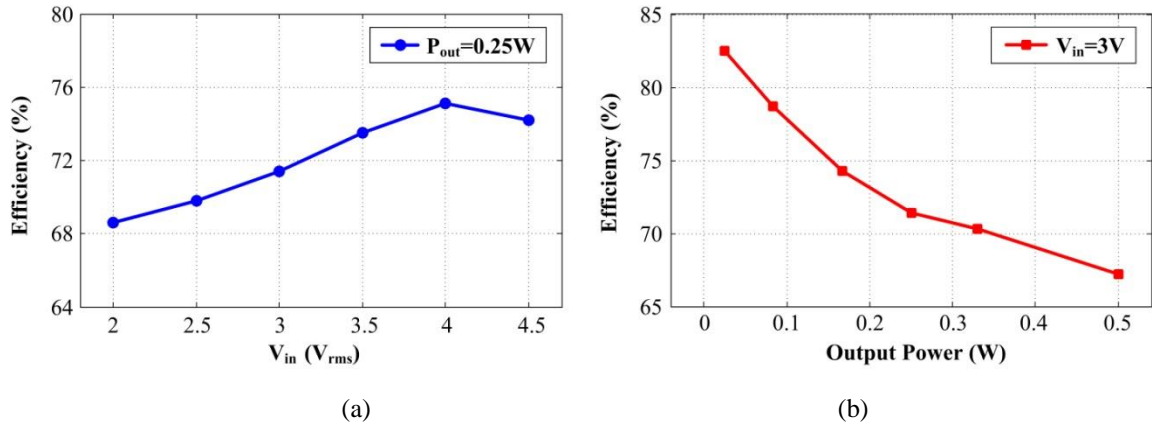


Figure 2.21. Closed-loop efficiency over (a) input voltage (at  $P_{out}=0.25$  W); and (b) output power (at  $V_{in}=3$  V<sub>rms</sub>).

The closed-loop efficiencies at various input voltages (at  $P_{out}=0.25$  W) and output powers (at  $V_{in}=3$  V<sub>rms</sub>) are illustrated in Fig. 2.21. At a constant output power, the average current decreases as the input voltage increases when the converter is enabled. When the converter is disabled, it consumes no power. Therefore, the conduction losses and inductor core losses decrease, which consequently causes higher efficiency in comparison to open loop at the same output power. At a constant input voltage, higher efficiency is

acquired at lower output power. The average current decreases as output power decreases, which leads to lower conduction losses and inductor core losses.

The conduction losses ( $P_{con}$ ), including transistor turn-on conduction losses ( $P_Q$ ), inductor copper losses ( $P_{Lr}$ ) and diode forward power losses ( $P_{dr}$ ), are represented as

$$P_{con} = P_Q + P_{Lr} + P_{dr} = 2 \cdot R_{Q,on} \cdot [I_{Q,rms}]^2 + R_{Lr2} \cdot I_{Lr2,rms}^2 + V_{dr, fw} \cdot I_{dr, avg} \quad (2-53)$$

where,  $R_{Q,on}$  is the drain-to-source on-state resistance of two transistors,  $I_{Q,rms}$  is root-mean-square (RMS) value of the transistor current,  $R_{Lr2}$  is the coil resistance of the resonant inductor  $L_{r2}$ ,  $I_{Lr,rms}$  is RMS value of the resonant inductor current,  $V_{dr, fw}$  is the forward voltage drop of the output diode, and  $I_{dr, avg}$  is the average value of the diode current. The total loss of the converter is 97 mW at 250 mW output power. Table 1.2 summarizes the loss breakdown associated with each component. Power stage loss is 74 mW (76.3% of total loss) and controller loss is 23 mW (23.7% of total loss).

TABLE 1.2

POWER LOSS ESTIMATION OF PEI		
COMPONENT	POWER LOSS	LOSS BREAKDOWN
<b>Power Stage</b>	<b>74 mW</b>	<b>76.3%</b>
Transistor ( $P_{Q1}, P_{Q2}$ )	6 mW	6.2%
Diode ( $P_{dr}$ )	18 mW	18.6%
Inductor ( $P_{Lr2}$ )	40 mW	41.2%
PCB	10 mW	10.3%
<b>Controller</b>	<b>23 mW</b>	<b>23.7%</b>
Microcontroller	5 mW	5.2%
Others	18 mW	18.5%

The efficiency analyses reveal the fact that the conduction losses and inductor core losses dominate over other losses such as switching losses and gating losses.

Moreover, the case becomes worse with a smaller size of converter where the conduction resistance is higher and the inductor core is smaller. Despite of this, the topology shows promising performance while minimizing the tradeoff between switching losses and miniaturization.

## 2.5 Summary

This chapter has outlined two novel bridgeless resonant ac-dc step-up converters suitable for high-frequency operation and low-voltage low-power ac-dc power conversion. These single-stage topologies provide direct ac-dc power conversion with much less number of components, in comparison to other resonant topologies. Both types of converters utilize soft-switched LC networks to convert low-frequency low-amplitude alternating input voltages into a high-frequency high-amplitude alternating voltage. The high-frequency alternating signal is then rectified into a dc output voltage through a soft-switched diode. Size miniaturization and high light-load efficiency are achieved through high-frequency soft-switching, resonant gating and a simple control scheme.

The performance of the circuit is verified through a 100-mg, 2-MHz prototype, which converts 3- $V_{\text{rms}}$  alternating input voltage into 7.6-V dc output voltage at 650-mW maximum output power. The circuit is designed to acquire high performance and miniature size. In addition to the size miniaturization, the circuit efficiently addresses the low-amplitude voltage rectification with fast transient response. The topology achieves higher than 70% closed-loop efficiency across wide range of input voltages and load conditions. As this chapter has elaborated, the topological concept can be adapted into other higher voltage and higher power applications.

## CHAPTER 3

### MINIATURIZED PEI DESIGN FOR MULTI-CHANNEL KINETIC ENERGY

#### HARVESTING SYSTEMS

Based on the resonant topological concept proposed in Chapter 2, this chapter outlines a novel design of multi-input resonant ac-dc topology for multi-channel electromagnetic energy harvesting systems.

#### **3.1 Electrical Model of Electromagnetic-reed Generators**

Wind energy is considered as one of the most promising alternative sources. Flapping electromagnetic-reed (EMR) generators, suitable to energize standalone small-size and low-power electrical loads, such as light poles and wireless sensors, can harvest energy from wind-induced vibration [3]. The EMR generators, such as wind energy harvesting cell, are suitable for virtually any wind conditions including turbulent wind found in many real-world settings [142]-[144].

In comparison to electroactive polymer (EAP) generators, EMR generators outperform in terms of high output current, high efficiency and high power density [3], [14]-[16]. The illustrative scheme and electrical model of a permanent magnet linear generator are depicted in Fig. 3.1, where  $k$  is the spring stiffness constant;  $m$  is the proof-mass;  $D_p$  represents the parasitic damper;  $K_E$  denotes the generated voltage coefficient; and  $z$  is the relative movement. The detailed analyses and modeling of the EMR generators are presented in [3], [16]. Typically, the extrinsic vibrations introduce internal spinning or linear oscillation between the electrical damper (an armature with coil winding) and the proof-mass (a stator with permanent magnets). The internal movement

results in a periodically variable magnetic flux in the coil winding, which in turn induces a corresponding alternating electromotive force (EMF) [18].

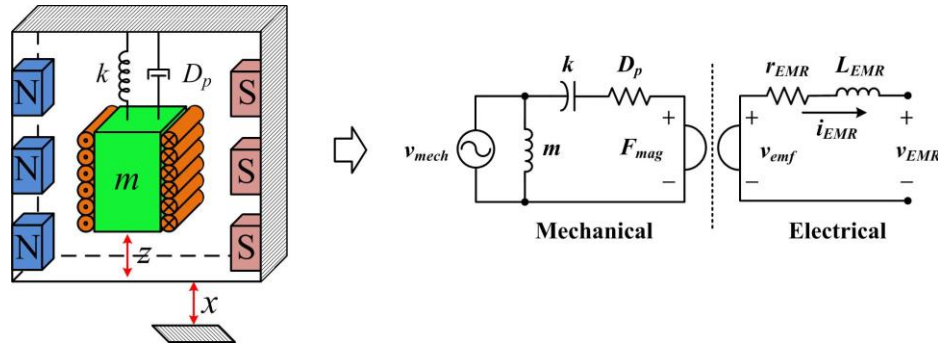


Figure 3.1. Equivalent circuit of one EMR generator ( $v_{mech}$ : mechanical velocity;  $m$ : proof mass;  $k$ : spring stiffness;  $D_p$ : mechanical damping;  $F_{mag}$ : magnetic force;  $v_{emf}$ : EMF;  $r_{EMR}$ : coil resistance;  $L_{EMR}$ : self-inductance;  $i_{EMR}$ : generator terminal current;  $v_{EMR}$ : generator terminal voltage).

The electrical model of an EMR generator can be represented as an induced EMF  $v_{emf}$  in series with a self-inductance  $L_{EMR}$  and an internal resistor  $r_{EMR}$  of the electrical damper (see Fig. 3.1). In comparison to typical electromagnetic generators, EMR generators may have high output impedance due to high number of winding with high-permeability core. With purpose of circuit integration, the input inductance of the converter can be replaced by  $L_{EMR}$  of the EMR generator. Therefore, the self-inductance of the damper can be used as part of the inductance on the circuit design and operation. In such cases, the circuit design and operation will be different from those in Chapter 2.

Most of these EMR generators share the same characteristics as electrical generators. However, their output voltage and power are erratic and low, which brings challenges in efficient PEI design. The PEIs are required to process the small and irregular voltage/power from EMR generators and then feed the load with a constant

voltage/power. The miniaturization of PEI is an important aspect of the design to increase the power density due to the limited space in majority of the systems. The proposed resonant ac-dc converters are intended to convert and step up the alternating low voltage into a dc voltage in the case of low-voltage energy harvesting. The switching frequency of the converter is required to be significantly higher than the vibrating frequency of generators.

### **3.2 Multi-channel Energy Harvesting Systems**

In a multi-channel energy harvesting system, PEI are required to condition the output power of multiple energy harvesters and effectively deliver power to the loads [54], [56], [76], as shown in Fig. 3.2(a). Power density and efficiency at low power conversion are important performance metrics of power converters for low-speed wind energy harvesting. One of the main challenges toward fabricating efficient converters for multi-channel systems is the efficient conditioning of multiple and independent low-amplitude voltages of generators. Due to the mutual interference of different channels, a large number of components and controllers are required that may increase size, losses and complexity of PEI. Therefore, an integrated multi-input power electronic converter is necessary as power stage of miniature PEI, as shown in Fig. 3.2(b).

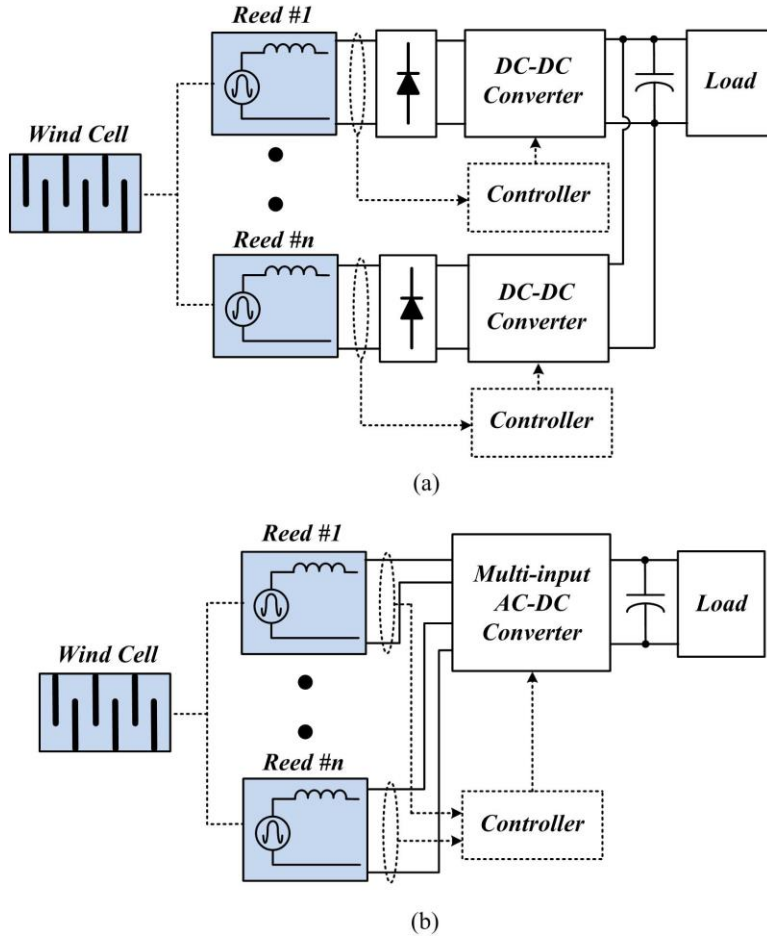


Figure 3.2. Multiple EMR generators and PEI system: (a) conventional PEI; and (b) proposed multi-input PEI.

Conventionally, the multi-channel EMR generators are interfaced with diode bridges for rectification [54]. Due to the rectification, the equivalent open-circuit voltage ( $|v_{emf}|$ ) is equal to the absolute value of electromotive force (EMF), as shown in Fig. 3.3(a). First, since the load is connected in series with the generator, the load root-mean-square (rms) voltage is lower than RMS value of generator EMF. However, in most of cases, a load voltage higher than EMF is required (i.e. for battery charging). As a result, a switching power converter capable of stepping up the EMF is necessary. Secondly, in order to extract the maximum power from a source, the equivalent input impedance ( $Z_{in}$ )

of the circuit should be set equal to the optimal impedance ( $Z_{opt}$ ) for impedance matching [17]. However, with a wide range of load ( $R_L$ ), it is difficult and impractical to adjust the input impedance to the optimal value by using a diode bridge. A switching power converter should be used to adjust the impedance ( $Z_r$ ) and regulate the input impedance ( $Z_{in}$ ) for optimal impedance matching, as illustrated in Fig. 3.3(b).

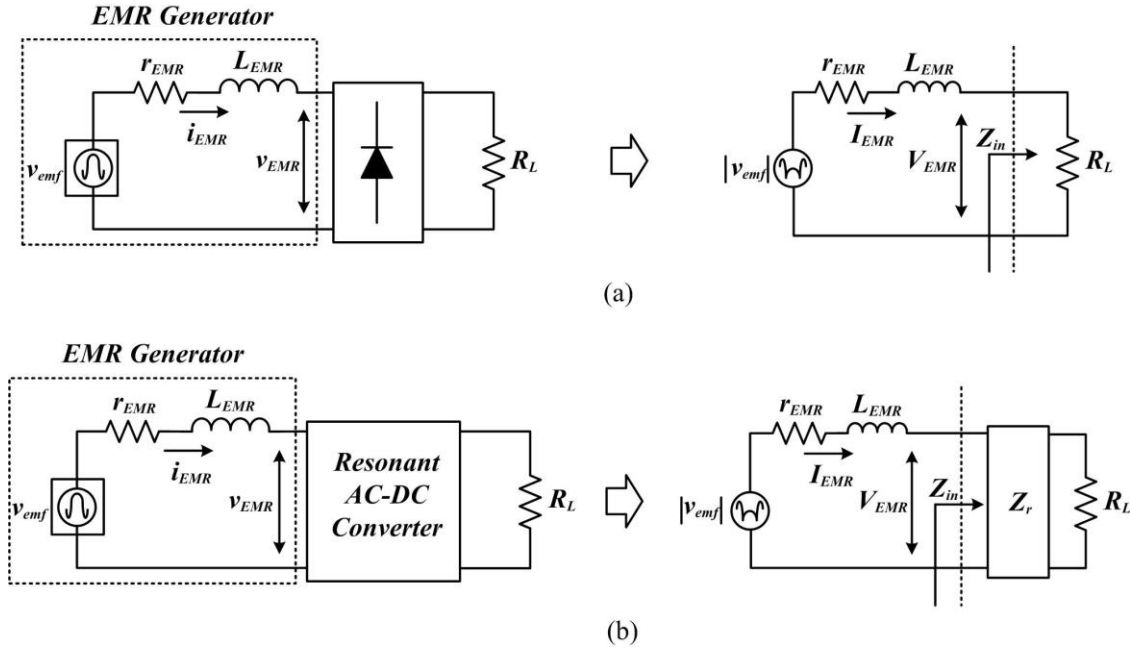


Figure 3.3. Impedance network of an EMR generator interfaced with (a) a diode bridge; and (b) a single-input resonant ac-dc converter ( $Z_r$ : characteristic impedance;  $R_{load}$ : load resistance;  $Z_{in}$ : equivalent input impedance).

### 3.3 Design of Multi-channel Energy Harvesting Power Stage

#### 3.3.1 Multi-input Bridgeless Resonant AC-DC Converter

Fig. 3.4 illustrates the proposed multi-input single-stage bridgeless resonant ac-dc converter. The topology is capable of operating with multiple inductive sources, in this case EMR generator. Each inductive source, which can be a low-frequency alternating

source with high-order harmonic distortion, is numbered with  $i=1,2,\dots,N$ . The multi-input circuit is formed by one resonant inductor, one diode and multiple MOSFET-capacitor bridges. Each input source is connected to two MOSFET-capacitor bridges ( $Q_{r1}^{(i)}, C_{r1}^{(i)}$  and  $Q_{r2}^{(i)}, C_{r2}^{(i)}$ ), which share a resonant inductor and a diode.

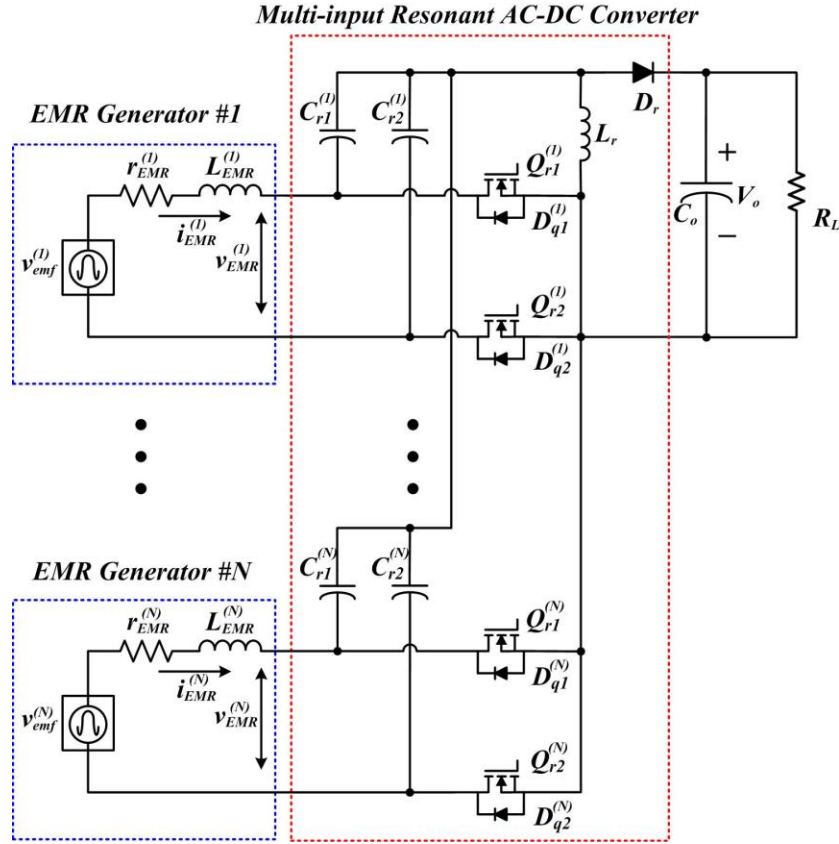


Figure 3.4. Illustrative scheme of the proposed multi-input converter ( $v_{emf}^{(i)}$ : EMF of #i channel;  $r_{EMR}^{(i)}$ : coil resistance;  $L_{EMR}^{(i)}$ : self-inductance;  $i_{EMR}^{(i)}$ : channel terminal current;  $v_{EMR}^{(i)}$ : channel terminal voltage;  $C_{r1}^{(i)} = C_{r2}^{(i)}$ : resonant capacitors;  $L_r$ : resonant inductor;  $Q_{r1}^{(i)}, Q_{r2}^{(i)}$ : MOSFETs;  $D_r$ : output diode;  $C_o$ : output capacitor).

The resonant inductor ( $L_r$ ) is tuned with resonant capacitors ( $C_{r1}^{(i)}$  and  $C_{r2}^{(i)}$ ) to resonate at the resonant frequency ( $f_r$ ) near the switching frequency ( $f_s$ ). Ideally, the resonant components ( $L_r, C_{r1}^{(i)}$  and  $C_{r2}^{(i)}$ ) present a lossless low drain-to-source

impedance branch across MOSFETs near  $f_s$ . The LC network amplifies the EMF.  $C_{r1}^{(i)}$  and  $C_{r2}^{(i)}$  are in parallel with MOSFETs and the diode to ensure ZVS at turning-on and turning-off. Switching losses are eliminated through the oscillating voltage and current, while the input energy is stored and released to the load through the active LC network. Furthermore, the tuned networks eliminate overvoltage spikes as well as diode reverse recovery issues while simultaneously maintaining low peak voltage stresses on MOSFETs.

MOSFETs ( $Q_{r1}^{(i)}$  and  $Q_{r2}^{(i)}$ ) are actively turned on and off with duty cycle close to 0.5 in order to generate drain-to-source pulse voltage ( $v_{ds1}^{(i)}$  and  $v_{ds2}^{(i)}$ ) at the input of LC network. The amplitude of drain-to-source pulse voltage is higher than  $v_{emf}$  due to the energy stored in  $L_{EMR}^{(i)}$ . The fundamental component of  $v_{ds1}^{(i)}$  and  $v_{ds2}^{(i)}$  pass through the LC network and generate an amplified oscillating voltage near  $f_s$  across the rectifier diode  $D_r$ . ZVS and ZCS operation of  $Q_{r1}^{(i)}$  and  $Q_{r2}^{(i)}$  provide energy recovery to drain-to-source MOSFET parasitic capacitor ( $C_{ds}$ ), which in turn increases the efficiency. The drain-to-source overvoltage spike is eliminated; thereby no snubber circuit is required. The output diode ( $D_r$ ) rectifies the amplified oscillating voltage after the tuned network into a dc output voltage. It generates freewheeling path for the resonant inductor current as well as charging path for the resonant capacitors.

### 3.3.2 Principle of Operation

In a switching cycle, one EMR generator can be assumed as a current source if the generator has a large self-inductance. In this case, for simplicity of analysis, each EMR generator is assumed as a current source ( $I_{in}^{(i)}$ ) during a switching period. In a mechanical vibration cycle,  $I_{in}^{(i)}$  is positive at positive sub-cycle and is negative at negative sub-cycle.

There are three switching sub-intervals (*Stage I ~ Stage III*) during one switching cycle at either positive sub-cycle or negative sub-cycle. For simplicity, the switching sub-intervals of a dual-input topology with a positive input and a negative input, as illustrated in Fig. 3.5, are presented in steady state. The analyses can be analogously extended to the multi-input topology. For a positive input ( $I_{in}^{(1)}$ ),  $Q_{r2}^{(1)}$  is conducting in the entire positive sub-cycle while  $Q_{r1}^{(1)}$  is switching; for a negative input ( $I_{in}^{(2)}$ ),  $Q_{r1}^{(2)}$  is conducting in the entire negative sub-cycle while  $Q_{r2}^{(2)}$  is switching. Therefore, the rectification of each alternating source is achieved by conducting  $Q_{r2}^{(i)}$  while switching  $Q_{r1}^{(i)}$  at positive sub-cycle; or conducting  $Q_{r1}^{(i)}$  while switching  $Q_{r2}^{(i)}$  at negative sub-cycle.

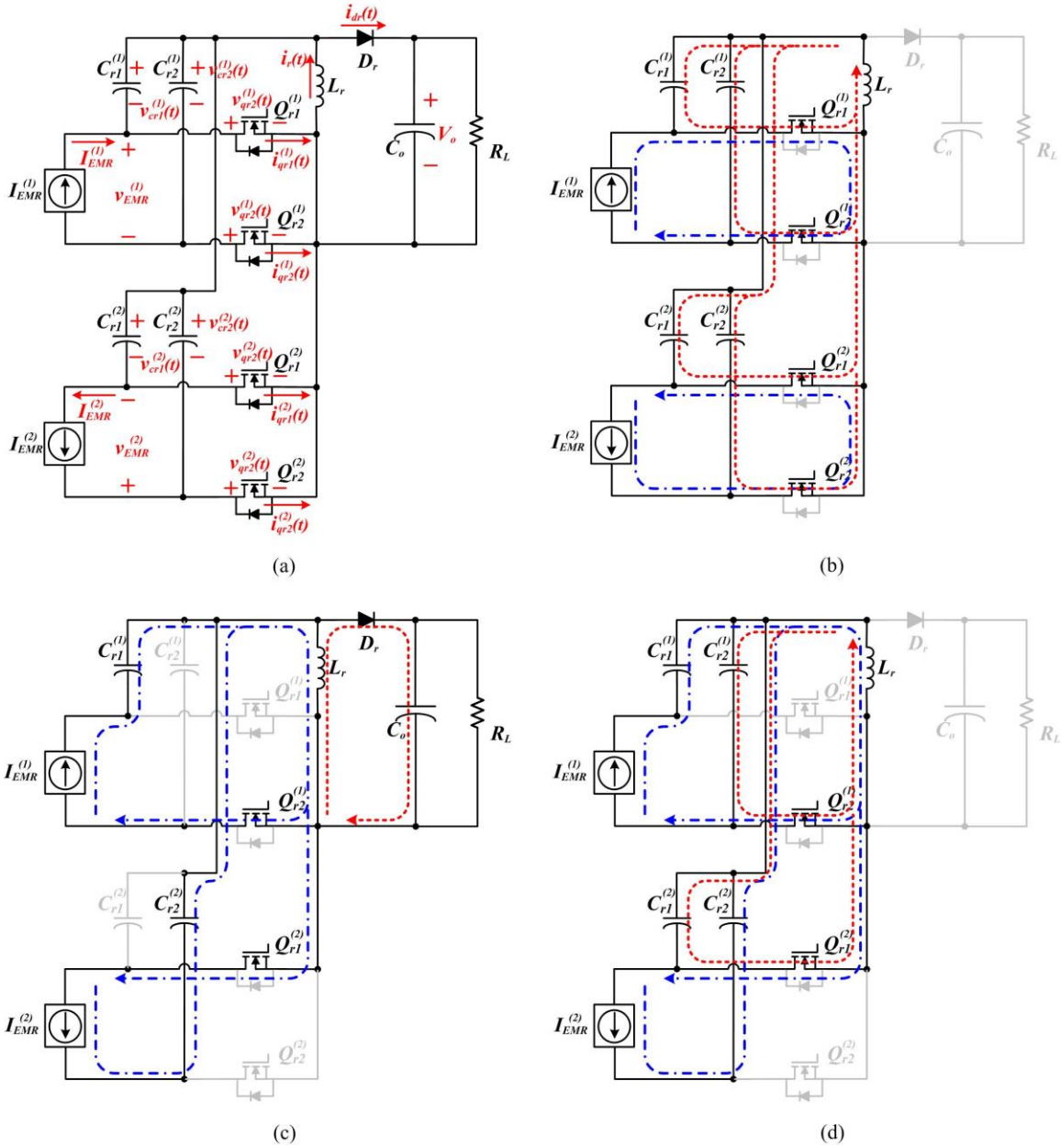


Figure 3.5. (a) Simplified topology of dual-input resonant converter with a positive input and a negative input; (b)~(d) switching sub-intervals during a switching cycle.

The simulation waveforms of a dual-channel system during one switching cycle are demonstrated in Fig. 3.6. The switching frequency is close to the resonant frequency ( $f_r$ ) of  $L_r C_{r1} C_{r2}$  network, and the switching duty cycle is close to 0.5. Relative to the

resonant capacitors,  $C_o$  has very small impedance at  $f_s$ , thereby it acts as a voltage source and can be considered as a constant value,  $V_o$ . The capacitances  $C_{r1}^{(i)}$  and  $C_{r2}^{(i)}$  ( $i=1,2$ ) are set equal to  $C_r$  for the impedance matching.

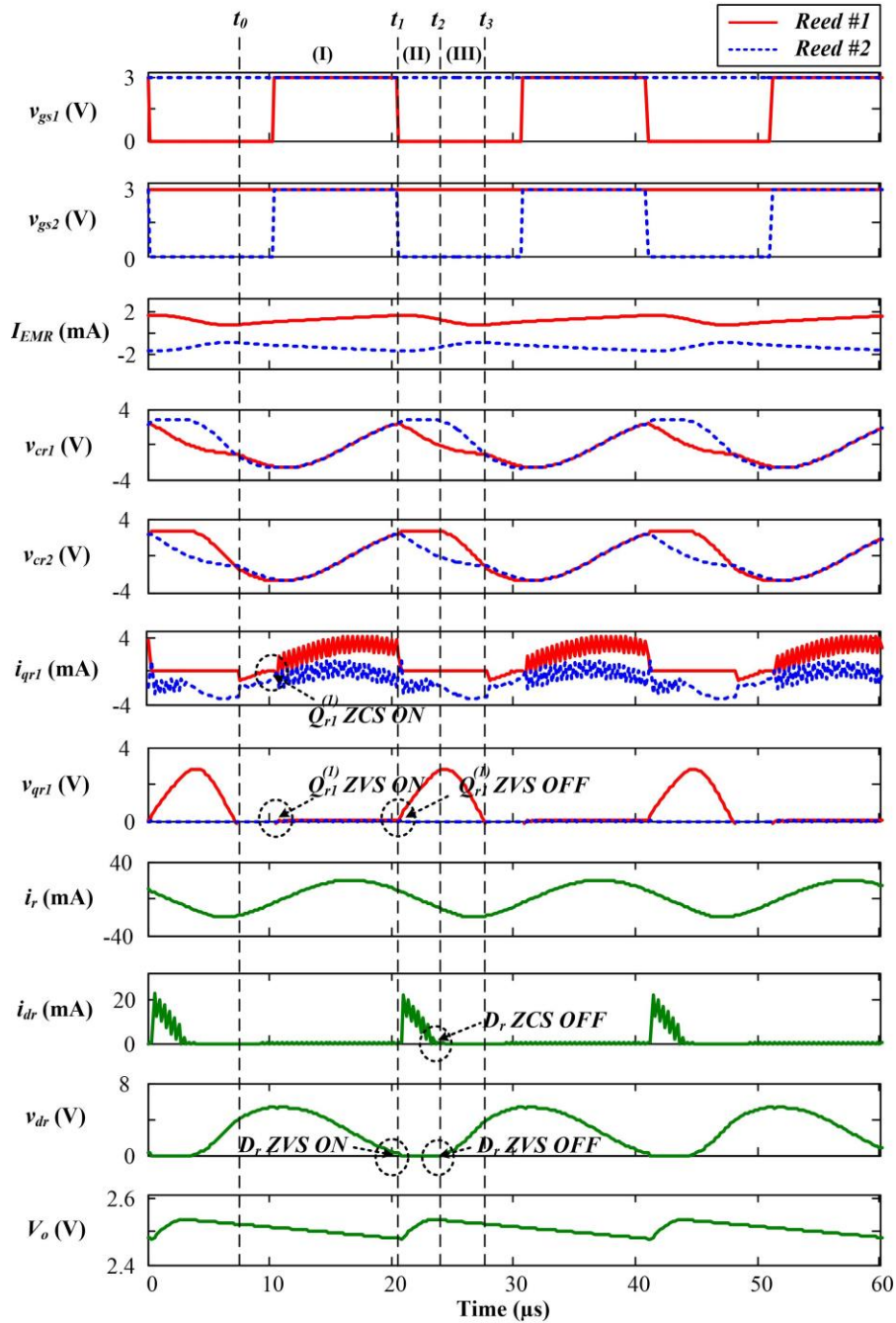


Figure 3.6. Simulation waveforms of dual-channel system during a switching cycle.

At  $t_0$ : (Circuit initial state) It is assumed that  $I_{EMR}^{(1)}$  and  $I_{EMR}^{(2)}$  have initial values.  $v_{cr1}^{(1)}$ ,  $v_{cr2}^{(1)}$ ,  $v_{cr1}^{(2)}$  and  $v_{cr2}^{(2)}$  have the same negative initial values,  $v_{cr1}(t_0)$ .  $Q_{r1}^{(1)}$  and  $Q_{r2}^{(2)}$  are both off before  $t_0$ .

*Stage I ( $t_0 \sim t_1$ ):* At  $t_0$ , as shown in Fig. 3.5(b), body diodes of  $Q_{r1}^{(1)}$  and  $Q_{r2}^{(2)}$  are turned on at zero voltage [ $v_{qr1}^{(1)}(t_0)$  and  $v_{qr2}^{(2)}(t_0)$ ] (equal to  $v_{cr2}^{(1)} - v_{cr1}^{(1)}$ ). As soon as the currents through body diodes reduce to zero,  $Q_{r1}^{(1)}$  and  $Q_{r2}^{(2)}$  are turned on at zero voltage [ $v_{qr1}^{(1)}(t_0)$  and  $v_{qr2}^{(2)}(t_0)$ ] (equal to  $v_{cr2}^{(1)} - v_{cr1}^{(1)}$ ) and zero current [ $i_{qr1}^{(1)}(t_0)$  and  $i_{qr2}^{(2)}(t_0)$ ]. The self-inductances of generators start to get charged by the input EMFs, thereby  $I_{EMR}^{(1)}$  and  $I_{EMR}^{(2)}$  increase linearly.  $C_{r1}^{(1)}$ ,  $C_{r2}^{(1)}$ ,  $C_{r1}^{(2)}$  and  $C_{r2}^{(2)}$  begin to resonate with  $L_r$  at  $f_r$ .  $v_{cr1}^{(1)}$ ,  $v_{cr2}^{(1)}$ ,  $v_{cr1}^{(2)}$  and  $v_{cr2}^{(2)}$  are equal and increase sinusoidally until they are equal to  $V_o$  at  $t_1$ . The governing equations in terms of  $v_{cr1}^{(i)}$ ,  $v_{cr2}^{(i)}$  and  $i_r$  are:

$$\begin{cases} \frac{di_r(t)}{dt} = \frac{v_{cr1}^{(i)}(t)}{L_r} = \frac{v_{cr2}^{(i)}(t)}{L_r} & (3-1) \\ \frac{dv_{cr1}^{(i)}(t)}{dt} = \frac{dv_{cr2}^{(i)}(t)}{dt} = -\frac{i_r(t)}{2NC_r} & (3-2) \end{cases}$$

where,  $N=2$  is the number of input sources. Hence, the transient state of  $i_r$  and  $v_{cr1}^{(i)}$  can be expressed as:

$$\begin{cases} i_r(t) = i_r(t_0) \cos \omega_r(t-t_0) + \frac{v_{cr1}^{(i)}(t_0)}{Z_r} \sin \omega_r(t-t_0) & (3-3) \end{cases}$$

$$\begin{cases} v_{cr1}^{(i)}(t) = v_{cr2}^{(i)}(t) = v_{cr1}^{(i)}(t_0) \cos \omega_r(t-t_0) - i_r(t_0) Z_r \sin \omega_r(t-t_0) & (3-4) \end{cases}$$

where,  $\omega_r = (2NL_r C_r)^{-1/2}$  is the angular resonance frequency of LC network; and  $Z_r = (L_r / 2NC_r)^{1/2}$  is the characteristic impedance of LC network. Assuming  $i_r(t_0)$  is very small, the first component of  $i_r(t)$  and the second component of  $v_{cr1}^{(i)}(t)$  can be neglected.

*Stage II ( $t_1 \sim t_2$ ):* At  $t_1$ ,  $Q_{r1}^{(1)}$  and  $Q_{r2}^{(2)}$  are turned off at zero voltage [ $v_{qr1}^{(1)}(t_1)$  and  $v_{qr2}^{(2)}(t_1)$ ], as depicted in Fig. 3.5(c). The energy stored in the generator self-inductance

begins to be transferred to  $L_r$ .  $D_r$  turns on at zero voltage [ $v_{dr}(t_1)$ ], allowing the current (equal to  $I_{EMR}^{(1)} + I_{EMR}^{(2)} + i_r$ ) to freewheel through  $D_r$ .  $i_r$  decreases linearly due to  $V_o$  across  $L_r$ . In this interval,  $v_{cr1}^{(1)}$  and  $v_{cr2}^{(2)}$  decrease; however,  $v_{cr2}^{(1)}$  and  $v_{cr1}^{(2)}$  remain equal to  $V_o$ . The governing equations are:

$$\left\{ \begin{array}{l} \frac{di_r(t)}{dt} = \frac{V_o}{L_r} \end{array} \right. \quad (3-5)$$

$$\left\{ \begin{array}{l} \frac{dv_{cr1}^{(1)}(t)}{dt} = -\frac{I_{EMR}^{(1)}}{C_r} \end{array} \right. \quad (3-6)$$

$$\left\{ \begin{array}{l} \frac{dv_{cr2}^{(2)}(t)}{dt} = -\frac{I_{EMR}^{(2)}}{C_r} \end{array} \right. \quad (3-7)$$

$v_{cr1}^{(1)}$  and  $v_{cr2}^{(2)}$  decrease linearly from their boundary condition  $v_{cr1}^{(1)}(t_1) = v_{cr2}^{(2)}(t_1) = V_o$ , yielding

$$\left\{ \begin{array}{l} i_r(t) = \frac{V_o}{L_r}(t-t_1) + i_r(t_1) \end{array} \right. \quad (3-8)$$

$$\left\{ \begin{array}{l} v_{cr1}^{(1)}(t) = -\frac{I_{EMR}^{(1)}}{C_r}(t-t_1) + V_o \end{array} \right. \quad (3-9)$$

$$\left\{ \begin{array}{l} v_{cr2}^{(2)}(t) = -\frac{I_{EMR}^{(2)}}{C_r}(t-t_1) + V_o \end{array} \right. \quad (3-10)$$

$$\left\{ \begin{array}{l} v_{cr2}^{(1)}(t) = v_{cr1}^{(2)}(t) = V_o \end{array} \right. \quad (3-11)$$

*Stage III* ( $t_2 \sim t_3$ ): At  $t_2$ ,  $i_{dr}$  drops to zero, leaving no current to freewheel through  $D_r$ .  $D_r$  turns off at both zero voltage [ $v_{dr}(t_2)$ ] and zero current [ $i_{dr}(t_2)$ ] at  $t_2$ .  $C_{r2}^{(1)}$ ,  $C_{r1}^{(2)}$ , and  $L_r$  begin to resonate, until  $v_{cr2}^{(1)}$  and  $v_{cr1}^{(2)}$  are respectively equal to  $v_{cr1}^{(1)}$  and  $v_{cr2}^{(2)}$  at  $t_3$ . The governing equations of Stage III can be represented as

$$\left\{ \begin{array}{l} \frac{di_r(t)}{dt} = \frac{v_{cr2}^{(1)}(t)}{L_r} = \frac{v_{cr1}^{(2)}(t)}{L_r} \end{array} \right. \quad (3-12)$$

$$\left\{ \begin{array}{l} \frac{dv_{cr2}^{(1)}(t)}{dt} = \frac{dv_{cr1}^{(2)}(t)}{dt} = \frac{\sum_{i=1}^N I_{EMR}^{(i)} - i_r(t)}{NC_r} \end{array} \right. \quad (3-13)$$

The governing equations of  $v_{cr1}^{(1)}$  and  $v_{cr2}^{(2)}$  are similar to those in Stage II. By applying boundary conditions  $v_{cr2}^{(1)}(t_2)=v_{cr1}^{(2)}(t_2)=V_o$  and  $i_r(t_2)=-I_{EMR}^{(1)}-I_{EMR}^{(2)}$ ,  $i_r$ ,  $v_{cr2}^{(1)}$  and  $v_{cr1}^{(2)}$  can be presented as

$$\begin{cases} i_r(t) = \sum_{i=1}^N I_{EMR}^{(i)} \cos \sqrt{2}\omega_r(t-t_2) + \frac{V_o}{\sqrt{2}Z_r} \sin \sqrt{2}\omega_r(t-t_2) + \sum_{i=1}^N I_{EMR}^{(i)} & (3-14) \end{cases}$$

$$\begin{cases} v_{cr2}^{(1)}(t) = v_{cr1}^{(2)}(t) = V_o \cos \sqrt{2}\omega_r(t-t_2) - \sum_{i=1}^N I_{EMR}^{(i)} \sqrt{2}Z_r \sin \sqrt{2}\omega_r(t-t_2) & (3-15) \end{cases}$$

At  $t_3$ : the body diodes of  $Q_{r1}^{(1)}$  and  $Q_{r2}^{(2)}$  turn on, both at zero voltage, and  $v_{cr1}^{(1)}$  and  $v_{cr2}^{(1)}$  become equal. Consequently, the circuit returns to the original state.

Since the integral of the current through  $C_o$  over one switching period at steady state equals to zero;  $\int i_{dr}(t)dt = V_o/R_L f_s$ . Using the boundary condition  $i_r(t_1) = i_{dr,peak}/2$  the following equation can be obtained as,

$$i_r(t_1) = V_o \sqrt{\frac{1}{2L_r R_L f_s}} \quad (3-16)$$

On the other hand, the integral of the current through  $C_{r1}^{(1)}$  over one switching period at steady state equals to zero;  $v_{cr1}^{(1)}(t_0)=v_{cr1}^{(1)}(t_3)$ . Using the boundary condition  $v_{cr1}^{(1)}(t_1)=V_o$  the following equation can be obtained from Eq. (3-3), Eq. (3-4), Eq. (3-9) and Eq. (3-16).

$$V_o [1 - \sqrt{\frac{\omega_r Z_r}{2R_L f_s}} \sin \omega_r(t_1-t_0) - \cos \omega_r(t_1-t_0)] = \frac{t_3-t_1}{NC_r} \sum_{i=1}^N I_{EMR}^{(i)} \quad (3-17)$$

By setting the transistor turn-on time  $t_{on}=t_1-t_0=3T_r/4=3\pi/2\omega_r$  and  $R_L \gg Z_r$ ,  $V_o$  can be represented in terms of the sum of  $I_{EMR}^{(i)}$  as,

$$V_o = \frac{t_{off}}{NC_r} \sum_{i=1}^N I_{EMR}^{(i)} \quad (3-18)$$

where,  $t_{off}=t_3-t_1=T_s-t_{on}$  is the turn-off time interval. By introducing the ratio of angular resonance frequency to switching frequency ( $\gamma=f_r/f_s$ ) and the coefficient  $\alpha=4\gamma-3$ , Eq. (3-18) can be written as

$$V_o = \alpha\pi Z_r \sum_{i=1}^N I_{EMR}^{(i)} \quad (3-19)$$

The switching frequency ( $f_s$ ) is slightly higher than the resonance frequency ( $f_r$ ). When  $R_L \gg Z_r$ , the converter can be considered as a current-controlled voltage-source. The impedance network of an  $N$ -channel system during one switching period is shown in Fig. 3.7.  $V_o$  is determined by the sum of the channel currents ( $I_{EMR}^{(i)}$ ), through setting the network impedance ( $Z_r$ ) to a desired value. At the same  $Z_r$  and load condition, connecting more EMR generators results in a higher output voltage. Furthermore, the output voltage regulation can be achieved through real-time pulse frequency modulation (PFM).

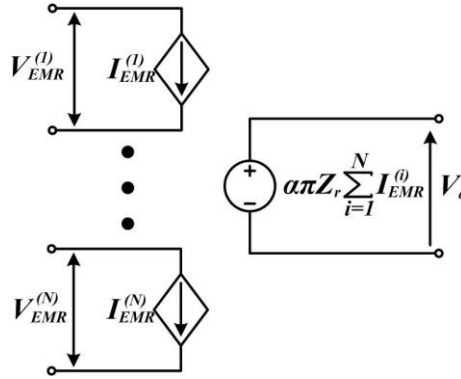


Figure 3.7. Switching average model of an  $N$ -channel system.

### 3.4 Optimal Impedance Matching

To extract the maximum power from an  $N$ -channel system, it is necessary to acquire the equivalent input impedance of an  $N$ -input converter depicted in Fig. 3.8(a). In the case of a resistive load ( $R_L$ ) comparable to  $Z_r$ , in one switching period, including  $R_L$  in  $V_o$  yields:

$$\frac{V_o}{\sum_{i=1}^N I_{EMR}^{(i)}} = \frac{\alpha\pi Z_r}{1 + \sqrt{\pi Q_r \gamma}} \quad (3-20)$$

where,  $Q_r=Z_r/R_L$  denotes the quality factor. According to Eq. (3-20) and  $V_o=I_oR_L$ , the output-to-input current ratio can be represented as

$$\frac{I_o}{\sum_{i=1}^N I_{EMR}^{(i)}} = \frac{\alpha\pi Q_r}{1 + \sqrt{\pi Q_r \gamma}} \quad (3-21)$$

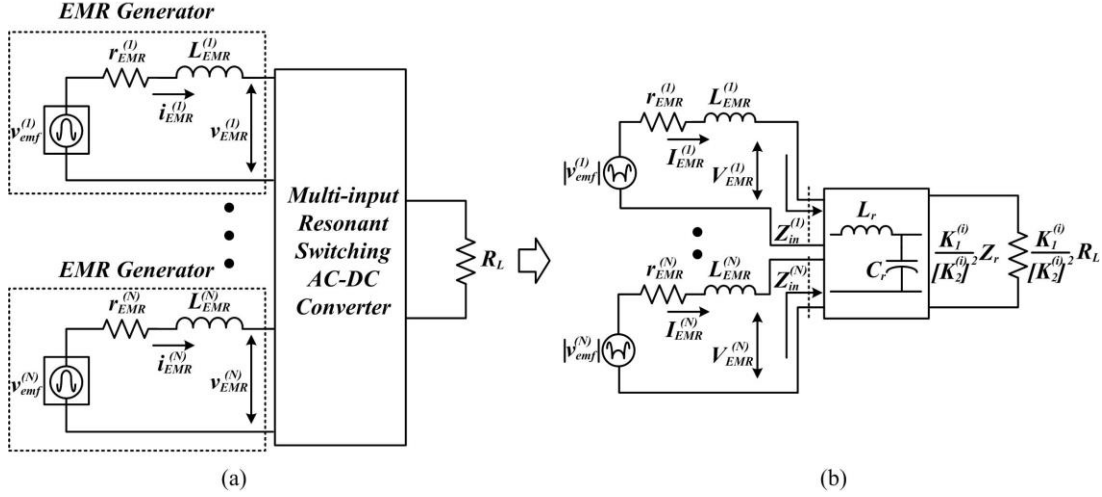


Figure 3.8. (a) An  $N$ -channel EMR generator system connected with an  $N$ -input resonant ac-dc converter; and (b) impedance network of an  $N$ -channel system.

In a vibration cycle, considering the conversion efficiency ( $\eta_{ff}$ ), the generated power ( $P_{EMR}^{(i)}$ ) from each channel and the output power ( $P_o$ ) of the converter should satisfy

$$P_{EMR}^{(i)} = V_{EMR}^{(i)} I_{EMR}^{(i)} = K_1^{(i)} \sum_{i=1}^N P_{EMR}^{(i)} \quad (3-22)$$

$$I_{EMR}^{(i)} = K_2^{(i)} \sum_{i=1}^N I_{EMR}^{(i)} \quad (3-23)$$

$$P_o = V_o I_o = \eta_{ff} \sum_{i=1}^N P_{EMR}^{(i)} \quad (3-24)$$

$$Z_{in}^{(i)} = \frac{V_{EMR}^{(i)}}{I_{EMR}^{(i)}} = \frac{P_{EMR}^{(i)}}{[I_{EMR}^{(i)}]^2} \quad (3-25)$$

where,  $V_{EMR}^{(i)}$  is the average terminal voltage of the  $i^{th}$  channel during one switching period,  $K_1^{(i)}$  is the percentage value of  $i^{th}$  channel's generated power over total power,  $K_2^{(i)}$  is the percentage value of  $i^{th}$  channel's terminal current over total current,  $Z_{in}^{(i)}$  is the equivalent input impedance of the  $i^{th}$  input connected to the  $i^{th}$  channel. In a switching period,  $K_1^{(i)}$  and  $K_2^{(i)}$  can be assumed constant due to the assumption that the channel current ( $I_{EMR}^{(i)}$ ) and the channel power ( $P_{EMR}^{(i)}$ ) are constant. However,  $K_1^{(i)}$  and  $K_2^{(i)}$  are variable in a vibration cycle, since the generator current and the generator power oscillate at vibration frequency.

Based on Eq. (3-25), the equivalent input impedance connected to the  $i^{th}$  channel can be expressed as

$$Z_{in}^{(i)} = \frac{K_1^{(i)}}{[K_2^{(i)}]^2} \frac{R_L}{\eta_{ff} (1/\alpha\pi Q_r + 1)^2} = \frac{K_1^{(i)}}{[K_2^{(i)}]^2} Z_{in} \quad (3-26)$$

where,  $Z_{in}$  is the equivalent input impedance of the  $i^{th}$  input connected to the  $i^{th}$  channel while other channels are disconnected.  $Z_{in}^{(i)}$  is constant during a switching period; however, it changes in a vibration cycle due to the variable coefficients  $K_1^{(i)}$  and  $K_2^{(i)}$ . The impedance network of an  $N$ -channel system during one vibration cycle is illustrated in Fig. 3.8(b). The characteristic impedance of the converter and load impedance are different for each channel, and they change during a vibration cycle. The total input power of the circuit is given by

$$\sum_{i=1}^N P_{EMR}^{(i)} = \sum_{i=1}^N [I_{EMR}^{(i)}]^2 Z_{in}^{(i)} = Z_{in} \sum_{j=1}^N K_1^{(j)} \left[ \sum_{i=1}^N I_{EMR}^{(i)} \right]^2 = Z_{in} \left[ \sum_{i=1}^N I_{EMR}^{(i)} \right]^2 \quad (3-27)$$

According to the general model of EMR generators, the maximum power of the  $i^{th}$  channel connected to the  $i^{th}$  input can be extracted when the input impedance of the  $i^{th}$  input equals to the optimal input impedance ( $Z_{in}^{(i)} = Z_{opt}$ ). However, for an  $N$ -channel

system connected to an  $N$ -input converter, the maximum power of the  $N$ -channel system is extracted as

$$P_{EMR,max} = Z_{in} \left[ \sum_{i=1}^N I_{EMR}^{(i)} \right]^2 \Bigg|_{Z_{in}=Z_{opt}^*} \quad (3-28)$$

where,  $Z_{opt}^* \leq Z_{opt}$ . Eq. (3-28) reveals the fact that the total maximum power of an  $N$ -channel system is extracted through achieving optimal impedance matching of the  $N$ -input converter ( $Z_{in}=Z_{opt}^*$ ) rather than optimal impedance matching of each input ( $Z_{in}^{(i)}=Z_{opt}$ ). The optimal impedance can be acquired by setting characteristic impedance ( $Z_r$ ) of LC network.

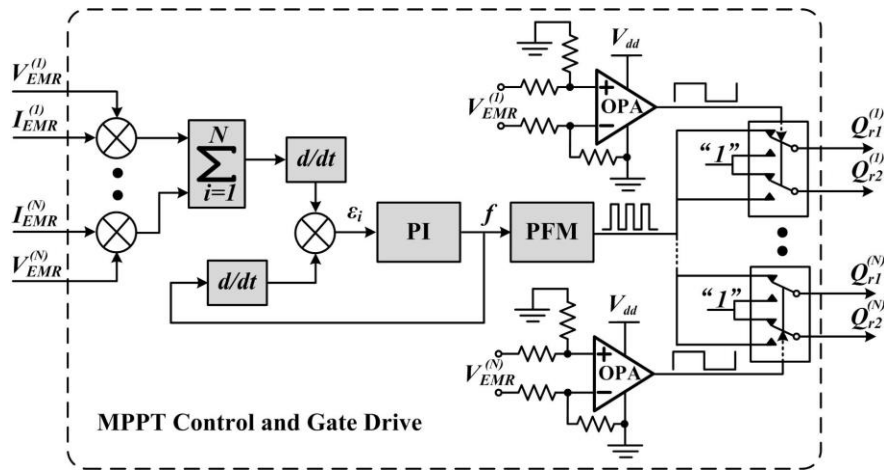


Figure 3.9. Illustrative scheme of the MPPT control strategy and gate drive.

In addition to the impedance matching through LC network design, the input impedance can be further regulated in real time by PFM. Increasing the switching frequency ( $f_s$ ) reduces the equivalent input impedance ( $Z_{in}$ ). A closed-loop PI control is used to acquire the optimal switching frequency ( $f_{opt}$ ) corresponding to  $Z_{opt}$ .  $f_s$  is increased when both derivations of the total input power and  $f_s$  have the same polarity; on the other

hand, it is decreased when the derivation polarities of the total input power and  $f_s$  are different. The maximum power point tracking (MPPT) control and gate drive system is demonstrated in Fig. 3.9. Zero-crossing comparators are used to generate pulse signals synchronous with the generator vibration. Demultiplexer switches are controlled by pulse signals to produce MOSFET gating signals. Fig. 3.10 illustrates the simulation of a six-input resonant converter with six individual EMR generators feeding a resistive load.

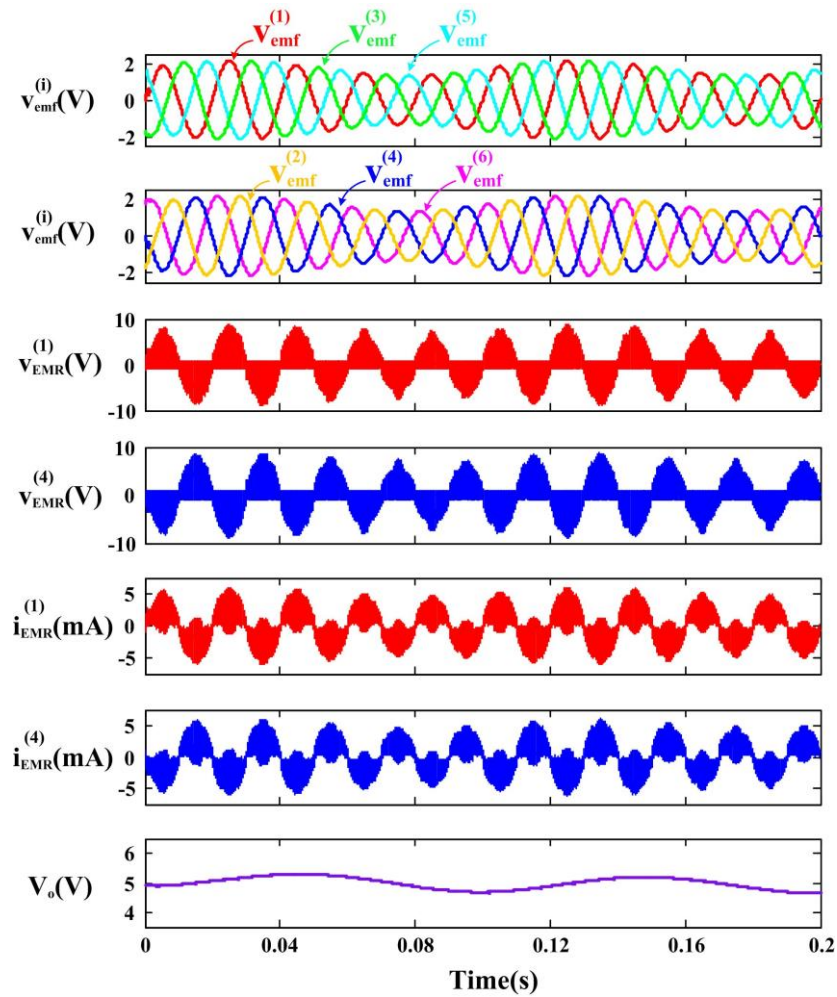


Figure 3.10. Simulation waveforms of a six-input converter connected to a resistive load.

### 3.5 Testing and Discussion

#### 3.5.1 Prototypes and Design Specification

A 5cm×3cm, six-input prototype of the proposed resonant converter, illustrated in Fig. 3.11, is fabricated for power conditioning of six EMR generators. Components and design parameters of the prototype PEI are listed in Table 3.1.

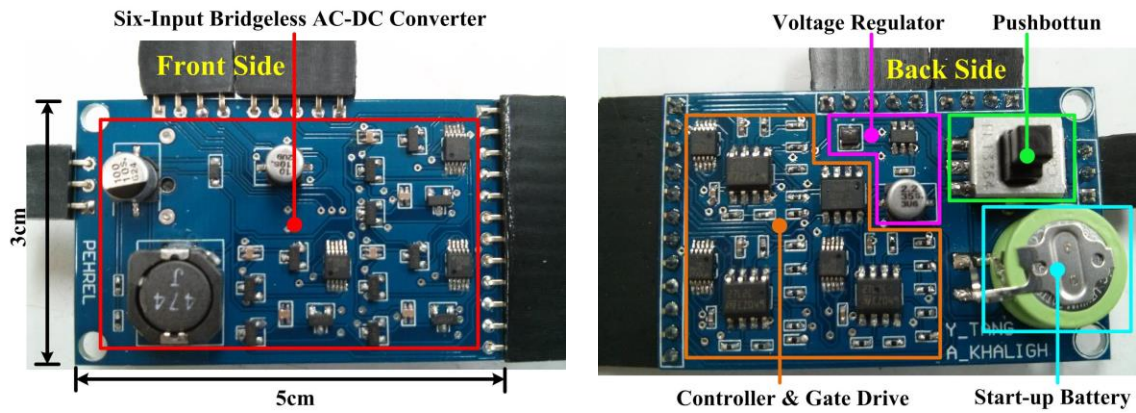


Figure 3.11. Six-input standalone prototype of the proposed resonant ac-dc converter for a six-EMR-generator system.

TABLE 3.1  
COMPONENT PARAMETERS OF EMR GENERATOR AND PEI

PARAMETER	DESCRIPTION	QUANTITY	PART NUMBER
<b>Power Converter</b>			
Resonant capacitor ( $C_{r1}^{(1)\sim(6)}$ , $C_{r2}^{(1)\sim(6)}$ )	2.2 nF, 50 V, Array	6	CKCM25X8R1H222 M060AK
Resonant inductor ( $L_r$ )	470 $\mu$ H, 0.62 A, 0.89 $\Omega$	1	MSS1048-474KL
Output dc capacitor ( $C_o$ )	100 $\mu$ F, 10 V	1	EEE-1AA101WR
Transistor ( $Q_{r1}^{(1)\sim(6)}$ , $Q_{r2}^{(1)\sim(6)}$ )	20 V, 1.9 A, 63 m $\Omega$	12	IRLML2030TRPBF
Diode ( $D_r$ )	20 V, 0.5 A, 0.3 V	1	DB2J20900L
<b>Control Board</b>			

Microcontroller	3V, 144 $\mu$ A, 2 PWM, 3 ADC	1	ATTINY13V-10SSU
OpAmp	0.04 V/ $\mu$ s, 3 V, 14 $\mu$ A	3	TS27L2CDT
Resistor	100 k $\Omega$	12	MCR01MRTJ104
Capacitor	1 nF, 10 V	6	C1005JB1H102K050

In order to achieve optimal impedance matching for a six-channel system, the characteristic impedance ( $Z_r$ ) is set equal to 133  $\Omega$ . For a more powerful source,  $Z_r$  and  $Z_{in}$  can be reduced through either reducing the resonant inductance or increasing resonant capacitance. Moreover, the natural frequency ( $f_r$ ) is set to 45 kHz with consideration of resonant losses and size miniaturization. Higher resonant frequency leads to smaller size of passive components; however, it results in higher resonant losses. The switching frequency ( $f_s$ ) is chosen to be 48 kHz, slightly higher than  $f_r$ . The resonant inductor and resonant capacitors are determined as

$$\left\{ \begin{array}{l} L_r = \frac{Z_r}{2\pi f_r} \\ C_r = \frac{1}{4\pi N f_r Z_r} \end{array} \right. \quad (3-29)$$

In order to reduce the resonant losses at low power, a 470- $\mu$ H inductor with ferrite powder core and low dc resistance is selected as the resonant inductor ( $L_r$ , much smaller than the self-inductance of the EMR generator). 2.2-nF/50-V ceramic capacitor arrays are used as resonant capacitors. The MOSFETs with high compactness, fast transient response and low on-resistance are selected to reduce conduction losses. These MOSFETs have low gate charge and low gate voltage (as low as 2 V). Hence, the circuit can operate with low supply voltage, and will have low gating power dissipation as well

as fast transient response. The rectifier diode ( $D_r$ ) is selected based on the low forward voltage and low on-resistance. Low-power components are selected in the control board to enhance the standalone capability. ATTINY13V is used as the controller due to its low profile package, low power consumption and minimum required functions. OpAmps and demultiplexer switches are adopted to detect the input polarity and provide gating signals.

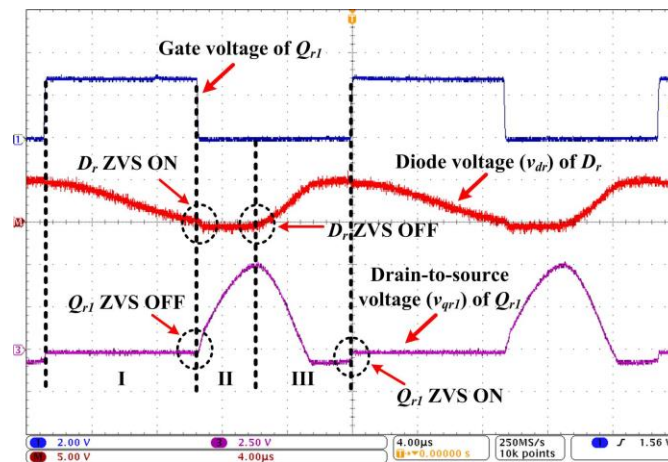
### **3.5.2 Energy Harvesting Testbed**

The prototype is tested with different sources to evaluate the operational performance at low power. The summary of circuit performance is listed in Table 3.2. A 1-V dc source corresponding to 1-V EMF of the EMR generator is first applied to demonstrate the circuit's switching operation. A 1.5-mH inductor corresponding to the self-inductance of the EMR generator is placed in conjunction with each input. The experimental waveforms at 48-kHz switching frequency are presented in Fig. 3.12 (a) and (b). High switching frequency can be achieved by tuning the network, illustrated in Fig. 3.12(c). According to the switching waveforms, the MOSFETs and the diode have ZVS turn-on and turn-off characteristics at the switching frequency close to the resonant frequency. A 2.4-V maximum output voltage is acquired through a 1-k $\Omega$  dc resistive load, with 94.4% dc-dc conversion efficiency.

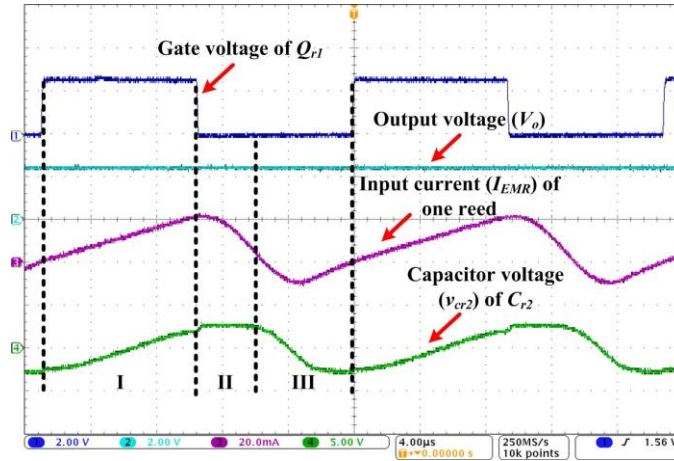
TABLE 3.2

ELECTRICAL PERFORMANCE OF PEI FOR MULTI-CHANNEL ENERGY HARVESTING

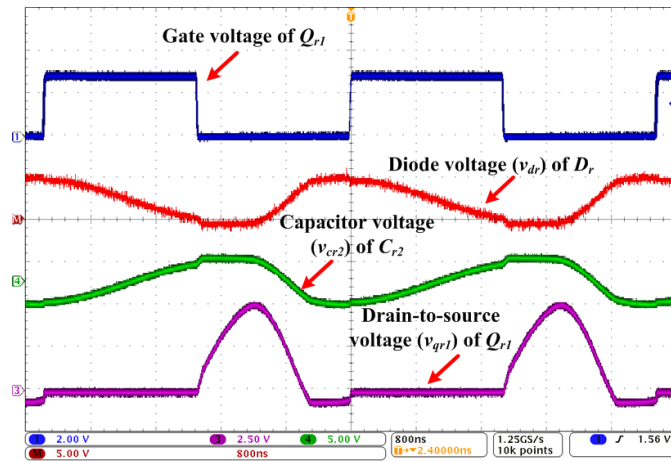
PARAMETER	NOMINAL VALUE
<b><i>Power Amplifier</i></b>	
Input frequency ( $f_{in}$ )	20~50 Hz
Open-circuit voltage ( $v_{emf}$ )	0.5~3 V (rms)
Terminal voltage ( $V_{EMR}$ )	2.5~7 V (peak)
Total input power ( $P_{EMR}$ )	1.8~34 mW
<b><i>EMR Generator</i></b>	
Input frequency ( $f_{in}$ )	15 Hz
Open-circuit voltage ( $v_{emf}$ )	0.5~2.5 V (rms)
Generator terminal voltage ( $V_{EMR}$ )	2.5~5 V (peak)
Total input power ( $P_{EMR}$ )	1~4.5 mW
<b><i>PEI</i></b>	
Switching frequency ( $f_s$ )	48 kHz
Resonant frequency	45 kHz
Characteristic impedance	133 $\Omega$
Output voltage	1.2~5.5 V
Output power	1.5~30 mW
Efficiency	85~91%



(a)



(b)

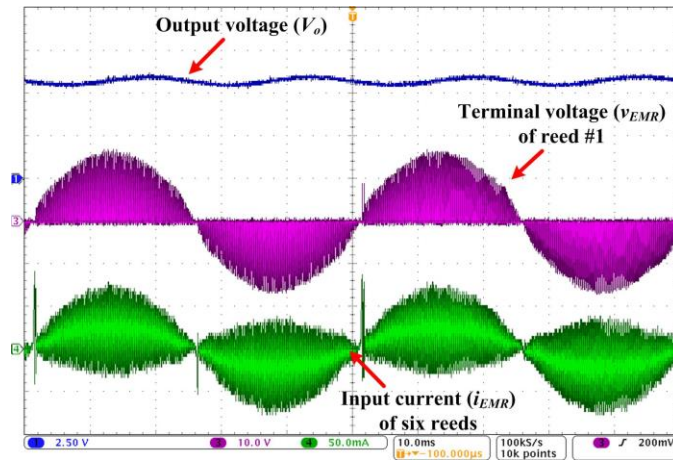


(c)

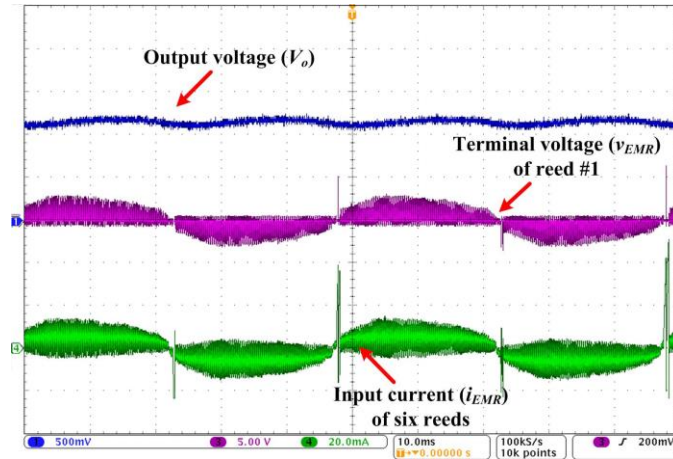
Figure 3.12. Experimental waveforms of switching operation:  $v_{emf} = 1 \text{ V}$ ,  $f_s = 48 \text{ kHz}$ ; X-axis:  $4 \mu\text{s}/\text{div}$ ; Y-axis: (a) Ch1 = gate voltage of  $Q_{r1}$ ,  $2 \text{ V}/\text{div}$ ; Ch3 = drain-to-source voltage ( $v_{qr1}$ ) of  $Q_{r1}$ ,  $2.5 \text{ V}/\text{div}$ ; ChM = diode voltage ( $v_{dr}$ ) of  $D_r$ ,  $5 \text{ V}/\text{div}$ ; and (b) Ch1 = gate voltage of  $Q_{r1}$ ,  $2 \text{ V}/\text{div}$ ; Ch2 = output voltage ( $V_o$ ),  $2 \text{ V}/\text{div}$ ; Ch3 = input current ( $I_{EMR}$ ) of one input,  $20 \text{ mA}/\text{div}$ ; Ch4 = inductor voltage ( $v_r$ ),  $5 \text{ V}/\text{div}$ ; and (c)  $f_s = 200 \text{ kHz}$ , Ch1 = gate voltage of  $Q_{r1}$ ,  $2 \text{ V}/\text{div}$ ; Ch3 = drain-to-source voltage ( $v_{qr1}$ ) of  $Q_{r1}$ ,  $2.5 \text{ V}/\text{div}$ ; Ch4 = inductor voltage ( $v_r$ ),  $5 \text{ V}/\text{div}$ ; ChM = diode voltage ( $v_{dr}$ ) of  $D_r$ ,  $5 \text{ V}/\text{div}$ .

A power amplifier circuit in conjunction with 1.5-mH inductors at each input is utilized to emulate the inductive ac sources. In this case, the overall input power is evenly

split between six channels. The rms voltage of the power amplifier is set at 0.5~3 V corresponding to the EMF voltage,  $v_{emf}$ , of EMR generators. 20~50-Hz ac frequency corresponding to low mechanical vibration frequency of EMR generator is selected to investigate the case of ambient energy harvesting. The measured output power varies from 1.5 mW to 30 mW at 20-Hz ac input power, as presented in Fig. 3.13(a) and Fig. 3.13(b), respectively. The converter shows good performance on rectification of a wide range of EMF voltages (from 0.5 V to 3 V). Furthermore, experimental waveforms with step change of input ac power and input ac frequency are illustrated in Fig. 3.14(a) and Fig. 3.14(b), respectively. The ac-dc conversion efficiency is above 80% even at very-low input voltage and power.

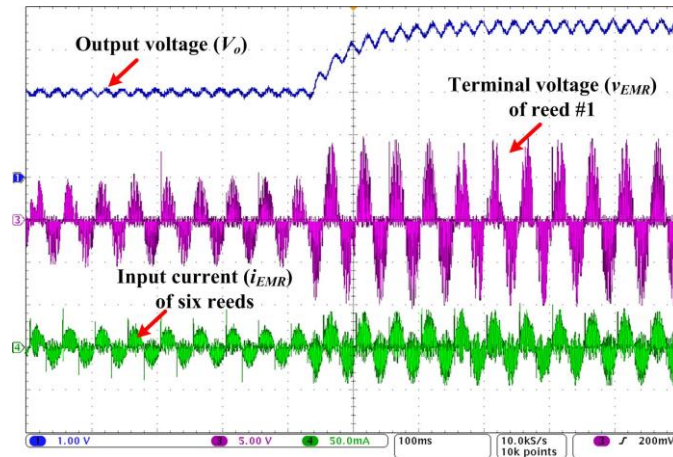


(a)

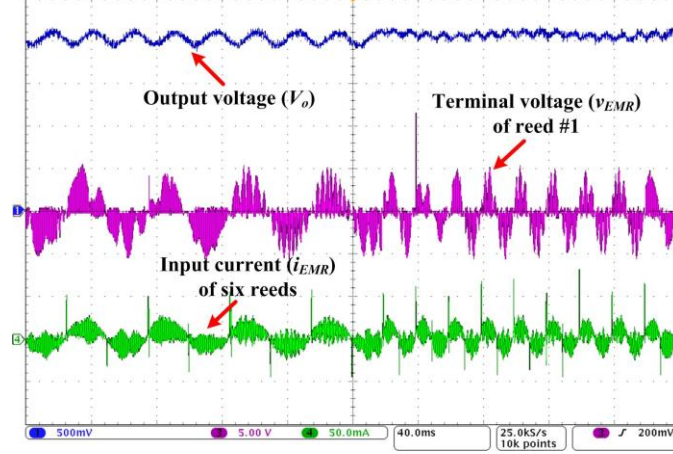


(b)

Figure 3.13. Experimental waveforms of power amplifiers:  $f_{in} = 20$  Hz; X-axis: 10 ms/div; Y-axis: (a)  $v_{emf} = 3$  V<sub>rms</sub>; Ch1 = output voltage ( $V_o$ ), 2.5 V/div; Ch2 = terminal voltage ( $v_{EMR}$ ) of channel #1, 10 V/div; Ch3 = input current ( $i_{EMR}$ ) of six channels, 50 mA/div; and (b)  $v_{emf} = 0.5$  V<sub>rms</sub>; Ch1 = output voltage ( $V_o$ ), 0.5 V/div; Ch2 = terminal voltage ( $v_{EMR}$ ) of channel #1, 5 V/div; Ch3 = sum of the input currents ( $i_{EMR}$ ) of six channels, 10 mA/div.



(a)



(b)

Figure 3.14. Experimental waveforms of power amplifiers with step change: X-axis: 40 ms/div; Y-axis: (a)  $v_{emf}$  = from 1  $V_{rms}$  to 2  $V_{rms}$ ; Ch1 = output voltage ( $V_o$ ), 1 V/div; Ch2 = terminal voltage ( $v_{EMR}$ ) of channel #1, 5 V/div; Ch3 = input current ( $i_{EMR}$ ) of six channels, 50 mA/div; and (b)  $f_{in}$  = from 20 Hz to 50 Hz; Ch1 = output voltage ( $V_o$ ), 0.5 V/div; Ch2 = terminal voltage ( $v_{EMR}$ ) of channel #1, 5 V/div; Ch3 = input current ( $i_{EMR}$ ) of six channels, 50 mA/div.

There are two types of losses: (1) power stage losses and (2) controller losses. Since the switching losses are eliminated through the resonant operation, the power stage losses can be categorized as the transistor conduction losses and the inductor losses. The controller stage losses include losses associate with the microcontroller, operational amplifiers and demultiplexer switches.

The conduction losses ( $P_{con}$ ), including transistor turn-on conduction losses ( $P_Q$ ), inductor copper losses ( $P_{Lr}$ ) and diode forward power losses ( $P_{dr}$ ), are represented as

$$P_{con} = P_Q + P_{Lr} + P_{dr} = \sum_{i=1}^{12} R_{Q,on}^{(i)} \cdot [I_{Q,rms}^{(i)}]^2 + R_{Lr} \cdot I_{Lr,rms}^2 + V_{dr, fw} \cdot I_{dr, avg} \quad (3-33)$$

where,  $R_{Q,on}^{(i)}$  is the drain-to-source on-state resistance of the transistor at  $i^{th}$  channel,  $I_{Q,rms}^{(i)}$  is root-mean-square (RMS) value of the transistor current at  $i^{th}$  channel,  $R_{Lr}$  is the

coil resistance of the resonant inductor,  $I_{Lr,rms}$  is RMS value of the resonant inductor current,  $V_{dr,fw}$  is the forward voltage drop of the output diode, and  $I_{dr,avg}$  is the average value of the diode current. In addition, since eddy current loss is very small due to the powder core, hysteresis loss calculated using equations in [146] becomes the majority of the inductor ferrite core loss.

The total loss of the converter at 23 mW output power is 3.96 mW. Table 3.3 summarizes the loss breakdown associated with each component. According to this table, power stage loss is 2.21 mW (55.8% of total loss) and controller loss is 1.75 mW (44.2% of total loss). The power conversion efficiency at different output power levels is presented in Fig. 3.15.

TABLE 3.3  
POWER LOSS ESTIMATION OF PEI FOR MULTI-CHANNEL ENERGY HARVESTING

COMPONENT	POWER LOSS	LOSS BREAKDOWN
<b><i>Power Stage</i></b>	<b><i>2.21 mW</i></b>	<b><i>55.8%</i></b>
Transistor ( $P_Q^{(1)-(12)}$ )	0.25 mW	6.3%
Diode ( $P_{dr}$ )	0.96 mW	24.2%
Inductor coil ( $P_{Lr}$ )	0.7 mW	17.7%
Inductor core ( $P_{fer}$ )	0.3 mW	7.6%
<b><i>Controller</i></b>	<b><i>1.75 mW</i></b>	<b><i>44.2%</i></b>
Microcontroller	1.2 mW	30.3%
OpAmp	0.126 mW	3.2%
Demultiplexer	0.18 mW	4.6%
Gating	0.2 mW	5.1%
Sensing resistor	0.04 mW	1.0%

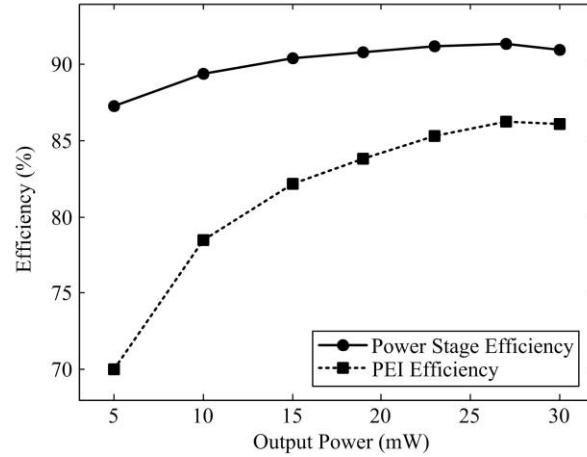
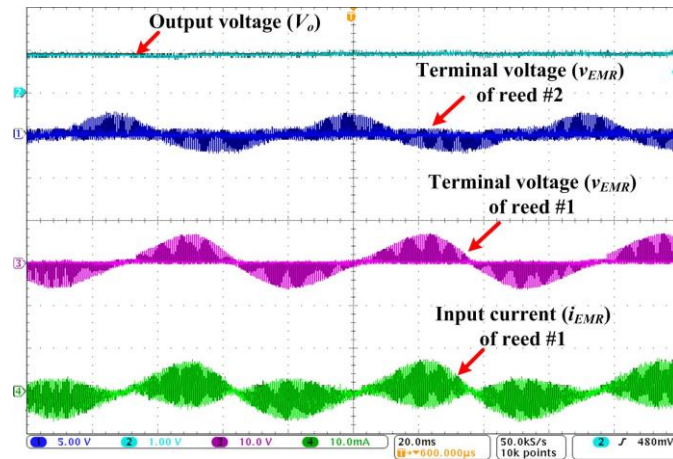
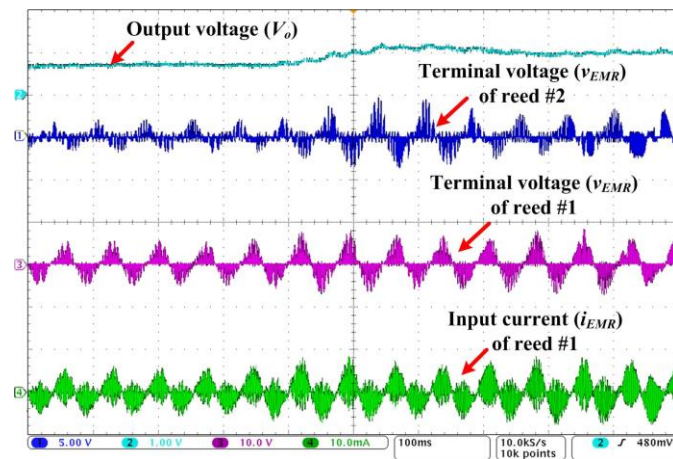


Fig. 3.15. Power conversion efficiency of the power stage and the entire PEI (including controller losses) at different output power.

To verify the circuit performance with EMR generators, the prototype is connected to the six-channel wind panel. The generators are driven by a low-speed fan and vibrate around 15 Hz. In this case, each EMR generator generates a unique EMF and power. The terminal voltages ( $v_{EMR}$ ) of channel #1 and channel #2 and the input current ( $i_{EMR}$ ) of channel #1 are measured, as depicted in Fig. 3.16. Very low power (as low as 1 mW) can be extracted at low cut-off wind speed (as low as 3m/s). The converter, connected to a 1-k $\Omega$  resistor, is capable of converting low EMFs (as low as 0.5 V<sub>rms</sub>) of six individual generators to a common dc output voltage (as high as 1.2 V), which make it suitable to charge a 1.2-V rechargeable battery.



(a)



(b)

Figure 3.16. Experimental waveforms of EMR generators: X-axis: (a) 20 ms/div; (b) 100 ms/div; Y-axis: (a) constant wind speed; (b) wind speed step change; Ch1 = terminal voltage ( $v_{EMR}$ ) of channel #2, 5 V/div; Ch2 = output voltage ( $V_o$ ), 1 V/div; Ch3 = terminal voltage ( $v_{EMR}$ ) of channel #1, 10 V/div; Ch4 = input current ( $i_{EMR}$ ) of channel #1, 10 mA/div.

### 3.6 Summary

This chapter introduces a new multi-input bridgeless resonant ac-dc converter to efficiently convert low-amplitude alternative voltages of multiple EMR generators into a regulated dc output voltage. The topology is capable of interfacing multiple, independent, alternating, input sources without using a diode bridge. Very-low-amplitude voltages can be stepped up to a relatively high voltage. Larger number of input sources result even in higher output voltage. The resonance nature of operation eliminates the switching losses, and allows high frequency switching. It also enables miniaturization through using substantially smaller capacitive and magnetic components. The multi-input converter uses the self-inductance of input sources, and only utilizes one magnetic component and one diode. Furthermore, this topology reduces the voltage stress on power transistors. The converter performance is verified through a 5-cm×3-cm standalone prototype, which converts ac voltages of a six-channel generator system into a dc output voltage. A maximum conversion efficiency of 86.3% is measured at 27-mW ac-dc power conversion. The topological concept, presented in this chapter, can be adapted for rectification of any inductive voltage sources or electromagnetic energy harvesting system.

## CHAPTER 4

### MINIATURIZED PEI DESIGN FOR AUTONOMOUS MOBILE MICROROBOTIC SYSTEMS

To introduce the resonant topological idea in the field of microrobots, this chapter proposes a novel design of bidirectional resonant dc-dc topology for driving high-voltage electrostatic actuators in mobile microrobotic systems.

#### **4.1 Operating Principle of Electrostatic Gap-closing Actuators**

Various multi-actuator configurations have increased their role in microrobot applications, such as bending mode bimorph mechanical amplifiers [8], [47], stack flextensional amplifier [21] and stepping inchworm motor [49], [50]. In majority of these actuators, high force density at the expense of small actuator travel length is required for efficient operation. The stepping inchworm motors, for instance, utilize several actuators to move a shaft step by step with nanometer precision, which brings the benefits in terms of high motion resolution, high drive force, fast dynamic response and self-locking if powered down [7]. In the case of gap closing actuators (GCA), which is the focus of this dissertation, a large displacement is achieved through using inchworm motor configurations and accumulating small displacements of actuators. The multi-actuator configuration has advantages over single-actuator configuration in terms of higher force, larger displacement and more flexible movement. However, driving strategies of multi-actuator configurations are more complicated and diverse than driving a single actuator [145], [146].

Among the multi-actuator mechanisms, electrostatic actuation has specific features in terms of straightforward fabrication, higher efficiency and fast response [7],

[19]. An in-plane gap-closing electrostatic inchworm motor with angled flexible drive arms is investigated as part of autonomous robotic legs [7]. In this study, the inchworm motor with two degree-of-freedom (DOF) operation is tested to achieve high force density and large displacement.

The electrostatic inchworm locomotion is fundamentally based on accumulating small displacements of electrostatic actuators in order to achieve a large distance movement. In-plane inchworm motion uses two or more sets of drive actuators that perform the same cyclic movements: engaging with a shuttle for a step motion, disengaging, and returning to the initial position. One end of the shuttle is connected to a mechanical load, such as a spring, to store mechanical work of each step motion. One set of actuators engages with a shuttle while another leaves the shuttle, and as a result at least one set of actuators is in contact with the shuttle to push it at a time. However, in order to prevent the shuttle rebounding from spring, additional clutch actuators are required to hold the shuttle while the drive actuators push the shuttle step by step. In an optimized inchworm motor, the inefficient clutch actuators are replaced by fixing angled flexible drive arms on the drive actuator, which in turn reduces the footprint and the driving mechanism.

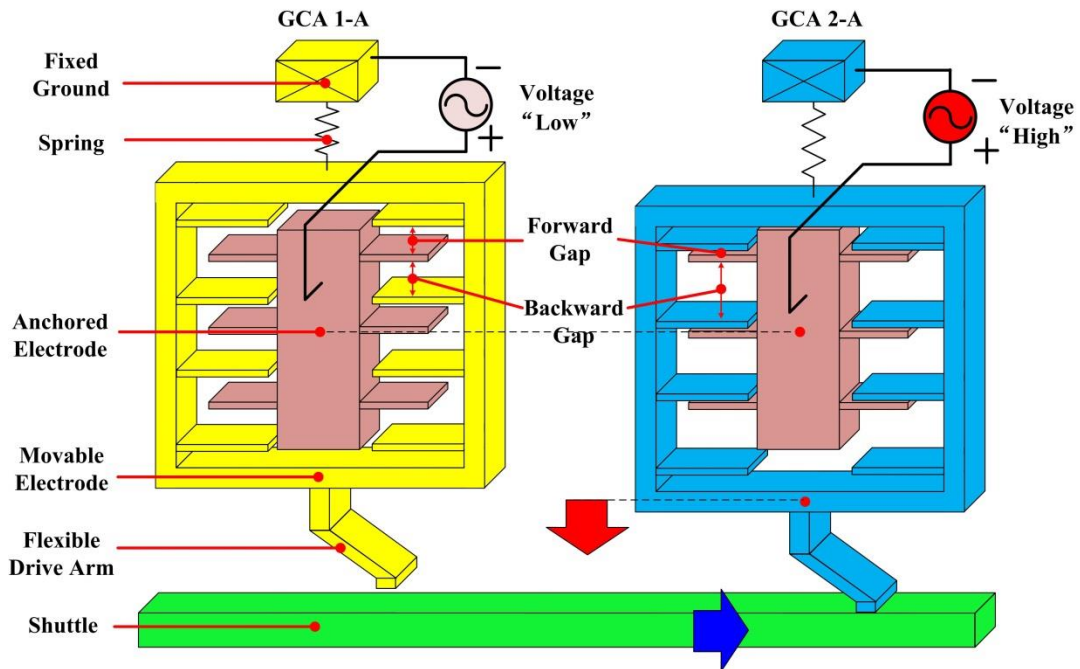


Figure 4.1. Mechanism of in-plane electrostatic gap-closing actuators (GCA) at one side of the shuttle.

Two sets of gap-closing actuators (GCA) are used as drive actuators. Each set includes two mirrored GCAs locating at both sides of the shuttle. Each GCA is composed of two comb-shaped electrodes, one of which is rigidly fixed to an anchor while the other is supported by a spring with motion perpendicular to the shuttle (see Fig. 4.1). The branches of the anchored electrode and the movable electrode interdigitate in the same plane, which generate the forward gaps and the backward gaps. The dimension of the overlapping electrodes is usually two orders of magnitude larger than the gaps. The forward gaps are set smaller than the backward gaps in equilibrium condition. Hence, the electrostatic force in the forward gaps overcomes that in the backward gap when a voltage is applied on the anchored electrode. The electrostatic force in the actuator ( $F_{es}$ ) can be expressed as [8]

$$F_{es} = \frac{1}{2} N_{br} \epsilon_0 A_{op} \left( \frac{1}{(d_{fwd} - \Delta y)^2} - \frac{1}{(d_{bwd} + \Delta y)^2} \right) V^2 \quad (4-1)$$

where,  $V$  is the voltage between interdigitated electrodes in equilibrium condition,  $\epsilon_o$  is the permittivity of free space,  $N_{br}$  is the number of the branches,  $A_{op}$  is the overlap area of each interdigitated plate,  $d_{fwd}$  and  $d_{bwd}$  are the distances of the forward gap and backward gap in equilibrium condition, and  $\Delta y$  is the actuator displacement. Therefore, the movable electrode travels toward the shuttle and engages in creating the motion.

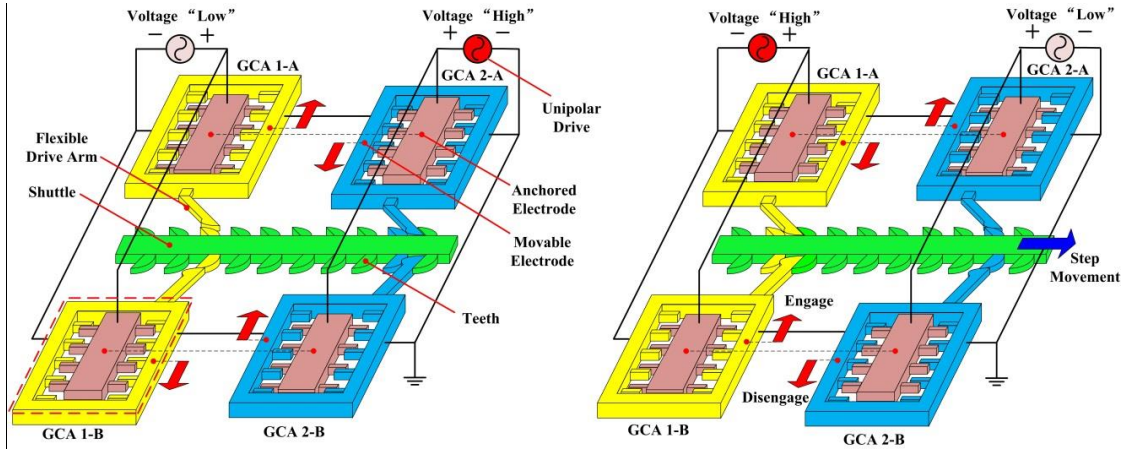


Figure 4.2. Electrostatic inchworm motor driven by two anti-phase drive signals.

The electrical energy transferred from the power source to the actuator is equal to the initial energy stored in the capacitor formed by the interdigitated electrodes. The total input energy of each GCA ( $E_{GCA}$ ) can be calculated as [8]

$$E_{GCA} = \frac{1}{2} C_{GCA} V^2 = \frac{1}{2} N_{br} \epsilon A_{op} \left( \frac{1}{d_{fwd}} + \frac{1}{d_{bwd}} \right) V^2 \quad (4-2)$$

where,  $C_{GCA}$  is the GCA capacitance,  $V$  is the voltage between interdigitated electrodes, both in equilibrium condition, and  $\epsilon$  is the static permittivity. Once the electrostatic force overcomes the stiffness of the angled flexible drive arms, the arms bend and apply forces in transverse direction to push or clutch the shuttle while the forces in longitudinal

direction cancel each other by mirrored actuators (see Fig. 4.2). The mechanical work performed by the GCA ( $W_{GCA}$ ) equals to [8]

$$W_{GCA} = F_{GCA} \Delta y = \frac{1}{2} N_{br} \varepsilon A_{op} \left( \frac{1}{d_{fwd}^2} - \frac{1}{d_{bwd}^2} \right) V^2 \Delta y \quad (4-3)$$

where,  $F_{GCA}$  is the reaction force of GCA when it engage with the shuttle.

The capacitance of GCA increases as the movable electrode travels toward the shuttle; on the other hand, the voltage decreases due to the mechanical deformation. The total unused energy left in the GCA ( $E_{GCA}^*$ ) can be represented as

$$E_{GCA}^* = E_{GCA} - W_{GCA} = \frac{1}{2} C_{GCA}^* V^{*2} = \frac{1}{2} N_{br} \varepsilon A_{op} \left( \frac{1}{d_{fwd}^*} + \frac{1}{d_{bwd}^*} \right) V^{*2} \quad (4-4)$$

where,  $C_{GCA}^*$  is the GCA capacitance,  $V^*$  is the voltage between interdigitated electrodes, and  $d_{fwd}^*$  and  $d_{bwd}^*$  are the distances of the forward gap and backward gap, all after the GCA fully engages with the shuttle. According to Eq. (4-2) to Eq. (4-4), the GCA voltage ( $V^*$ ) decreases due to the mechanical work and the increasing capacitance, calculated as

$$V^* = \frac{2\sqrt{d_{fwd}^* \cdot d_{bwd}^*}}{d_{fwd}^* + d_{bwd}^*} V \quad (4-5)$$

Hence, in order to efficiently remove such voltage ( $V^*$ ), it is necessary to recover the unused energy ( $E_{GCA}^*$ ) stored in the GCA after it fully engages with the shuttle.

## 4.2 Design of Actuator Driving Power Stage

### 4.2.1 Bidirectional Resonant DC-DC Converter

The proposed bidirectional dc-dc converter, capable of satisfying the stringent electrical and drive voltage requirements of electroactive polymer (EAP) actuators, is illustrated in Fig. 4.3. The converter consists of an inductor, a coupled inductor, two resonant capacitors and two power transistors. The input inductor  $L_{in}$  converts the input

voltage source into a current source to: (1) avoid short circuit between the input voltage source and resonant capacitors; and (2) amplify the input voltage into a pulse voltage across the power transistor  $Q_{r1}$ . The coupled inductor is tuned with two split resonant capacitors  $C_{r1}$  and  $C_{r2}$  to resonate near the switching frequency  $f_s$ . Ideally, the components  $L_p$  (self-inductance of primary coil),  $C_{r1}$  and  $C_{r2}$  ( $C_{r1}=C_{r2}$  are small resonant capacitors) present a lossless low drain-to-source impedance branch across  $Q_{r1}$  at the resonant frequency  $f_r$  near  $f_s$ .

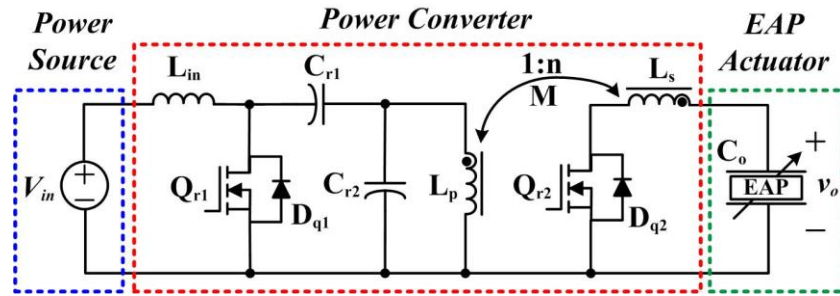


Figure 4.3. Proposed bidirectional resonant dc-dc converters for driving EAP actuators.

An amplified drain-to-source pulse voltage is generated across the active-switching transistor  $Q_{r1}$ , and its fundamental component passes through the drain-to-source impedance branch. The amplified alternating component across the primary winding of the coupled inductor is further stepped up at the secondary side with a coupling turns ratio,  $n$  ( $n > 1$ ). The parasitic capacitance  $C_{q2}$  of the transistor  $Q_{r2}$  can be an additional component of the drain-to-source impedance branch across  $Q_{r1}$  due to the effect of mutual inductance  $M$ . The body diode  $D_{q2}$  rectifies the step-up alternating voltage at the secondary side. Zero voltage switching (ZVS) and zero current switching (ZCS) are achieved in switching power transistors  $Q_{r1}$ ,  $Q_{r2}$  as well as their body diodes  $D_{q1}$ ,  $D_{q2}$ . In addition, the peak voltage stress on the power transistors is reduced due to

the voltage compensation of the split resonant capacitors. The power transistor  $Q_{r2}$  and the body diode  $D_{q1}$  are used for energy recovering during bidirectional operation.

### 4.2.2 Principle of Operation

The steady-state operation of the converter is divided into two modes: boost mode (driving actuator) and buck mode (energy recovery). During each steady-state operation mode, each switching cycle is divided into three switching sub-intervals (*Stage I ~ Stage III*). The equivalent circuits corresponding to the switching sub-intervals during boost operation are illustrated in Fig. 4.4 (a-I), Fig. 4.4 (a-II), and Fig. 4.4 (a-III). The equivalent circuits corresponding to the switching sub-intervals during buck operation are illustrated in Fig. 4.4 (b-I), Fig. 4.4 (b-II), and Fig. 4.4 (b-III). The voltage and current waveforms during boost mode and buck mode are demonstrated in Fig. 4.5 (a) and Fig. 4.5 (b), respectively. Each switching sub-intervals of the converter during boost mode is described briefly below.

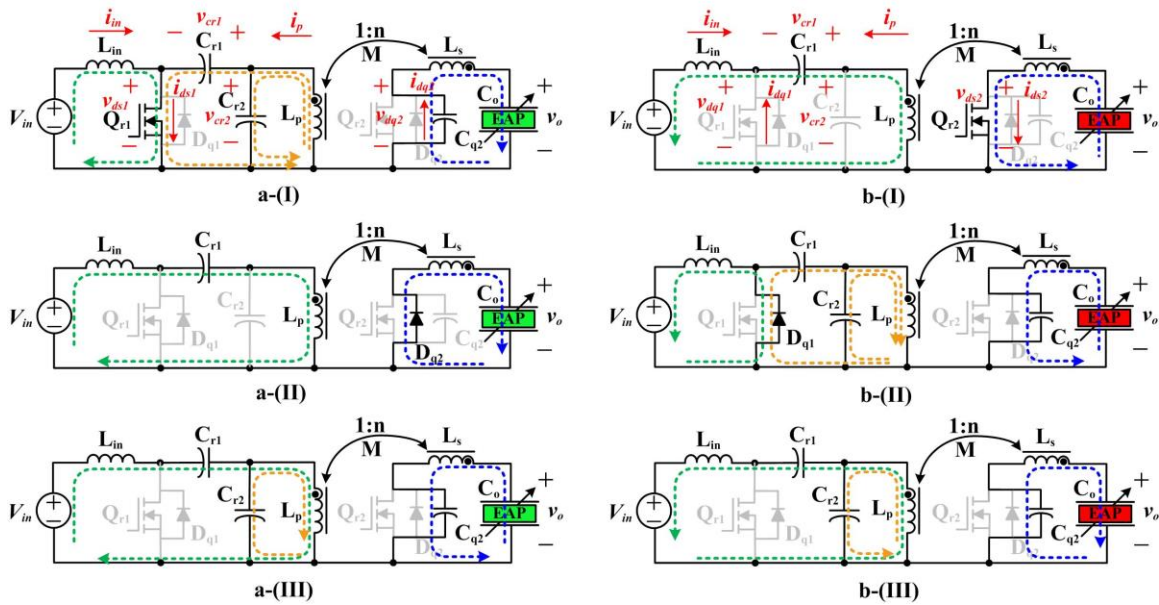


Figure 4.4. a-(I)~a-(III) Equivalent circuits corresponding to the switching sub-intervals during boost operation (driving actuators); b-(I)~b-(III) equivalent circuits corresponding to the switching sub-intervals during buck operation (energy recovery).

At  $t_0$ : (Circuit initial state) It is assumed that  $i_{in}$  has an initial value.  $v_{cr1}$  and  $v_{cr2}$  have the same negative initial values.  $v_{dq2}$  has a positive initial value.  $Q_{r1}$  is off before  $t_0$ .

*Stage I ( $t_0 \sim t_1$ ):* At  $t_0$ ,  $Q_{r1}$  is turned on at zero voltage [ $v_{ds1}(t_0)$ ] (equal to  $v_{cr2} - v_{cr1}$ ) and zero current [ $i_{ds1}(t_0)$ ].  $L_{in}$  starts to be charged by the input voltage source, thereby  $i_{in}$  increases linearly.  $C_{r1}$ ,  $C_{r2}$  and  $L_p$  begin to resonate near  $f_s$ , while  $C_{q2}$  (parasitic capacitor) resonates with  $L_s$  due to the effect of mutual inductance,  $M$ .  $v_{cr1}$  and  $v_{cr2}$  are equal and increase sinusoidally until they are equal to  $V_o/n$  at  $t_1$ .

*Stage II ( $t_1 \sim t_2$ ):* At  $t_1$ ,  $Q_{r1}$  is turned off at zero voltage [ $v_{ds1}(t_1)$ ]. The energy stored in  $L_{in}$  is transferred to the coupled inductor.  $D_{q2}$  turns on at zero voltage [ $v_{dq2}(t_1)$ ], allowing the secondary current,  $i_{dq2}$ , to freewheel through  $D_{q2}$ .  $i_{dq2}$  decreases since the secondary coil is connected to the output.  $C_{r1}$  releases the energy to  $C_o$  and  $v_{cr1}$  decreases; however,  $v_{cr2}$  is still equal to  $V_o/n$ .

*Stage III ( $t_2 \sim t_3$ ):* At  $t_2$ ,  $i_{dq2}$  drops to zero, leaving no current to freewheel through  $D_{q2}$ .  $D_{q2}$  turns off at both zero voltage [ $v_{dq2}(t_2)$ ] and zero current [ $i_{dq2}(t_2)$ ] at  $t_2$ .  $L_p$  and  $C_{r2}$  resonate while  $L_s$  and  $C_{q2}$  resonate, until  $v_{cr2}$  is equal to  $v_{cr1}$  at  $t_3$ .

At  $t_3$ :  $v_{cr2}$  is equal to  $v_{cr1}$ , followed by  $Q_{r1}$  turning on, both at zero voltage and zero current. The circuit returns to the original state.

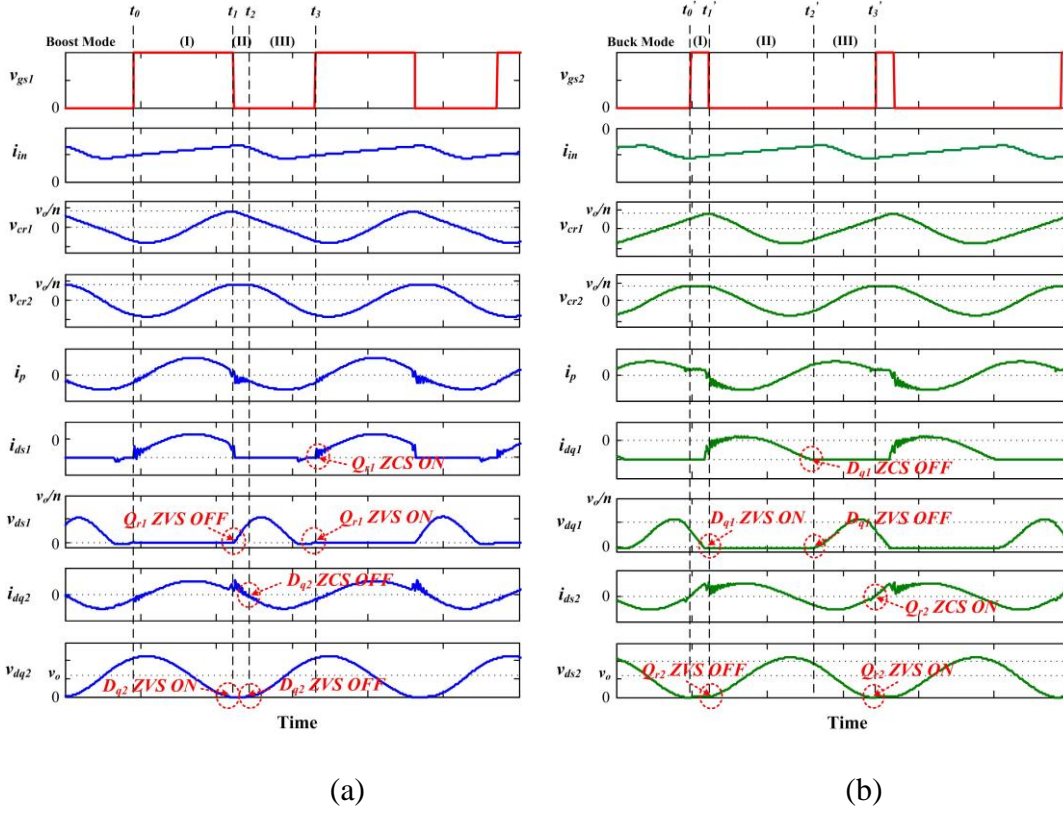


Figure 4.5. The voltage and current waveforms of the proposed converter during (a) boost mode (actuator drive), and (b) buck mode (energy recovery).

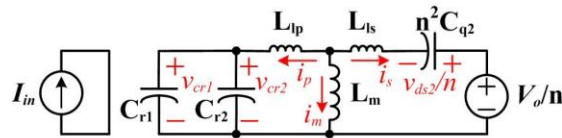
In this circuit, the input voltage source  $V_{in}$  is converted to a current source  $i_{in}$  through  $L_{in}$ .  $i_{in}$  is chopped by  $Q_{r1}$  to generate an amplified pulse voltage  $v_{ds1}$  across  $Q_{r1} \cdot L_p$ ,  $C_{r1}$ ,  $C_{r2}$  and  $C_{q2}$  serve as a lossless low drain-to-source impedance branch across  $Q_{r1}$ , allowing the fundamental component of  $v_{ds1}$  at the switching frequency to pass. The amplified ac component is then rectified to a dc voltage by  $D_{q2}$ . The input energy is first stored in  $L_{in}$  during Stage I. Then, the stored energy of  $L_{in}$  is transferred to the EAP actuator through the coupled inductor during Stage II. The coupled inductor resonates with  $C_{r1}$ ,  $C_{r2}$  and  $C_{q2}$  during Stages I and III.

Buck mode of operation is reverse of boost mode.  $Q_{r2}$  and  $D_{q1}$  are used for switching instead of  $Q_{r1}$  and  $D_{q2}$ . The unused energy of EPA actuator is first transferred

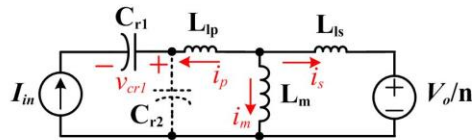
to the coupled inductor during Stage I. The stored energy is then released to the input source through  $L_{in}$  during Stage II. Similarly, the coupled inductor resonates with  $C_{r1}$ ,  $C_{r2}$  and  $C_{q2}$  during Stages II and III.

### 4.2.3 Steady-state Analysis

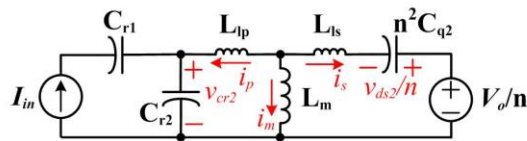
The analyses of the steady-state characteristics are based on equivalent circuit models corresponding to different switching sub-intervals, illustrated in Fig. 4.6.  $L_{in}$  is set large enough to convert the input voltage source into a voltage controlled current source  $I_{in}$ . Relative to the resonant capacitors,  $C_o$  has very small impedance at  $f_s$ , thereby it acts as a voltage source  $V_o$ . The values of  $C_{r1}$  and  $C_{r2}$  are set equal to  $C_r$  for the impedance matching. By using the transformer  $\pi$  model, the coupled inductor is composed of  $L_m$  ( $L_m=M/n$  is the magnetizing inductance),  $L_{lp}$  ( $L_{lp}=L_p-M/n$  is the equivalent leakage inductance at primary side), and  $L_{ls}$  ( $L_{ls}=L_s/n^2-M/n=L_{lp}$  is the equivalent leakage inductance at secondary side referred to the primary side). The transient waveforms and time intervals are presented in Fig. 4.5.



(a) Boost Mode I & Buck Mode II



(b) Boost Mode II & Buck Mode I



(c) Boost Mode III & Buck Mode III

Figure 4.6. Equivalent circuit model of each switching sub-intervals. (a) equivalent circuit corresponding to Stage I (boost) and Stage II (buck); (b) equivalent circuit corresponding to Stage II (boost) and Stage I (buck); (c) equivalent circuit corresponding to Stage III (boost) and Stage III (buck).

In Stage I,  $I_{in}$  is shorted while the  $L_p C_{r1} C_{r2} C_{q2}$  network is connected to  $V_o$  (see Fig. 4.6(a)).  $C_{r1}$  and  $C_{r2}$  are resonating with the coupled inductor. The governing equations in terms of  $v_{cr1}$  and  $i_m$  (current through magnetizing inductance) are presented as:

$$\begin{cases} L_m \frac{di_m(t)}{dt} - L_{lp} \frac{di_p(t)}{dt} = v_{cr1}(t) \end{cases} \quad (4-6)$$

$$\begin{cases} L_m \frac{di_m(t)}{dt} - L_{ls} \frac{di_s(t)}{dt} = \frac{V_o - v_{ds2}(t)}{n} \end{cases} \quad (4-7)$$

$$\begin{cases} \frac{dv_{cr1}(t)}{dt} = \frac{i_p(t)}{2C_r} \end{cases} \quad (4-8)$$

$$\begin{cases} \frac{1}{n} \frac{dv_{ds2}(t)}{dt} = -\frac{i_s(t)}{n^2 C_{q2}} \end{cases} \quad (4-9)$$

where,  $i_s = n * i_{dq2}$ , and  $i_m = -i_p - i_s$ . Assuming  $L_{lp} = L_{ls} \ll L_m$ , the voltages across the leakage inductances on both sides can be neglected. Hence, ( $v_{cr1}(t) \approx [V_o - v_{ds2}(t)]/n$ ), and the transient state of  $i_m$  and  $v_{cr1}$  can be expressed as:

$$\begin{cases} i_m^I(t) = i_m(t_0) \cos \omega_{r1}(t - t_0) + \frac{v_{cr1}(t_0)}{Z_{r1}} \sin \omega_{r1}(t - t_0) \end{cases} \quad (4-10)$$

$$\begin{cases} v_{cr1}^I(t) = v_{cr2}^I(t) = v_{cr1}(t_0) \cos \omega_{r1}(t - t_0) - i_m(t_0) Z_{r1} \sin \omega_{r1}(t - t_0) \end{cases} \quad (4-11)$$

where,  $\omega_{r1} = (L_m)^{-1/2} (2C_r + n^2 C_{q2})^{-1/2}$  is the angular resonance frequency of  $L_p C_{r1} C_{r2} C_{q2}$  network; and  $Z_{r1} = (L_m)^{1/2} (2C_r + n^2 C_{q2})^{-1/2}$  is the characteristic impedance of  $L_p C_{r1} C_{r2} C_{q2}$  network. Assuming  $i_m(t_0)$  is very small, the first component of  $i_m(t)$  and the second component of  $v_{cr1}(t)$  can be neglected.

During Stage II (see Fig. 4.6(b)),  $I_{in}$  is divided into  $i_m$  and  $i_s$ . The governing equations are:

$$\begin{cases} L_m \frac{di_m(t)}{dt} - L_s \frac{di_s(t)}{dt} = \frac{V_o}{n} & (4-12) \\ \frac{dv_{cr1}(t)}{dt} = -\frac{I_{in}}{C_r} & (4-13) \end{cases}$$

where,  $I_{in}=i_m+i_s$ .  $i_m$  increases linearly, while  $v_{cr1}$  decreases linearly from its boundary condition  $v_{cr1}(t_1)=V_o/n$ , yielding

$$\begin{cases} i_m''(t) = \frac{V_o}{nL_p}(t-t_1) + i_m(t_1) & (4-14) \\ v_{cr1}''(t) = -\frac{I_{in}}{C_r}(t-t_1) + \frac{V_o}{n} & (4-15) \\ v_{cr2}''(t) = \frac{V_o}{n} & (4-16) \end{cases}$$

In Stage III, the transient state of  $v_{cr2}$  is similar to those in Stage I. By applying boundary conditions  $v_{cr2}(t_2)=V_o/n$ ,  $i_p(t_2)+I_{in}=0$ , and  $i_s(t_2)=n*i_{dq2}(t_2)=0$ ,  $v_{cr2}$  can be presented as

$$v_{cr2}'''(t) = \frac{V_o}{n} \cos \omega_{r2}(t-t_2) \quad (4-17)$$

where,  $\omega_{r2}=(L_m)^{-1/2}(C_r+n^2C_{q2})^{-1/2}$  is the angular resonance frequency of  $L_pC_{r2}C_{q2}$  network; and  $Z_{r2}=(L_m)^{1/2}(C_r+n^2C_{q2})^{-1/2}$  is the characteristic impedance of  $L_pC_{r2}C_{q2}$  network. On the other hand, the transient states of  $i_m$  and  $v_{cr1}$  are similar to those of Stage II (see Fig. 4.6(c)). Since the integral of the current through  $C_{r1}$  over one switching period at steady state equals to zero;  $v_{cr1}(t_0)=v_{cr1}(t_3)$ . Using the boundary condition  $v_{cr1}(t_1)=V_o/n$  the following equation can be obtained from Eq. (4-11) and (4-15).

$$\frac{V_o}{n} \left[ 1 - \frac{1}{\cos \omega_{r1}(t_1-t_0)} \right] = \frac{I_{in}}{C_r} (t_3-t_1) \quad (4-18)$$

By setting the transistor turn-on time  $t_{on}=t_1-t_0=T_{r1}/2=\pi/\omega_{r1}$ ,  $V_o$  can be represented in terms of  $I_{in}$  as

$$V_o = \frac{nI_{in}}{2C_r} t_{off} \quad (4-19)$$

where,  $t_{off}=t_3-t_1=T_s-t_{on}$  is the turn-off time interval. By introducing the ratio of angular resonance frequency to switching frequency ( $\gamma=f_{r1}/f_s$ ) and the coefficient  $\alpha=2\gamma-1$ , Eq. (4-19) can be written as,

$$V_o = n\alpha\pi Z_m I_{in} \quad (4-20)$$

where,  $Z_m=1/(2\omega_{r1}C_r)$  is the characteristic impedance of the multi-resonant network. Therefore, the switching frequency  $f_s$  is slightly higher than the resonance frequency  $f_{r1}$  of  $L_p C_{r1} C_{r2} C_{q2}$  network. Hence, the output voltage regulation can be achieved through controlling  $f_s$ .

Eq. (4-20) reveals the fact that the multi-resonant network acts as a low drain-to-source impedance branch across transistors.  $V_o$  is determined by the current source  $I_{in}$ , through setting the network impedance to a desired value. In the case of resistive loads, the load resistance  $R_{load}$  is comparable to  $Z_m$ . Therefore, including a resistive load,  $R_{load}$ , connected to  $V_o$ , will yield:

$$\frac{V_o}{I_{in}} = (n\alpha\pi Z_m) \parallel R_{load} \quad (4-21)$$

According to Eq. (4-21) and  $V_o=I_o R_{load}$ , the output-to-input current ratio can be represented as:

$$\frac{I_o}{I_{in}} = \frac{n\alpha\pi Q_m}{n\alpha\pi Q_m + 1} \quad (4-22)$$

where,  $Q_m=Z_m/R_{load}$  denotes the quality factor. Considering a conversion efficiency of  $\eta_{ff}$ , the input power and output power of the converter should satisfy,

$$P_o = I_o^2 R_{load} = \eta_{ff} V_{in} I_{in} = \eta_{ff} P_{in} \quad (4-23)$$

Therefore, the input impedance of the converter can be expressed as

$$Z_{in} = \frac{V_{in}}{I_{in}} = \frac{R_{load}}{\eta_{ff}(1/n\alpha\pi Q_m + 1)^2} \quad (4-24)$$

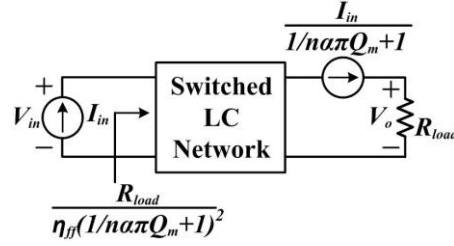


Figure 4.7. Steady state average model for the converter connected with a resistive load.

The steady-state average model is demonstrated in Fig. 4.7. The output power of the circuit is given by

$$P_o = \frac{I_{in}^2 R_{load}}{(1/n\alpha\pi Q_m + 1)^2} \quad (4-25)$$

Eq. (4-25) demonstrates the contributions of characteristic impedance and time ratio to the output power. The power capability increases by decreasing characteristic impedance  $Z_m$ , which can be achieved by either increasing  $C_{r1}$  and  $C_{r2}$  or decreasing  $L_p$ . Meanwhile, the component  $\alpha$  can be changed by adjusting switching frequency.

### 4.3 Driving Strategies for Actuator-based Inchworm Motor

#### 4.3.1 Voltage Driving Requirement

In order to efficiently drive each electrostatic actuator, a power converter is required to overcome several challenges. First, a high voltage should be applied on the anchored electrode in order to create a large electrostatic force against the load force on the spring. Higher force density and larger step motion can be achieved by applying a higher voltage. However, the electrodes may lose rigidity and touch each other if the applied voltage exceeds the limit, which consequently results in the “pull-in” instability

of GCAs (gap short circuit) [25], [26]. Therefore, the applied voltage has to be regulated in a safe range.

In addition to the voltage range, it is necessary to restore the unused energy stored in GCAs to enhance efficiency during each cyclic movement. After one GCA fully engages with the shuttle, amount of unused charge, which is not converted to mechanical work, is left behind and impedes the GCA leaving away from the shuttle. Conventionally, EAP actuators are pulled to ground instantly, leaving the unused charge to flee into the ground. An efficient driving strategy necessitates the energy recovery of actuators during each cyclic movement. Furthermore, the driving strategy should prevent the GCA failure as a result of a negative voltage that would result in the actuator travelling in an opposite direction.

The proposed resonant step-up converter is able to satisfy the stringent requirements of a single EAP actuator in terms of high driving voltage and unused energy recovery. However, one major challenge toward developing a PEI for driving multiple actuators, such as an actuator-based inchworm motor, is to design a topology associated with varied driving strategies. In order to satisfy the diverse driving requirements (wide range of driving frequencies, various driving waveforms, different correlations among driving signals), we propose using multiple converters in parallel, sharing the same power source (see Fig. 4.8). The topology is capable of providing multiple independent driving signals, with the capability of providing overlapping signals. EAP actuators can be driven with various driving waveforms (square, triangle or sinusoidal) and different correlations (simultaneous, complementary or overlapped). Furthermore, unlike the dual-stage topologies introduced in literature [17], [18] that have two stages and their overall

efficiency is equal to the product of efficiencies of two stages, the proposed topology is a single stage circuit and its efficiency can be substantially enhanced. In this work, a dual-converter topology associated with an anti-phase driving strategy is elaborated for driving an electrostatic inchworm motor.

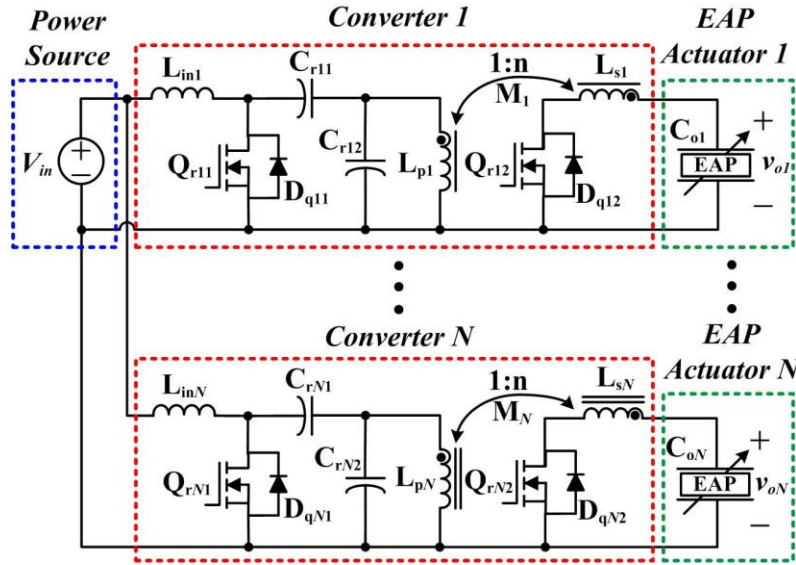


Figure 4.8. Paralleled topology for driving multiple EAP actuators.

The inchworm motor requires two anti-phase drive signals to create anti-phase motion for two sets of GCAs. By imposing two independent anti-phase voltages, two sets of flexible drive arms are capable of engaging and disengaging with the shuttle alternatively. However, two anti-phase drive signals are not absolutely complementary. Due to the time delay of mechanical deformation, the shuttle may spring back if one set of GCAs loses charge before the second set is fully engaged. Excitation voltage overlap zones between two signals are necessary to ensure that one set of GCAs is holding the shuttle until another set of GCAs is fully engaged. The proposed topology is capable of providing: (1) unipolar driving voltage; (2) high magnitude voltage; (3) energy recovery;

(4) two anti-phase signals; and (5) overlap of driving signals. It is interesting to note that these capabilities can satisfy requirements of majority of EAP actuators.

### 4.3.2 Driving Strategy with a Paralleled Topology

Two converters are connected in parallel for driving the electrostatic inchworm motor. Both converters are controlled to generate alternative driving signals with energy recovery capability. Each step of the driving strategy during one driving cycle is presented in Fig. 4.9, corresponding to the voltage on actuators and the shuttle motion.

*Step 0.5:* (before *Step 1*)  $C_{o2}$  (GCA 2-A and 2-B) is fully charged initially;  $C_{o1}$  (GCA 1-A and 1-B) is pulled to ground. The drive arms of  $C_{o2}$  engage and hold the shuttle (at S-1), while the drive arms of  $C_{o1}$  stay away from the shuttle. Both converters are in idle state.

*Step 1:* Converter 1 operates in boost mode, and the power source starts to charge  $C_{o1}$ . As soon as  $v_{o1}$  increases above the threshold voltage  $V_{th}$ , the drive arms of  $C_{o1}$  begin to engage (at S-3) and push forward the shuttle. Since  $C_{o2}$  is fully charged at the beginning of this step, the drive arms of  $C_{o2}$  stay at the initial position and clutch the shuttle before the drive arms of  $C_{o1}$  engage. Once the shuttle moves forward, the drive arms of  $C_{o2}$  bend and touch position S-2. After  $C_{o1}$  is fully charged ( $V_{o1}=V_{max}$ ), Converter 1 stops operating. Both  $v_{o1}$  and  $v_{o2}$  have high magnitude for a short interval, thereby leaving sufficient time for mechanical deformation of drive arms.

*Step 2:* Converter 2 begins to operate in buck mode after the drive arms of  $C_{o1}$  fully engage. The unused energy stored in  $C_{o2}$  returns to the power source through Converter 2. As soon as  $v_{o2}$  drops below  $V_{th}$ , the drive arms of  $C_{o2}$  disengage and leave away from the shuttle.

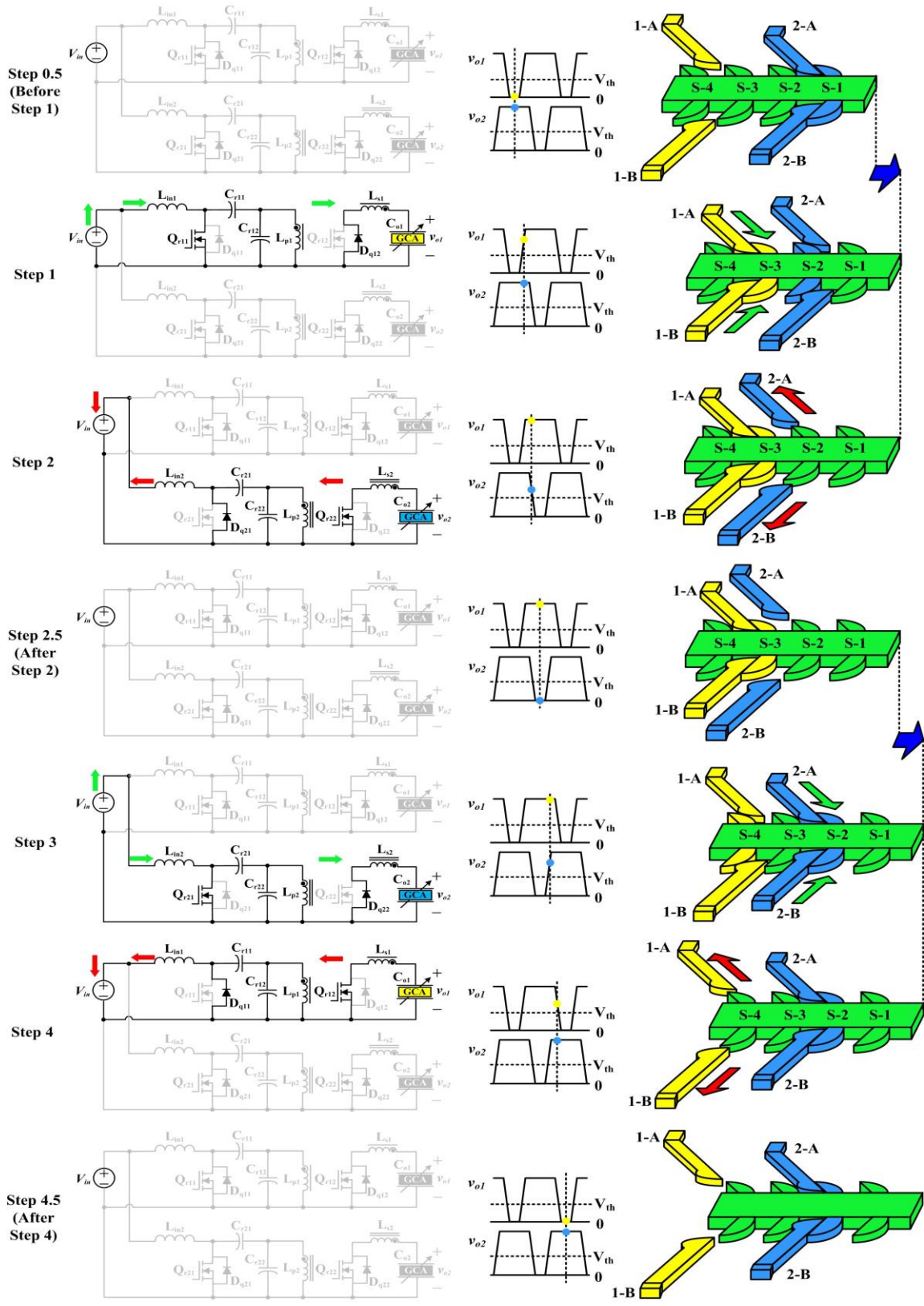


Figure 4.9. Alternative strategy for driving electrostatic multi-GCA inchworm motor.

*Step 2.5:* (after Step 2)  $C_{o1}$  is fully charged while  $C_{o2}$  is pulled to ground. The drive arms of  $C_{o1}$  hold the shuttle until the next step.

*Step 3:* Converter 2 operates in boost mode, and the power source starts to charge  $C_{o2}$ . The drive arms of  $C_{o2}$  begin to engage (at S-2) and push forward the shuttle as soon as  $v_{o2}$  is higher than  $V_{th}$ . The drive arms of  $C_{o1}$  hold the shuttle before the drive arms of  $C_{o2}$  engage. Converter 2 maintains operation until  $C_{o2}$  is fully charged ( $V_{o2}=V_{max}$ ). The overlap between  $v_{o1}$  and  $v_{o2}$  (both high) appears again in order to ensure complete mechanical deformation and avoid shuttle rebounding.

*Step 4:* Converter 1 begins to operate in buck mode as soon as the drive arms of  $C_{o2}$  fully engage. The unused energy stored in  $C_{o1}$  is returned back to the power source through Converter 1. As soon as  $v_{o1}$  drops below  $V_{th}$ , the drive arms of  $C_{o1}$  disengage and return to the initial position.

*Step 4.5:* (after Step 4) One drive cycle is completed. All components return to the initial state and the shuttle moves forward one step.

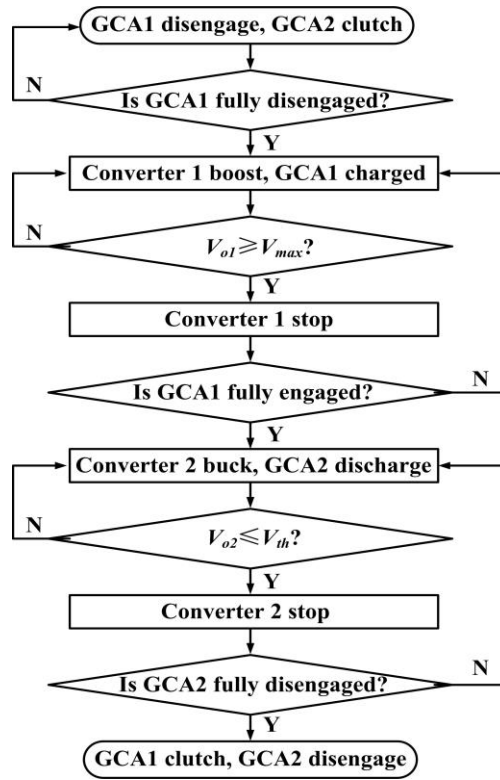


Figure 4.10. Logical flow chart of the alternative driving strategy during a half driving cycle.

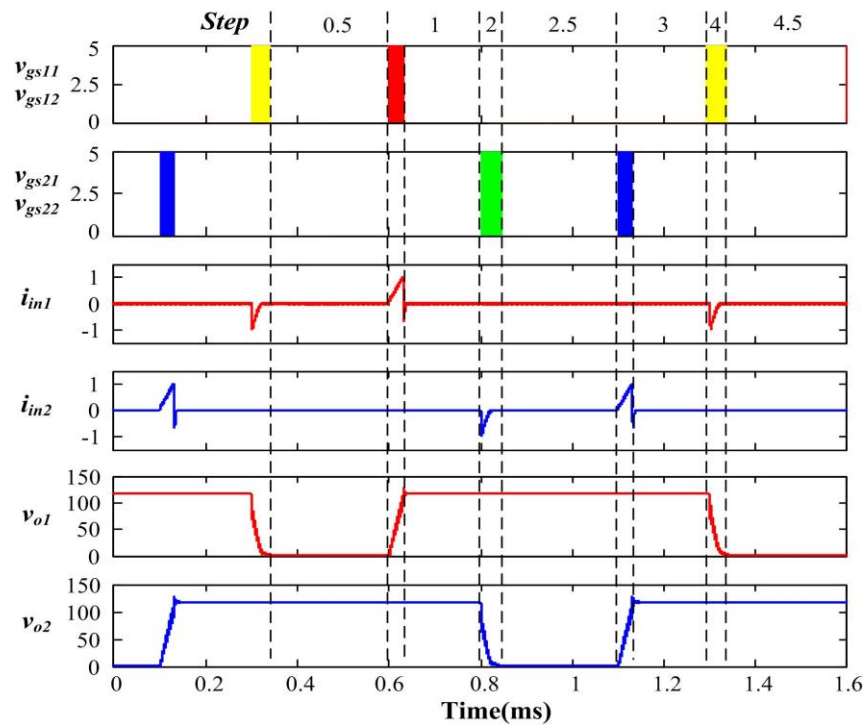


Figure 4.11. Simulation waveforms during one cycle of driving the electrostatic inchworm motor.

The logical flow chart of the driving strategy in a half driving cycle is depicted in Fig. 4.10. The simulation of driving the electrostatic inchworm motor is illustrated in Fig. 4.11. Quasi-square driving voltage is selected due to its advantage over other driving signals in terms of control simplicity, fast response and high efficiency. By applying quasi-square driving voltage, the actuators are quickly charged and discharged during step 1 to step 4, and consequently create fast mechanical deformations with maximum efficiency. The converters are disabled as soon as actuator voltages reach  $V_{max}$  or  $V_{th}$ , and consequently there will be no power conversion losses during these periods. It should be noted that quasi-square driving voltage requires feedbacks only when the actuator is fully charged or pulled to ground; however, other driving voltages such as quasi-triangle and quasi-sinusoidal voltages require more feedbacks for voltage shaping.

In addition to the voltage shape, the maximum driving frequency determined by the slew rate is another critical parameter to represent the maximum actuation speed of the inchworm motor. The driving slew rate is heavily dependent on the power capability of converters and the capacitance of actuators. Higher power capability and smaller capacitance of loads lead to a steeper rising and falling edge of voltage, corresponding to a higher driving frequency. The converter can operate with 200 mW at 2-nF loading, resulting in the actuator's voltage rise time of 50  $\mu$ s. The simulation results show that the converter is capable of driving two 2-nF EAP actuators with 3.3-V/ $\mu$ s slew rate, corresponding to the maximum driving frequency of 5 kHz.

## 4.4 Testing and Discussion

### 4.4.1 Prototypes and Design Consideration

Experimental tests on driving an electrostatic inchworm motor are presented to elaborate the performance of the proposed converter and the driving strategy, particularly with a limited footprint. A 4-mm×8-mm, 62-mg prototype dual-converter power stage, illustrated in Fig. 4.12, is developed to validate the capability of driving capacitive loads with 1.5-MHz resonant switching operation. Higher switching frequency can lead to smaller passive components; however, it results in higher conduction losses and ferrite losses, especially at miniature footprint. Therefore, the resonant switching frequency is set to 1.5 MHz with consideration of miniature commercially available packages and reasonable power conversion efficiency. Table 4.1 lists parameters of all the components adopted in the dual-converter power stage.

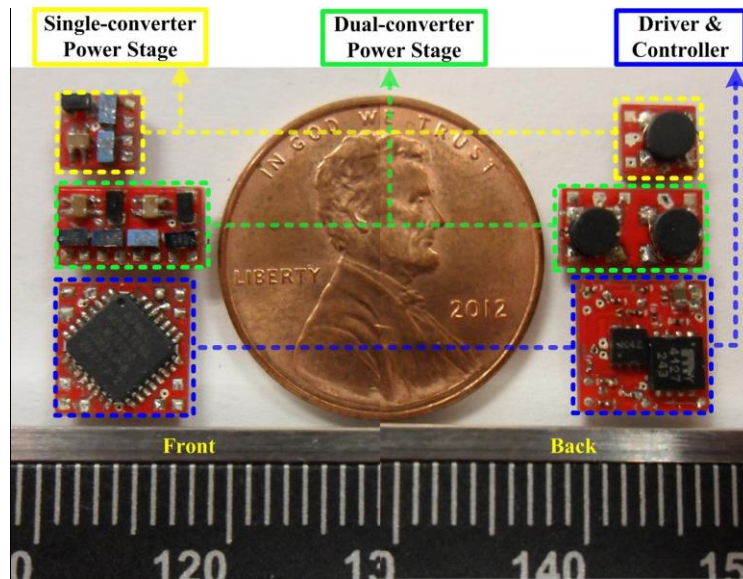


Figure 4.12. Front ( $L_{in}$ ,  $C_{r1}$ ,  $C_{r2}$ ,  $Q_{r1}$  and  $Q_{r2}$ ) and back ( $L_p$  and  $L_s$ ) views of 100-mg, 1.5-MHz experimental prototype of the paralleled resonant dc-dc converters, as well as its driver and controller.

TABLE 4.1  
COMPONENT PARAMETERS OF DUAL-CONVERTER POWER STAGE

Circuit Component	Nominal Value	No. of Unit	Unit Weight	Part Number
$L_{in}$	2.2 $\mu\text{H}$	2	8mg	Coilcraft PFL1609-222
$L_p, L_s$	1.1 $\mu\text{H}$ , 113 $\mu\text{H}$ , 1:10	2	16mg	Customized Coupled Inductor
$C_{r1}, C_{r2}$	4.7 nF	2	1mg	MLCC Array, 50V
$Q_{r1}$	40V, 10A	2	3mg	EPC2014 (GaN, Die)
$Q_{r2}$	200V, 3A	2	3mg	EPC2012 (GaN, Die)

For each resonant converter, an 8-mg chip inductor (Coilcraft PFL1609-222, 2.2  $\mu\text{H}$  at 0.47  $A_{\text{sat}}$ ) is selected as the input resonant inductor  $L_{in}$  due to its low dc resistance, small footprint and good EMI performance. The ferrite shield of the inductor keeps the magnetic field within the package, thereby reducing the EMI noise. According to the steady-state analyses, the resonant capacitance and the primary self-inductance are determined as

$$\begin{cases} C_r \cong \frac{1}{4\pi f_s Z_m} & (4-26) \\ L_p \cong \frac{Z_m C_r}{\pi f_{r1} (2C_r + n^2 C_{q2})} & (4-27) \end{cases}$$

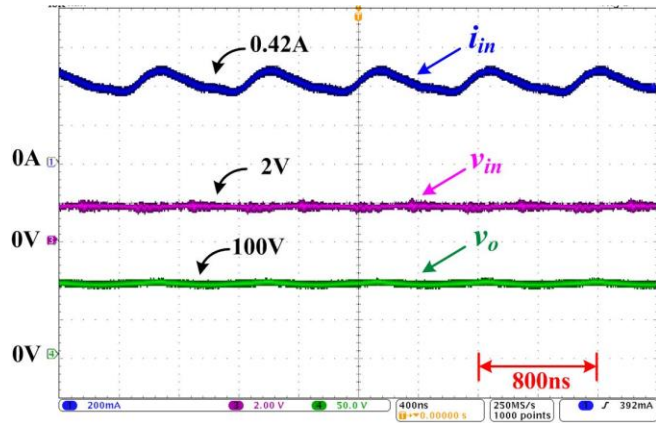
With the desired switching frequency ( $f_s=1.5\text{MHz}$ ) and characteristic impedance ( $Z_m=11\Omega$ ), the coupled inductor is customized to have 1.1- $\mu\text{H}$  primary self-inductance ( $L_p$ ). The turn ratio ( $n$ ) is set to 1:10 for a highly-step-up voltage gain. Coil windings are placed on a ferrite bobbin core due to the design simplicity and small footprint. The sizes of coil wire and ferrite core are selected with consideration of compactness and losses. A

4.7-nF/50-V ceramic capacitor array (MLCC Array) is chosen as resonant capacitors  $C_{r1}$  and  $C_{r2}$ .

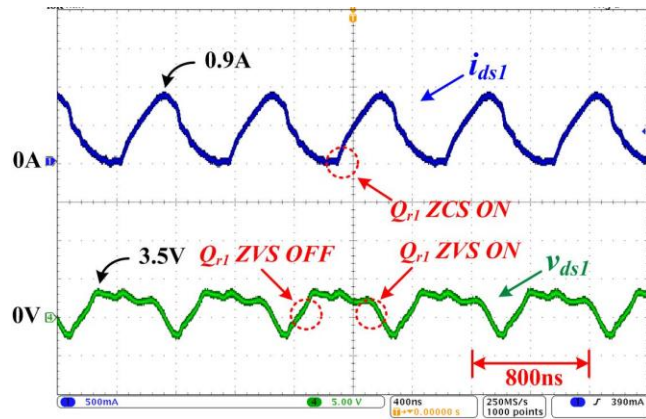
The n-channel enhancement mode Gallium-Nitride power transistors in passivated die form are selected due to their fast transient response, low gate charge, low conduction losses and compactness. The transistor (EPC2014) has very-low on-resistance (16 m $\Omega$  tested at 5-V  $V_{gs}$ ). Its features of high electron mobility and low temperature coefficient allow low conduction losses. The high-voltage transistor (EPC2012) has capability of handling 200-V drain-to-source breakdown voltage and 3-A continuous current. Its drain-to-source parasitic capacitance (70 pF tested at 100-V  $V_{ds}$ ) is used as part of the resonant network. Furthermore, the low gate charge and low gate voltage (as low as 5 V) lead to low driver power dissipation and fast gating response.

#### 4.4.2 Open-loop Operation of Single Converter

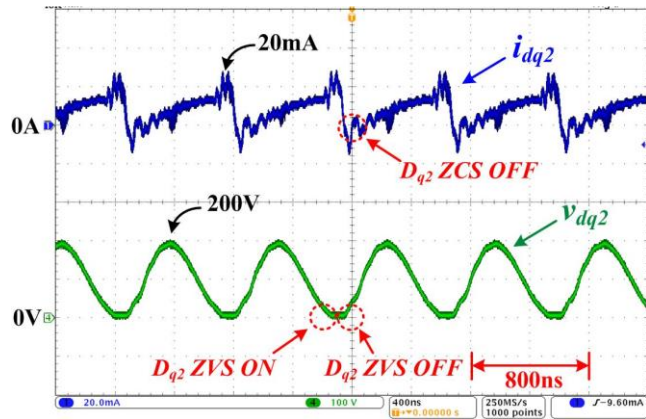
Each resonant converter is tested with open-loop 1.5-MHz switching for validation of high voltage gain and resonant switching operation. A 2-V dc power supply is utilized as the input energy source, equivalent to two series-connected 1.1-V batteries. The converter is capable of stepping the 2-V input voltage up to a 100-V dc output voltage with a 16.8-k $\Omega$  resistive load. Experimental waveforms at 600-mW constant output power are presented in Fig. 4.13. The transistor at primary side ( $Q_{r1}$ ) shows good resonant switching performances in terms of ZVS turn-on, ZVS turn-off and ZCS turn-on. In addition, resonant switching characteristics are obtained in the body diode of the transistor at secondary side ( $D_{q2}$ ). Note that the maximum voltage across  $D_{q2}$  is twice of the output voltage. A maximum dc-dc conversion efficiency of 72.6% is acquired at 100-V constant output voltage and 600-mW output power.



(a)



(b)



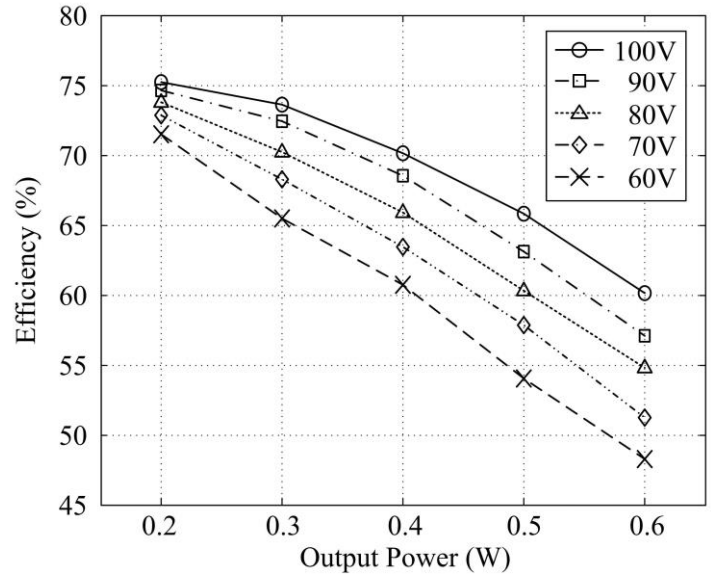
(c)

Figure 4.13. Experimental waveforms operating with  $V_{in}=2$  V,  $V_o=100$  V,  $R_{load}=16.8$  k $\Omega$ , during 1.5-MHz switching: (a)  $i_{in}$ ,  $V_{in}$  and  $V_o$ ; (b) the current  $i_{ds1}$  and voltage  $v_{ds1}$  of transistor  $Q_{r1}$ ; (c) the current  $i_{dq2}$  and voltage  $v_{dq2}$  of body diode  $D_{q2}$ .

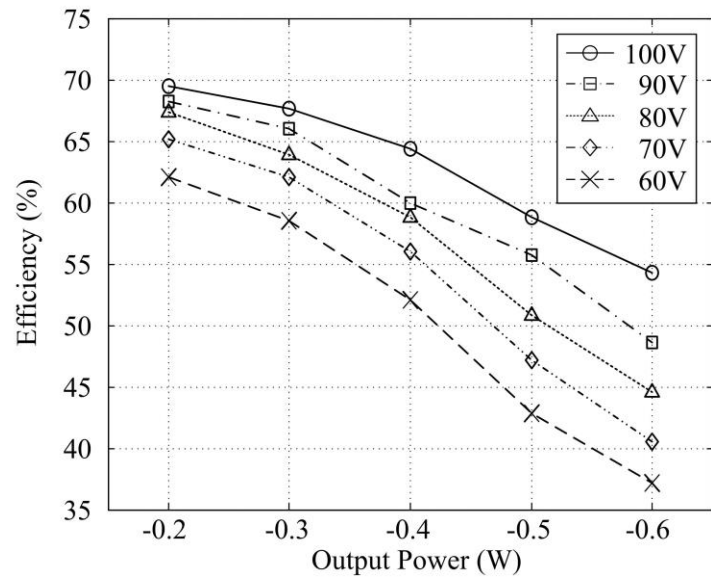
The conversion efficiency curves of each resonant converter during boost mode and buck mode, illustrated in Fig. 4.14 (a) and (b) respectively, are measured at different output powers (0.2 W~0.6 W) and output drive voltages (60 V~100 V). The drive voltage conditions are selected based on the minimum actuator threshold voltage and maximum safety voltage. According to the efficiency curves, at the same drive voltage, the conversion efficiency decreases as the output power increases. At the same delivered power, a higher efficiency is measured with a higher drive voltage. This reveals the fact that the transistor conduction losses and the inductor losses are dominant. The conduction losses ( $P_{con}$ ), including transistor turn-on conduction losses and inductor copper losses, are represented as

$$P_{con} = R_{Q,on} \cdot I_{Q,rms}^2 + R_{Lin} \cdot I_{in,rms}^2 + R_{Lp} \cdot I_{Lp,rms}^2 + R_{Ls} \cdot I_{Ls,rms}^2 \quad (4-28)$$

where,  $R_{Q,on}$  is the drain-to-source on-state resistance of each transistor,  $I_{Q,rms}$  is root-mean-square (RMS) value of the transistor current,  $R_{Lin}$ ,  $R_{Lp}$  and  $R_{Ls}$  are the coil resistances of the input inductor, the primary and secondary coupled inductor, respectively,  $I_{in,rms}$ ,  $I_{Lp,rms}$  and  $I_{Ls,rms}$  are RMS values of the input current, the primary and secondary coupled inductor currents, respectively. The hysteresis loss ( $P_{hys}$ ), which is majority of inductor's ferrite powder core losses, can be calculated using equations in [146].



(a)



(b)

Figure 4.14. Conversion efficiency versus output power of the resonant converter at different output drive voltages: (a) boost mode; (b) buck mode.

Either reducing the output power or increasing the drive voltage results in lower current RMS values, which in turn increases the efficiency. In addition, at a higher drive

voltage, the ferrite losses reduce and the efficiency increases due to a lower switching frequency of the resonant converter. The maximum efficiency is 75.2% at 200-mW output power and 100-V drive voltage. This condition satisfies the drive requirement of the electrostatic inchworm motor. The input power demands at different driving frequencies (1 kHz~3 kHz) and load capacitances (1 nF~3 nF) are presented in Fig. 4.15. Higher driving frequency and higher load capacitance result in higher input power need.

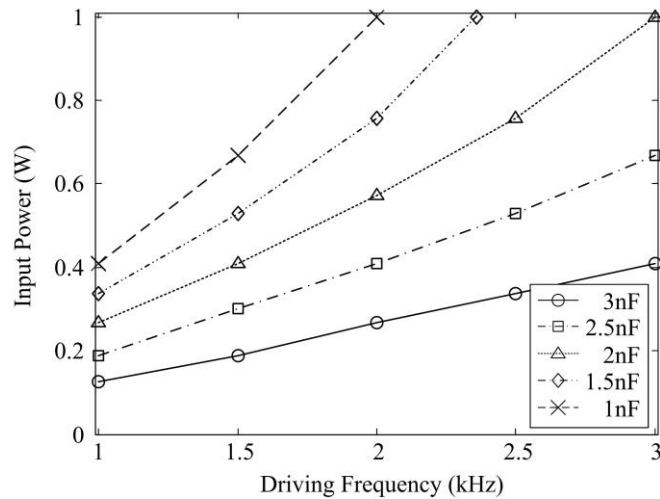


Figure 4.15. Input power demands of the converter at different driving frequencies and load capacitances.

#### 4.4.3 Inchworm Motor Actuation Validation

The experimental prototype was tested along with an electrostatic inchworm motor [7] to analyze the dynamic performance of the PEI driver. An experimental test-bed capable of testing the mechanical and electrical properties of the dynamic system is illustrated in Fig. 4.16, including the electrostatic inchworm motor on a probe station, the PEI driver, and the controller. The PEI driver and its controller are powered by a dc power supply, which emulates the low voltage energy source. The PEI output is

connected to the terminals on the probe station, while the electrostatic actuator is physically anchored by the terminals under the microscope.

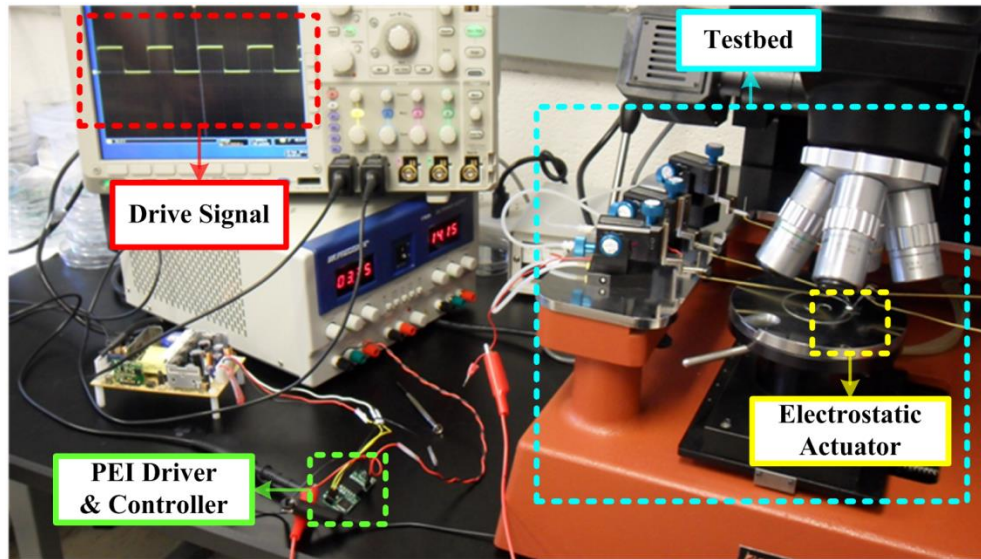


Figure 4.16. Electrostatic actuator driving test by utilizing the adopted PEI driver (500 mW, 63 mg, 31.5 mm<sup>2</sup>) and its controller [112].

A Scanning Electron Microscope (SEM) image of the inchworm motor under test is presented in Fig. 4.17. This motor utilizes the operation principle represented in Fig. 4.2 with the exception of including two more GCA arrays on the other side of the shuttle. This symmetric layout is provided to balance the normal forces on the shuttle when pushing it forward. During testing the corresponding GCA arrays, each side of the shuttle is wire-bonded together to provide a simpler signal interface to the motor (two voltage signals and ground).

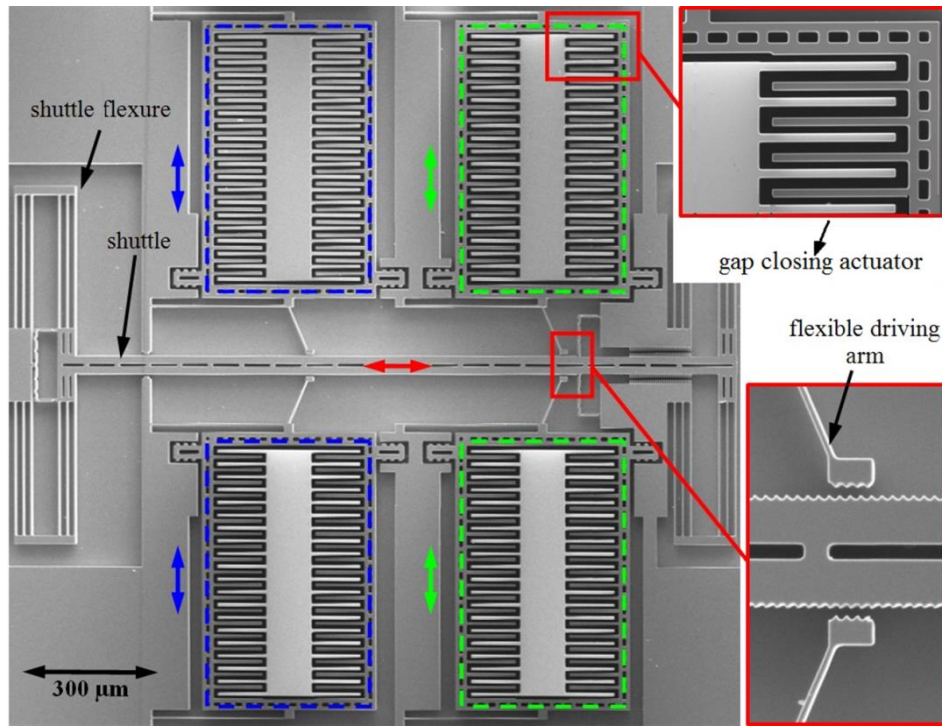


Figure 4.17. SEM image of the electrostatic actuators for inchworm motor [8].

The dual-converter power stage is tested to verify its performance for driving a gap-closing electrostatic inchworm motor. The PEI composed of a power stage, a driver and a controller is connected to the probe station where the inchworm motor is physically anchored. Each fabricated GCA acts as a few tens of pico-farad capacitor. Therefore, the capacitance is increased by cascading multiple actuators to verify the loading capacity of the circuit. The bidirectional operation of the converter enables it to charge the capacitive load and then recover the energy back to the source. Each converter is designed to charge a 2-nF actuator at up to 100 V and recover the charge at 1-kHz driving frequency. Table 4.2 lists the comparison between the proposed converter and other state of art converters for driving two high-voltage actuators. The proposed converter has superiorities in terms of small size, high power density, high efficiency and explicit drive strategy.

TABLE 4.2  
COMPARISON OF POWER STAGES FOR DRIVING HIGH-VOLTAGE ACTUATORS

Parameters	[111]	In this work
Size	152 mm <sup>2</sup>	32 mm <sup>2</sup>
Weight	90 mg	100 mg
Output Power (max.)	155 mW	600 mW
Power Density	1.7 kW/kg	6 kW/kg
Soft Switching	No	Yes
Energy Recovery	Yes	Yes
Drive Strategy	Complementary drive only	Explicit
Efficiency (max.)	38.9%	75.2%

By using the alternative driving strategy, two anti-phase quasi-square driving signals, with 100-V amplitude and 1-kHz frequency, are generated to drive two sets of actuators alternatively (see Fig. 4.18). The driving voltage is regulated at 100 V to prevent the actuators from “pull-in” instability. High-voltage overlapping zones (step 1 and step 3) are available between two signals to ensure that one set of actuators clutches the shuttle before the other set is engaged. The driving frequency is set to 1 kHz in order to acquire sufficient overlapping period for mechanical deformation. Higher driving frequency leads to faster movement of the shuttle; however, it results in less robustness and might cause spring-back [8]. The successive shuttle locomotion of inchworm motor, recorded by 300-fps high-speed video (see Fig. 4.19), elaborates more robustness and less spring-back with larger overlapping zones. The shuttle moves with 4-mm/sec average speed and reaches a maximum displacement of 60  $\mu$ m as soon as the force of spring load equals to the force of drive arms.

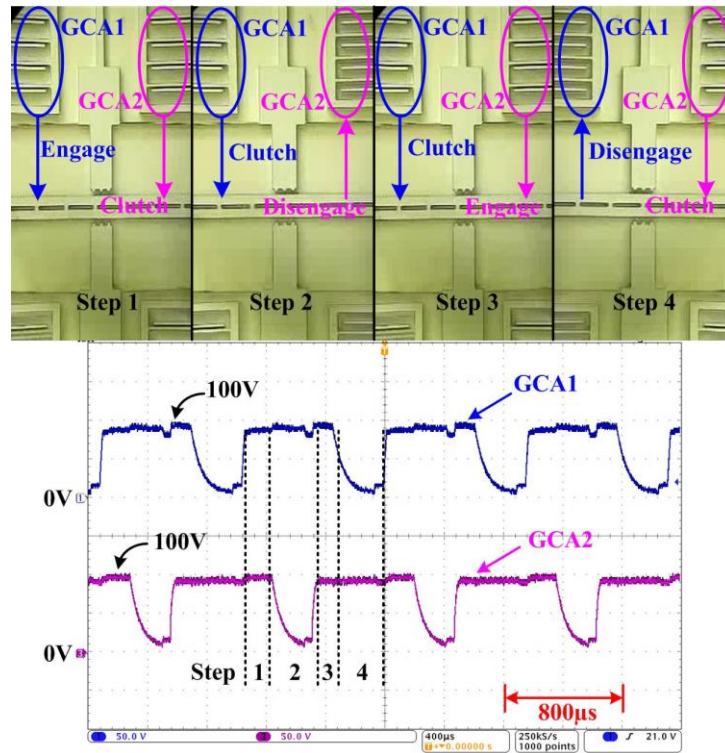


Figure 4.18. Dynamic driving performance of two sets of GCAs during one alternative driving cycle.

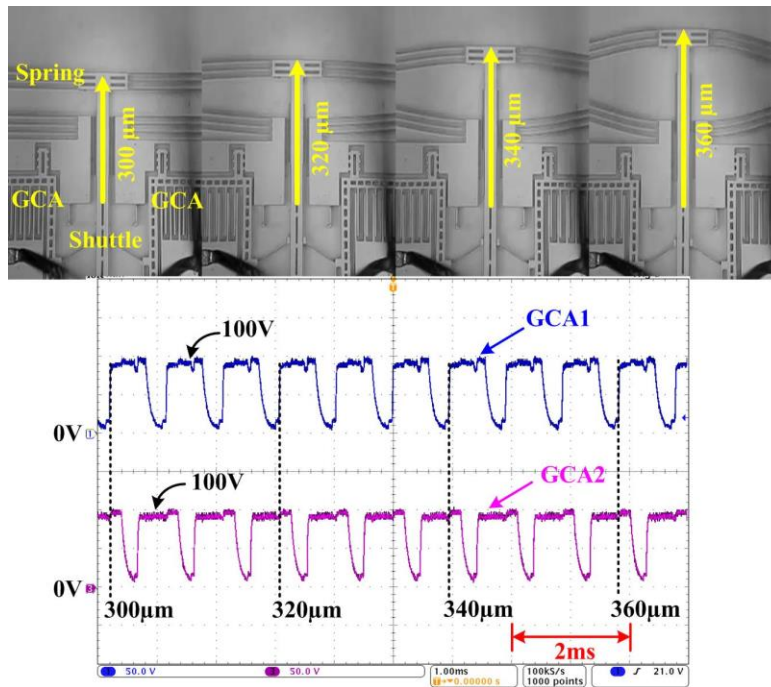


Figure 4.19. Dynamic motion of the shuttle of the inchworm motor during alternative driving process.

#### **4.5 Summary**

This chapter introduces a single-stage bidirectional resonant dc-dc converter to satisfy the drive requirements of capacitive actuators. It will potentially enable on-board power conversion due to its unique advantages in terms of milligram weight, high power density and high efficiency. The proposed converter provides high-step-up voltage gain as well as energy recovery capability to meet the stringent driving requirement of EAP actuators, while enhancing the efficiency of the power conversion and actuator system. The resonant topology provides reasonably high efficiency from light-load to full-load, due to the elimination of switching losses. High-frequency operation (up to 1.5MHz) of the converter allows miniaturization through using substantially smaller capacitive and inductive passive components. Furthermore, the topology has advantages such as reduced voltage stresses on power transistors. The work highlights the operation analyses, energy recovery control scheme, and capability of creating different driving strategies for EAP actuators. The circuit performance is verified through a 100-mg, 1.5-MHz, 600-mW prototype, which converts a 2-V input voltage into two quasi-square 100-V output voltages at 1-kHz driving frequency. A maximum conversion efficiency of 75.2% is measured at 200-mW power. Although the prototype is specified in the work for driving electrostatic actuators, the topology concept can be adapted to other EAP actuators.

## CHAPTER 5

### CONCLUSIONS AND FUTURE WORKS

This dissertation has investigated advanced technologies and potential solutions toward miniaturization of power electronic interfaces (PEI) for efficient power conditioning of advanced and ultra-compact electromechanical (EM) systems. The challenges and potential techniques toward fabricating miniaturized PEI are outlined, and the state of art in developing miniature converters is comprehensively reviewed.

#### 5.1 Conclusions

This dissertation presents novel high-frequency resonant-switching topologies as PEIs for energy harvesting and microrobotic systems.

(1) First, bridgeless resonant ac-dc step-up converters, suitable for high-frequency operation and low-voltage low-power ac-dc power conversion, are introduced for power conditioning of miniature EM systems. These single-stage topologies provide direct ac-dc power conversion with much less number of components, in comparison to other resonant topologies. Both types of converters utilize soft-switched LC networks to convert low-frequency low-amplitude alternating input voltages into a high-frequency high-amplitude alternating voltage. The high-frequency alternating signal is then rectified into a dc output voltage through a soft-switched diode. Size miniaturization and high light-load efficiency are achieved through high-frequency soft-switching, resonant gating and a simple control scheme. The performance of the circuit is verified through a 100-mg, 2-MHz prototype, which converts  $3\text{-V}_{\text{rms}}$  alternating input voltage into 7.6-V dc output voltage at 650-mW maximum output power. The circuit is designed to acquire high performance and miniature size. In addition to the size miniaturization, the circuit

efficiently addresses the low-amplitude voltage rectification with fast transient response. The topology achieves higher than 70% closed-loop efficiency across wide range of input voltages and load conditions. As this dissertation has elaborated, the topological concept can be adapted into other higher voltage and higher power applications.

(2) In the application of multi-channel energy harvesting systems, this dissertation introduces a multi-input bridgeless resonant ac-dc converter suitable for efficient, low-voltage, low-power, ac-dc power conversion of multiple electromagnetic generators. The multi-input single-stage topology is capable of directly converting independent, low-amplitude, alternative voltages of electromagnetic-reed (EMR) inductive generators to a stepped-up dc output voltage with relatively high efficiency. Low-frequency alternating voltages of EMR generators are first converted into a high-frequency alternating voltage through an LC network and then rectified into a dc output voltage through a soft-switched diode. Optimal electrical impedance matching is achieved through proper LC network design and PFM control to scavenge maximum power of EMR generators. In addition, high-frequency soft-switching increases the potential of size miniaturization without suffering from switching losses. The converter performance is verified through a 5-cm×3-cm, 48-kHz standalone prototype, which converts ac voltages of a six-channel generator system into a dc output voltage. A maximum conversion efficiency of 86.3% is measured at 27-mW ac-dc power conversion. The topological concept, presented in this dissertation, can be adapted for rectification of any inductive voltage sources or electromagnetic energy-harvesting system.

(3) In the application of mobile microrobotic systems, this dissertation introduces a bidirectional resonant dc-dc step-up converter for driving high-voltage electroactive

polymer (EAP) actuators in mobile microrobots. The single-stage topology, associated with a low input voltage source, is capable of generating a high driving voltage to efficiently excite the high-voltage EAP actuator. Highly-step-up voltage gain is acquired through a resonant-switched LC network composed of a medium-turn-ratio coupled inductor and two resonant capacitors. Size miniaturization is achieved through high-frequency resonant switching without suffering from switching losses. An alternative driving strategy is investigated through a dual-converter topology to drive an in-plane gap-closing electrostatic inchworm motor. Two anti-phase quasi-square high-amplitude voltages are generated to charge the electrostatic actuators and also recover the unused energy. High-voltage overlapping zones between two voltages increase the robustness of the inchworm motor operation. The circuit performance is verified through an 100-mg, 1.5-MHz, 600-mW prototype, which converts a 2-V input voltage into two quasi-square 100-V output voltages at 1-kHz driving frequency. A maximum conversion efficiency of 75.2% is measured at 200-mW power. The topological concept can be adapted for driving other EAP actuators.

## **5.2 Future Works**

Based on the novel topologies and the fabrication techniques investigated in this dissertation, the future work may focus on further exploring miniaturization approaches and efficient operation of converter through

1. Further increasing the switching frequency at very high frequency (above 10 MHz) to reduce size and weight of inductive and capacitive components. At very high frequency, the effort may focus on reducing resonant losses and high-frequency noises.

2. Utilizing smaller micro-coils and bare die components in the power stage to reduce the PCB footprint. Fabrication and electromagnetic optimization of micro-coil may become the main challenge.
3. Investigating chip-level packaging of the controller and the gate driver to integrate signal processing circuits into one chip. Loss mechanism, propagation delay and noise can be potentially reduced through using chip-level packaging.
4. Exploring the feasibility of using an analog controller to further reduce the size of controller and increase the speed of dynamic response. This may lead to a tradeoff between controller size and control flexibility, as the digital controller has advantages such as simplicity of implementation and configuration through software.
5. Investigating more advanced control strategy for driving actuators to increase driving speed and mechanism stability of various actuators. Different shapes of driving waveforms, including sinusoidal, triangle and trapezoidal waveforms, can be used to evaluate the performance of various actuators in different operating conditions.
6. Integrating, equipping and testing the PEI onboard of a microrobot. The effort may focus on effectively and efficiently implementing the PEI on a microrobot and investigating the impacts on maneuverability and autonomous operation of the system at dynamic environmental conditions.

## BIBLIOGRAPHY

- [1] E. P. Furlani, *Permanent Magnet and Electromechanical Devices: Materials, Analysis and Applications*. Ed. I. D. Mayergoyz. San Diego: Academic Press Series in Electromagnetism, 2001.
- [2] *MEMS Materials and Processes Handbook*. Ed. R. Ghodssi and P. Lin. Berlin: Springer, 2011.
- [3] A. Khaligh, P. Zeng, and C. Zheng, "Kinetic energy harvesting using piezoelectric and electromagnetic technologies - state of the art," *IEEE Trans. on Industrial Electronics*, vol. 57, no. 3, pp. 850-860, Mar. 2010.
- [4] C. Cepnik, R. Lausecker, and U. Wallrabe, "Review on electrodynamic energy harvesters - a classification approach," *Micromachines*, vol. 4, pp. 168-196, Apr. 2013.
- [5] R. J. Wood, "The first takeoff of a biologically-inspired at-scale robotic insect," *IEEE Trans. on Robot.*, vol. 24, no. 2, pp. 341-347, Apr. 2008.
- [6] R.C. Cope and Y. Podrazhansky, "The art of battery charging", in *Proc. IEEE Battery Conf. on Applications and Advances*, Jan. 1999, pp. 233-235.
- [7] A. Hajati and S. Kim, "Ultra-wide bandwidth piezoelectric energy harvesting," *Applied Physics Letters*, 99 (8): 083105.
- [8] I. Penskiy and S. Bergbreiter, "Optimized electrostatic inchworm motors using a flexible driving arm," *J. of Micromechanics and Microengineering*, vol. 23, no. 1, pp. 015018, Jan. 2013.
- [9] P. Sreetharan, J. Whitney, M. Strauss, and R. Wood, "Monolithic fabrication of millimeter-scale machines," *J. of Micromechanics and Microengineering*, vol. 22, no. 5, pp. 055027, Apr. 2012.
- [10] A. P. Gerratt and S. Bergbreiter, "Incorporating compliant elastomers for jumping locomotion in microrobots," *Smart Materials and Structures*, vol. 22, no. 1, pp. 014010, Dec. 2012.
- [11] A. P. Gerratt, I. Penskiy, and S. Bergbreiter, "SOI/elastomer process for energy storage and rapid release," *J. of Micromechanics and Microengineering*, vol. 20, no. 10, pp. 104011, Sep. 2010.
- [12] S. J. Roundy, "Energy Scavenging for Wireless Sensor Nodes with a Focus on Vibration to Electricity Conversion," PhD Dissertation, Dept. Mech. Eng., Univ. of California, Berkeley, CA, 2003.

- [13] E. Şahin, "Swarm Robotics: From Sources of Inspiration to Domains of Application," *Swarm Robotics: State-of-the-art Survey, Lecture Notes in Computer Science*, vol. 3342, pp. 10-20, 2005.
- [14] S. P. Beeby, R. N. Torah, M. J. Tudor, P. Glynne-Jones, T. O'Donnell, C. R. Saha, and S. Roy, "A micro electromagnetic generator for vibration energy harvesting," *J. of Micromechanics and Microengineering*, vol. 17, no. 7, pp. 1257-1265, Jul. 2007.
- [15] L. C. Rome, L. Flynn, and T. D. Yoo, "Generating electricity while walking with loads," *Science*, vol. 309, no. 5741, pp. 1725-1728, Sep. 2005.
- [16] Z. Yang, Y. Tang, P. Zeng, and A. Khaligh, "Reducing detent force while harvesting energy from center of gravity: an 11-poles, 12-slots generator design," in *Proc. IEEE Energy Conversion Congress and Exposition*, Sept. 2012, pp. 380-387.
- [17] M. El-hami, P. Glynne-Jones, N. M. White, M. Hill, S. Beeby, E. James, A. D. Brown, and J. N. Ross, "Design and fabrication of a new vibration-based electromechanical power generator," *Sensors and Actuators A: Physical*, vol. 92, no. 1-3, pp. 335-342, Aug. 2001.
- [18] S. Cheng, N. Wang, and D. P. Arnold, "Modeling of magnetic vibrational energy harvesters using equivalent circuit representations," *J. of Micromechanics and Microengineering*, vol. 17, no. 11, pp. 2328-2335, Nov. 2007.
- [19] P. Niu and P. Chapman, "Design and performance of linear biomechanical energy conversion devices," in *Proc. IEEE Power Electronics Specialists Conf.*, Jun. 2006, pp. 1-6.
- [20] M. Duffy and D. Carroll, "Electromagnetic generators for power harvesting," in *Proc. IEEE Power Electronics Specialists Conference (PESC)*, Jun. 2004, vol. 3, pp. 2075-2081.
- [21] M. Soliman, E. Abdel-Rahman, E. El-Saadany, and R. Mansour, "A wideband vibration-based energy harvester," *J. of Micromechanics and Microengineering*, vol. 18, p. 115021, 2008.
- [22] X. Xing, J. Lou, G. Yang, O. Obi, C. Driscoll, and N. Sun, "Wideband vibration energy harvester with high permeability magnetic material," *Applied Physics Letters*, 2009, 95, 134103.
- [23] C. Saha, T. O'donnell, N. Wang, and P. McCloskey, "Electromagnetic generator for harvesting energy from human motion," *Sensors and Actuators A: Physical*, vol. 147, no. 1, pp. 248-253, 2008.

- [24] N. N. H. Ching, H. Y. Wong, W. J. Li, P. H. W. Leong, and Z. Wen, "A laser-micromachined multi-modal resonating power transducer for wireless sensing systems," *Sensors and Actuators A*, 2002, 97-98, 685-690.
- [25] C. Cepnik, O. Radler, S. Rosenbaum, T. Strohla, and U. Wallrabe, "Effective optimization of electromagnetic energy harvesters through direct computation of the electromagnetic coupling," *Sensors and Actuators A*, 2011, 167, 416-421.
- [26] O. Zorlu, E. T. Topal, and H. Klah, "A vibration-based electromagnetic energy harvester using mechanical frequency up-conversion method," *IEEE Sensors J.*, vol. 11, no. 2, pp. 481-488, 2011.
- [27] G. Hatipoglu and H. rey, "FR4-based electromagnetic energy harvester for wireless sensor nodes," *Smart Materials and Structures*, vol. 19, p. 015022, 2010.
- [28] E. Bouendeu, A. Greiner, P. J. Smith, and J. G. Korvink, "Design synthesis of electromagnetic vibration-driven energy generators using a variational formulation," *J. Of Microelectromechanical Systems*, vol. 20, no. 2, pp. 466-475, 2011.
- [29] S. P. Beeby, R. N. Torah, M. J. Tudor, P. Glynne-Jones, T. O'Donnell, C. R. Saha, and S. Roy, "A micro electromagnetic generator for vibration energy harvesting," *J. of Micromechanics and Microengineering*, vol. 17, no. 7, pp. 1257-1265, Jul. 2007. [13]
- [30] M. I. Beyaz, B. M. Hanrahan, J. Feldman, and R. Ghodssi, "An integrated permanent-magnet microturbogenerator supported on microball bearings," *J. of Microelectromechanical Systems*, vol. 22, no. 3, pp. 794-803, Jun. 2013.
- [31] P. Wang, W. Li, and L. Che, "Design and fabrication of a micro electromagnetic vibration energy harvester," *J. of Semiconductors*, vol. 32, p. 104009, Oct. 2011.
- [32] I. Sari, T. Balkan, and H. Klah, "An electromagnetic micro power generator for low-frequency environmental vibrations based on the frequency upconversion technique," *J. of Microelectromechanical Systems*, vol. 19, no. 1, pp. 14-27, Feb. 2013.
- [33] Y. Jiang, S. Masaoka, T. Fujita, M. Uehara, T. Toyonaga, K. Fujii, K. Higuchi, and K. Maenaka, "Fabrication of a vibration-driven electromagnetic energy harvester with integrated NdFeB/Ta multilayered micro-magnets," *J. of Micromechanics and Microengineering*, vol. 21, p. 095014, 2011.
- [34] E. K. Reilly, F. Burghardt, R. Fain, and P. Wright, "Powering a wireless sensor node with a vibration-driven piezoelectric energy harvester," *Smart Materials and Structures*, vol. 20, p. 125006, 2011.

- [35] H. Yoon and A. Danak, "Modeling, optimization, and design of efficient initially curved piezoceramic unimorphs for energy harvesting applications," *J. of Intelligent Material Systems and Structure*, vol. 16, pp. 877-888, Oct. 2005.
- [36] D. Zhu, A. Almusallam, S. Beeby, J. Tudor, and N. Harris, "A bimorph multi-layer piezoelectric vibration energy harvester," in *Proc. PowerMEMS*, 2011.
- [37] R. Elfrink, M. Renaud, T. M. Kamel, C. de Nooijer, M. Jambunathan, M. Goedbloed, D. Hohlfeld, S. Matova, and R. van Schaijk, "Vacuum packaged MEMS piezoelectric vibration energy harvesters," in *Proc. PowerMEMS*, Dec. 2009, pp. 67-70.
- [38] R. Elfrink, T. Kamel, M. Goedbloed, S. Matova, D. Hohlfeld, Y. Van Andel, and R. Van Schaijk, "Vibration energy harvesting with aluminum nitride-based piezoelectric devices," *J. of Micromechanics and Microengineering*, vol. 19, p. 094005, Aug. 2009.
- [39] J. Q. Liu, H. B. Fang, Z. Y. Xu, X. H. Mao, X. C. Shen, D. Chen, H. Liao, and B. C. Cai, "A MEMS-based piezoelectric power generator array for vibration energy harvesting," *Microelectronics J.*, vol. 39, no. 5, pp. 802-806, Feb. 2008.
- [40] B. Lee, S. Lin, W. Wu, X. Wang, P. Chang, and C. Lee, "Piezoelectric MEMS generators fabricated with an aerosol deposition PZT thin film," *J. of Micromechanics and Microengineering*, vol. 19, p. 065014, May 2009.
- [41] D. Shen, J. H. Park, J. Ajitsaria, S. Y. Choe, H. C. Wickle, and D. J. Kim, "The design, fabrication and evaluation of a MEMS PZT cantilever with an integrated Si proof mass for vibration energy harvesting," *J. of Micromechanics and Microengineering*, vol. 18, p. 055017, Apr. 2008.
- [42] P. Glynne-Jones, S. Beeby, and N. White, "Towards a piezoelectric vibration-powered microgenerator," in *IEE Proc. Sci. Meas. Technol.*, vol. 148, no. 2, Mar. 2001, pp. 68-72.
- [43] J. Park, D. Lee, J. Park, Y. Chang, and Y. Lee, "High performance piezoelectric MEMS energy harvester based on D33 mode of PZT thin film on buffer-layer with PBTIO3 inter-layer," in *Proc. Int. Solid-State Sensors, Actuators and Microsystems Conf.*, Jun. 2009, pp. 21-25.
- [44] H. Liu, C. J. Tay, C. Quan, T. Kobayashi, and C. Lee, "Piezoelectric MEMS energy harvester for low-frequency vibrations with wideband operation range and steadily increased output power," *J. Of Microelectromechanical Systems*, vol. 20, no. 5, pp. 1131-1142, Oct. 2011.
- [45] E. Halvorsen, E. Westby, S. Husa, A. Vogl, N. Ostbo, V. Leonov, T. Sterken, and T. Kvisteroy, "An electrostatic energy harvester with electret bias," in *Proc. Int. Solid-State Sensors, Actuators and Microsystems Conf.*, Jun. 2009, pp. 1381-1384.

- [46] T. Tsutsumino, Y. Suzuki, N. Kasagi, and Y. Sakane, "Seismic power generator using high-performance polymer electret," in *Proc. Int. Conf. on Micro Electro Mechanical Systems*, Jan. 2006, pp. 98-101.
- [47] D. Hoffmann, B. Folkmer, and Y. Manoli, "Fabrication, characterization and modelling of electrostatic micro-generators," *J. of Micromechanics and Microengineering*, vol. 19, p. 094001, Aug. 2009.
- [48] R. Tashiro, N. Kabei, K. Katayama, E. Tsuboi, and K. Tsuchiya, "Development of an electrostatic generator for a cardiac pacemaker that harnesses the ventricular wall motion," *J. of Artificial Organs*, vol. 5, no. 4, pp. 239-245, 2002.
- [49] P. Basset, D. Galayko, A. M. Paracha, F. Marty, A. Dudka, and T. Bourouina, "A batch-fabricated and electret-free silicon electrostatic vibration energy harvester," *J. of Micromechanics and Microengineering*, vol. 19, p. 115025, Oct. 2009.
- [50] S. Mittal and C. H. Menq, "Hysteresis compensation in electromagnetic actuators through Preisach model inversion," *IEEE/ASME Trans. on Mechatronics*, vol. 5, pp. 394-409, Dec. 2000.
- [51] S. Towfighian, A. Seleim, E. M. Abdel-Rahman, and G. R. Heppler, "A large-stroke electrostatic micro-actuator," *J. of Micromechanics and Microengineering*, vol. 21, pp. 1-12, Jul. 2011.
- [52] A. Bransky, N. Korin, M. Khoury, and S. Levenberg, "A microfluidic droplet generator based on a piezoelectric actuator," *Lab on a Chip*, vol. 9, pp. 516-520, Nov. 2008.
- [53] G. Kovacs, L. Düring, S. Michel, and G. Terrasi, "Stacked dielectric elastomer actuator for tensile force transmission," *Sensors and Actuators A: Physical*, vol. 155, pp. 299-307, Oct. 2009.
- [54] G. D. Szarka, B. H. Stark, and S. G. Burrow, "Review of power conditioning for kinetic energy harvesting systems," *IEEE Trans. on Power Electronics*, vol. 27, no. 2, pp. 803-815, Feb. 2012.
- [55] T. T. Le, J. Han, A. V. Jouanne, K. Mayaram, and T. S. Fiez, "Piezoelectric micro-power generation interface circuits," *IEEE J. of Solid-State Circuits*, vol. 41, no. 6, pp. 1411-1420, Jun. 2006.
- [56] J. C. Farrarons, P. M. Català, A. S. Vela, M. P. Vidal, and J. Samitier, "Power-conditioning circuitry for a self-powered system based on micro PZT generators in a 0.13- $\mu\text{m}$  low-voltage low-power technology," *IEEE Trans. on Industrial Electronics*, vol. 55, no. 9, pp. 3249-3257, Sept. 2008.

- [57] S. Hashemi, M. Sawan, and Y. Savaria, "A novel low-drop CMOS active rectifier for RF-powered devices: experimental results," *Microelectronics J.*, vol. 40, pp. 1547-1554, 2009.
- [58] S. Guo and H. Lee, "An efficiency-enhanced integrated CMOS rectifier with comparator-controlled switches for transcutaneous powered implants," in *Proc. IEEE Custom Intergrated Circuits Conference*, 2007, pp. 385-388.
- [59] G. Bawa and M. Ghovanloo, "Analysis, design, and implementation of a high-efficiency full-wave rectifier in standard CMOS technology," *IEEE J. of Analog Integrated Circuits and Signal Processing*, vol. 60, no. 1, pp. 71-81, 2009.
- [60] P. M. Lin, "Topological generation and analysis of voltage multiplier circuits," *IEEE Trans. on Circuits Syst.*, vol. CAS-24, no. 10, pp. 517-530, Oct. 1977.
- [61] C. K. Tse, S. C. Wong, and M. H. L. Chow, "On lossless switched capacitor power converters," *IEEE Trans. Power Electronics*, vol. 10, no. 3, pp. 286-291, May 1995.
- [62] S. Cheng, Y. Jin, Y. Rao, and D. P. Arnold, "A bridge voltage doubler ac/dc converter for low-voltage energy harvesting applications," in *Proc. PowerMEMS*, Washington D.C., Dec. 2009, pp. 25-28.
- [63] J. C. Salmon, "Circuit topologies for single-phase voltage-doubler boost rectifiers," *IEEE Trans. on Power Electronics*, vol. 8, no. 4, pp. 521-529, 1993.
- [64] R. Itoh and K. Ishizaka, "Single-phase sinusoidal convertor using MOSFETs," in *Proc. IEE Electric Power Applications*, vol. 136, no. 5, pp. 237-242, 1989.
- [65] P. D. Mitcheson, T. C. Green, and E. M. Yeatman, "Power processing circuits for electromagnetic, electrostatic and piezoelectric inertial energy scavengers," *Microsyst. Technol.*, vol. 13, pp. 1629-1635, Jul. 2007.
- [66] S. Dwari and L. Parsa, "An efficient ac-dc step-up converter for low-voltage energy harvesting," *IEEE Trans. on Power Electronics*, vol. 25, no. 8, pp. 2188-2199, Aug. 2010.
- [67] H. Wang, Y. Tang, and A. Khaligh, "A bridgeless boost rectifier for low voltage energy harvesting applications," *IEEE Trans. on Power Electronics*, vol. 28, no.11, pp. 5206-5214, Jan. 2013.
- [68] S. Dwari and L. Parsa, "Efficient low voltage direct ac/dc converters for self-powered wireless sensor nodes and mobile electronics," in *Proc. 30th IEEE Int. Telecommun. Energy Conf.*, San Diego, CA, Sep. 2008, pp. 1-7.

- [69] R. Dayal, S. Dwari, and L. Parsa, "A new design for vibration-based electromagnetic energy harvesting systems using coil inductance of microgenerator," *IEEE Trans. on Industry Applications*, vol. 47, no. 2, pp. 820-830, Mar. 2011.
- [70] R. Dayal and L. Parsa, "A new single stage ac-dc converter for low voltage electromagnetic energy harvesting," in *Proc. Energy Conversion Congress and Exposition*, Sept. 2010, pp. 4447-4452.
- [71] I. D. Mayergoyz and P. McAvoy, *Fundamentals of Electric Power Engineering*. Singapore: World Scientific, 2014.
- [72] R. Moghe, D. Divan, and F. Lambert, "Powering low-cost utility sensors using energy harvesting," in *Proc. 14th European Conf. on Power Electronics and Applications*, Aug. 2011, pp. 1-10.
- [73] E. Lefeuvre, D. Audigier, C. Richard, and D. Guyomar, "Buck-boost converter for sensorless power optimization of piezoelectric energy harvester," *IEEE Trans. on Power Electronics*, vol. 22, no. 5, pp. 2018-2025, Sept. 2007.
- [74] G. K. Ottman, H. F. Hofmann, and G. A. Lesieutre, "Optimized piezoelectric energy harvesting circuit using step-down converter in discontinuous conduction mode," *IEEE Trans. on Power Electronics*, vol. 18, no. 2, pp. 696-703, 2003.
- [75] A. Badel, A. Benayad, E. Lefeuvre, L. Lebrun, C. Richard, and D. Guyomar, "Single crystals and nonlinear process for outstanding vibration-powered electrical generators," *IEEE Trans. on Ultrasonics, Ferroelectrics, and Frequency Control*, vol. 53, no. 4, pp. 673-684, 2006.
- [76] A. Tabesh and L. G. Fr chette, "A low-power stand-alone adaptive circuit for harvesting energy from a piezoelectric micropower generator," *IEEE Trans. on Industrial Electronics*, vol. 57, no. 3, pp. 840-849, 2010.
- [77] E. Lefeuvre, A. Badel, C. Richard, and D. Guyomar, "Piezoelectric energy harvesting device optimization by synchronous electric charge extraction," *J. of Intelligent Material Systems and Structures*, vol. 16, no. 10, pp. 865-876, 2005.
- [78] D. Guyomar, A. Badel, E. Lefeuvre, and C. Richard, "Toward energy harvesting using active materials and conversion improvement by nonlinear processing," *IEEE Trans. on Ultrasonics, Ferroelectrics and Frequency Control*, vol. 52, no. 4, pp. 584-595, Apr. 2005.
- [79] L. Garbuio, M. Lallart, D. Guyomar, C. Richard, and D. Audigier, "Mechanical energy harvester with ultralow threshold rectification based on SSHI nonlinear technique," *IEEE Trans. on Industrial Electronics*, vol. 56, no. 4, pp. 1048-1056, Apr. 2009.

- [80] M. Lallart, C. Richard, L. Garbuio, L. Petit, and D. Guyomar, "High efficiency, wide load bandwidth piezoelectric energy scavenging by a hybrid nonlinear approach," *Sensors and Actuators A: Physical*, vol. 165, no. 2, pp. 294-302, 2011.
- [81] E. Dallago, D. Miatton, G. Venchi, V. Bottarel, G. Frattini, G. Ricotti, and M. Schipani, "Electronic interface for piezoelectric energy scavenging system," in *Proc. IEEE 34th Solid-State Circuits Conf.*, Sept. 2008, pp. 402-405.
- [82] B. H. Stark, P. D. Mitcheson, P. Miao, T. C. Green, E. M. Yeatman, and A. S. Holmes, "Converter circuit design, semiconductor device selection and analysis of parasitics for micropower electrostatic generators," *IEEE Trans. on Power Electronics*, vol. 21, no. 1, pp. 27-37, 2006.
- [83] G. Despesse, T. Jager, J. Chaillout, J. L  ger, A. Vassilev, S. Basrour, and B. Charlot, "Fabrication and characterization of high damping electrostatic micro devices for vibration energy scavenging," in *Proc. Design, Test, Integration and Packaging of MEMS and MOEMS*, Jan. 2005, pp. 386-390.
- [84] B. C. Yen and J. H. Lang, "A variable-capacitance vibration-to-electric energy harvester," *IEEE Trans. on Circuits and Systems I: Regular Papers*, vol. 53, no. 2, pp. 288-295, Feb. 2006.
- [85] J. O. Mur-Miranda, "MEMS-Enabled Electrostatic Vibration-to-Electric Energy Conversion," PhD Dissertation, Dept. of Elec. and Comp. Eng., Massachusetts Institute of Technology, 2003.
- [86] E. O. Torres and G. A. Rinc  n-Mora, "Electrostatic energy-harvesting and battery-charging CMOS system prototype," *IEEE Trans. on Circuits and Systems I: Regular Papers*, vol. 56, no. 9, pp. 1938-1948, 2009.
- [87] D. Kwon, G. A. Rinc  n-Mora, and E. O. Torres, "Harvesting ambient kinetic energy with switched-inductor converters," *IEEE Trans. on Circuits and Systems I: Regular Papers*, no. 99, pp. 1-1, 2011.
- [88] J. Kassakian, M. Schlecht, and G. Verghese, *Principles of Power Electron.* New York: Addison-Wesley, 1991.
- [89] F. C. Lee, "High-frequency quasi-resonant converter technologies," in *Proc. IEEE Conf.*, Apr. 1988, vol. 76, no. 4, pp. 377-390.
- [90] W. Tabisz and F. C. Lee, "Zero-voltage-switching multiresonant technique - a novel approach to improve performance of high-frequency quasiresonant converters," *IEEE Trans. on Power Electronics*, vol. 4, no. 4, pp. 450-458, Oct. 1989.

- [91] W. Tabisz and F. C. Lee, "Principles of quasi- and multi-resonant power conversion techniques," in *Proc. IEEE Intel. Sym. on Circuits and Systems*, Jun. 1991, vol. 2, pp. 1053-1056.
- [92] J. Sebastian, J. A. Martinez, J. M. Alonso, J. A. Cobos, "Voltage-follower control in zero-current-switched quasi-resonant power factor preregulators," *IEEE Trans. on Power Electronics*, vol. 13, no. 4, pp. 727-738, Jul. 1998.
- [93] H. Bodur, and A. F. Bakan, "A new ZVT-PWM dc-dc converter," *IEEE Trans. on Power Electronics*, vol. 17, no. 1, pp. 40-47, Jan. 2002.
- [94] I. Aksoy, H. Bodur, and A. F. Bakan, "A new ZVT-ZCT-PWM dc-dc converter," *IEEE Trans. on Power Electronics*, vol. 25, no. 8, pp. 2093-2105, Aug. 2010.
- [95] R. Redl, B. Molnar, and N. Sokal, "Class E resonant regulated dc/dc power converters: analysis of operations and experimental results at 1.5 MHz," *IEEE Trans. on Power Electronics*, vol. PE-1, no. 2, pp. 111-120, Apr. 1986.
- [96] B. Tomescu, "A unified approach to Class E versus quasi-resonant switch topologies," *IEEE Trans. on Circuits and Systems-II: Analog and Digital Signal Processing*, vol. 45, no. 6, pp. 763-766, Jun. 1998.
- [97] J. Hu, A. D. Sagneri, J. M. Rivas, Y. Han, S. M. Davis, and D. J. Perreault, "High-frequency resonant SEPIC converter with wide input and output voltage ranges," *IEEE Trans. on Power Electronics*, vol. 27, no. 1, pp. 189-200, Jan. 2012.
- [98] R. C. N. Pilawa-Podgurski, A. D. Sagneri, J. M. Rivas, D. I. Anderson, and D. J. Perreault, "Very-high-frequency resonant boost converters," *IEEE Trans. on Power Electronics*, vol. 24, no. 6, pp. 1654-1665, Jun. 2009.
- [99] J. M. Rivas, R. S. Wahby, J. S. Shafran, and D. J. Perreault, "New architectures for radio-frequency dc-dc power conversion," *IEEE Trans. on Power Electronics*, vol. 21, no. 2, pp. 380-392, Mar. 2006.
- [100] N. Mohan, T. M. Undeland, and W. P. Robbins, *Power Electronics: Converters, Applications, and Design*, New York: Wiley, 1995.
- [101] Y. Tang and A. Khaligh, "Miniaturized bridgeless high-frequency resonant ac-dc step-up/step-down converters," *IEEE Trans. on Power Electronics*, vol. 29, no. 12, pp. 6518-6533, Dec. 2014.
- [102] Y. Tang and A. Khaligh, "A novel bridgeless high-frequency resonant ac-dc converter," in *Proc. IEEE Applied Power Electronics Conf. and Expo.*, Fort Worth, TX, Mar. 2014, pp. 125-130.

- [103] M. Karpelson, G.Y. Wei, and R. J. Wood, "A review of actuation and power electronics options for flapping-wing robotic insects," in *Proc. IEEE Int. Conf. on Robotics and Automation*, Pasadena, CA, May 2008.
- [104] A. Wilhelm, B. W. Surgenor, and J. G. Pharoah, "Evaluation of a micro fuel cell as applied to a mobile robot," in *Proc. IEEE Int. Conf. on Mechatronics and Automation*, Niagara Falls, Canada, Aug. 2005.
- [105] C. L. Bellew, S. Hollar, and K. S. J. Pister, "An SOI process for fabrication of solar cells, transistors and electrostatic actuators," in *Proc. Int. Conf. on Solid-State Sensors, Actuators and Microsystems*, Boston, MA, Jun. 2003.
- [106] R. Yeh, S. Hollar, and K. S. J. Pister, "Single mask, large force, and large displacement. Electrostatic linear inchworm motors," *J. of Microelectromechanical Systems*, vol. 11, pp. 330-336, Aug. 2002.
- [107] M. P. de Boer, D. L. Luck, and W. R. Ashurst, "High-performance surface-micromachined inchworm actuator," *J. of Microelectromechanical Systems*, vol. 13, pp. 63-74, Feb. 2004.
- [108] E. Steltz, M. Seeman, S. Avadhanula, and R. S. Fearing, "Power electronics design choice for piezoelectric microrobots," in *Proc. IEEE/RSJ Int. Conf. on Intelligent Robots and Systems*, 2006, pp. 1322–1328.
- [109] D. Campolo, M. Sitti, and R. S. Fearing, "Efficient charge recovery method for driving piezoelectric actuators with quasi-square waves," *IEEE Transactions on Ultrasonics, Ferroelectrics, and Frequency Control*, vol. 50, no. 3, Mar. 2003.
- [110] M. Karpelson, J. P. Whitney, G. Wei, and R. J. Wood, "Design and fabrication of ultralight high-voltage power circuits for flapping-wing robotic insects," in *Proc. IEEE Applied Power Electronics Conf.*, Mar. 2011, pp. 2070-2077.
- [111] M. Karpelson, G. Wei, and R. J. Wood, "Driving high voltage piezoelectric actuators in microrobotic applications," *Sensors and Actuators A: Physical*, vol. 176, pp. 78-89, Apr. 2012.
- [112] Y. Tang, C. Chen, A. Khaligh, I. Penskiy, and S. Bergbreiter, "An ultracompact dual-stage converter for driving electrostatic actuators in mobile microrobots," *IEEE Trans. on Power Electronics*, vol. 29, no. 6, pp. 2991-3000, Jun. 2014.
- [113] C. Chen, Y. Tang, A. Khaligh, and R. W. Newcomb, "A low-power and high-gain converter for driving dielectric elastomer actuators," in *Proc. IEEE Applied Power Electronics Conf. and Expo.*, Long Beach, CA, Mar. 2013, pp. 2755-2760.

- [114] G. K. Ottman, H. F. Hofmann, A. C. Bhatt, and G. A. Lesieutre, "Adaptive piezoelectric energy harvesting circuit for wireless remote power supply," *IEEE Trans. on Power Electronics*, vol. 17, no. 5, pp. 669-676, Sept. 2002.
- [115] Y. K. Ramadass and A. P. Chandrakasan, "An efficient piezoelectric energy harvesting interface circuit using a bias-flip rectifier and shared inductor," *IEEE J. of Solid-State Circuits*, vol. 45, no. 1, pp. 189-204, Jan. 2010.
- [116] S. Xu, K. D. T. Ngo, T. Nishida, G. Chung, and A. Sharma, "Converter and controller for micro-power energy harvesting," in *Proc. 20th Applied Power Electronics Conf. and Expo.*, vol. 1, Mar. 2005, pp. 226-230.
- [117] H. Lee and P. K. T. Mok, "An SC voltage doubler with pseudo-continuous output regulation using a three-stage switchable opamp," *IEEE J. of Solid-State Circuits*, vol. 42, no. 6, pp. 1216-1229, Jun. 2007.
- [118] J. Xiao, A. Peterchev, J. Zhang, and S. Sanders, "An ultra-low-power digitally-controlled buck converter IC for cellular phone applications," in *Proc. 19th Applied Power Electronics Conf. and Expo.*, vol. 1, Mar. 2004, pp. 383-391.
- [119] L. Xue, C. Meyer, C. M. Dougherty, and S. Bedair, "Towards miniature step-up power converters for mobile microsystems," in *Proc. 26th Applied Power Electronics Conf. and Expo.*, Mar. 2011, pp. 1451-1455.
- [120] Y. K. Ramadass and A. P. Chandrakasan, "Voltage scalable switched capacitor DC-DC converter for ultra-low-power on-chip applications," in *Proc. Power Electronics Specialists Conf.*, Jun. 2007, pp. 2353-2359.
- [121] A. Richelli, L. Colalongo, S. Tonoli, and Z. M. Kovacs-Vajna, "A 0.2-1.2 V DC/DC boost converter for power harvesting applications," *IEEE Trans. on Power Electronics*, vol. 24, no. 6, pp. 1541-1546, Jun. 2009.
- [122] E. J. Carlson, K. Strunz, and B. P. Otis, "A 20 mV input boost converter with efficient digital control for thermoelectric energy harvesting," *IEEE J. of Solid-State Circuits*, vol. 45, no. 4, pp. 741-750, Apr. 2010.
- [123] A. Uddin, S. Yemenicioglu, C. Chen, E. Corigliano, K. Milaninia and L. Theogarajan, "Integration of solid-state nanopores in a 0.5  $\mu\text{m}$  CMOS foundry process," *Nanotechnology*, vol. 24, p. 155501, Mar. 2013.
- [124] M. Lallart and D. Guyomar, "An optimized self-powered switching circuit for non-linear energy harvesting with low voltage output," *Smart Materials and Structures*, vol. 17, p. 035030, May 2008.
- [125] J. H. Lau and S.W. R. Lee, *Chip Scale Package: Design, Materials, Process, Reliability, and Applications*, New York : New York City, 1999.

- [126] M. Raimann, A. Peter, D. Mager, U. Wallrabe, and J. G. Korvink, "Microtransformer-based isolated signal and power transmission," *IEEE Trans. on Power Electronics*, vol. 27, no. 9, pp. 3996-4004, Sept. 2012.
- [127] J. Park and M. G. Allen, "Ultralow-profile micromachined power inductors with highly laminated Ni/Fe cores: application to low-megahertz dc-dc converters," *IEEE Trans. on Magnetics*, vol. 39, no. 5, pp. 3184-3186, Sept. 2003.
- [128] D. Flynn, A. Toon, L. Allen, R. Dhariwal, and M. P. Y. Desmulliez, "Characterization of core materials for microscale magnetic components operating in the megahertz frequency range," *IEEE Trans. on Magnetics*, vol. 43, no. 7, pp. 3171-3180, Jul. 2007.
- [129] S. Tang, S. Hui, and H. Chung, "A low-profile low-power converter with coreless PCB isolation transformer," *IEEE Trans. on Power Electronics*, vol. 16, no. 3, pp. 311-315, May 2001.
- [130] M. Brunet, T. O'Donnell, L. Baud, J. O'Brien, P. McCloskey, and S. C. O'Mathuna, "Electrical performance of microtransformers for dc-dc converter applications," *IEEE Trans. on Magnetics*, vol. 38, no. 5, pp. 3174-3176, Sept. 2002.
- [131] C. D. Meyer, S. S. Bedair, B. C. Morgan, and D. P. Arnold, "High-inductance-density, air-core, power inductors, and transformers designed for operation at 100–500 MHz," *IEEE Trans. on Magnetics*, vol. 46, no. 6, pp. 2236-2239, Jun. 2010.
- [132] R. Rassel and C. Hiatt, "Fabrication and characterization of a solenoid-type microtransformer," *IEEE Trans. on Magnetics*, vol. 39, no. 1, pp. 553-558, Jan. 2003.
- [133] K. Kratt, V. Badilita, T. Burger, J. G. Korvink, and U. Wallrabe, "A fully MEMS-compatible process for 3D high aspect ratio micro coils obtained with an automatic wire bonder," *J. of Micromechanics and Microengineering*, vol. 20, p. 015021, Jan. 2010.
- [134] A. Moazenzadeh, N. Spengler, R. Lausecker, A. Rezvani, M. Mayer, J. G. Korvink, and U. Wallrabe, "Wire bonded 3D coils render air core microtransformers competitive," *J. of Micromechanics and Microengineering*, vol. 23, p. 114020, Oct. 2013.
- [135] K. Yao and F. C. Lee, "A novel resonant gate driver for high frequency synchronous buck converters," *IEEE Trans. Power Electronics*, vol. 17, no. 2, pp. 180-186, Mar. 2002.

- [136] Y. Chen, F.C. Lee, L. Amoroso, and H. Wu, "A resonant MOSFET gate driver with efficient energy recovery," *IEEE Trans. on Power Electronics*, vol. 19, no. 2, pp. 470-477, Mar. 2004.
- [137] N. Z. Yahaya, K. M. Begam, and M. Awan, "A review on design considerations & limitations of resonant gate drive circuit in VHF operations," *Engineering Letters*, vol. 17, no. 2, pp. 54-62, 2009.
- [138] J. T. Strydom, M. A. de Rooji, and J. D. van Wyk, "A comparison of fundamental gate-driver topologies for high frequency applications," in *Proc. IEEE Applied Power Electronics Conf. and Expo.*, Feb. 2004, pp. 1045-1052.
- [139] Z. Yang, S. Ye, and Y. Liu, "A new resonant gate drive circuit for synchronous buck converter," *IEEE Trans. on Power Electronics*, vol. 22, no. 4, pp. 1311-1320, Jul. 2007.
- [140] Y. Lee and Y. Cheng, "A 580 kHz switching regulator using on-off control," *J. Inst. Electron. Radio Eng.*, vol. 57, no.5, pp. 221-226, Sep./Oct. 1987.
- [141] B. Song, X. Yang, and Y. He, "Class  $\Phi 2$  dc-dc converter with PWM on-off control," in *Proc. IEEE 8th Intel. Conf. on Power Electronics and ECCE Asia*, Jun. 2011, pp. 2792-2796.
- [142] H. Jung, S. Lee, and D. Jang, "Feasibility study on a new energy harvesting electromagnetic device using aerodynamic instability," *IEEE Trans. on Magnetics*, vol. 45, no. 10, pp. 4376-4379, Oct. 2009.
- [143] A. Bansal, D. A. Howey, and A. S. Holmes, "CM-scale air turbine and generator for energy harvesting from low-speed flows," in *Proc. Solid-State Sensors, Actuators and Microsystems Conf.*, Jun. 2009, pp. 529-532.
- [144] D. Rancourt, A. Tabesh, and L. G. Fr chette, "Evaluation of centimeter-scale micro windmills: aerodynamics and electromagnetic power generation," in *Proc. PowerMEMS*, 2007, pp. 93-96.
- [145] J. I. Seeger and B. E. Boser, "Charge control of parallel-plate, electrostatic actuators and the tip-in instability," *J. of Microelectromechanical Systems*, vol. 12, no. 5, pp. 656-671, Oct. 2003.
- [146] S. Paul, A. M. Schlaffer, and J. A. Nossek, "Optimal charging of capacitors," *IEEE Trans. on Circuits and Systems I: Fundamental Theory and Applications*, vol. 47, no. 7, pp. 1009-1016, Jul. 2000.
- [147] C. W. T. McLyman, *Transformer and Inductor Design Handbook, Third Edition*. Boca Raton: CRC, 2004.

## PUBLICATION

- [1] Y. Tang and A. Khaligh, "Bidirectional resonant dc-dc step-up converters for driving high-voltage actuators in mobile microrobots," *IEEE Trans. on Power Electronics*, in press (accepted).
- [2] Y. Tang and A. Khaligh, "A multi-input bridgeless resonant ac-dc converter for electromagnetic energy harvesting," *IEEE Trans. on Power Electronics*, in press (accepted).
- [3] Y. Tang and A. Khaligh, "Miniaturized bridgeless high-frequency resonant ac-dc step-up/step-down converters," *IEEE Trans. on Power Electronics*, vol. 29, no. 12, pp. 6518-6533, Dec. 2014.
- [4] Y. Tang, C. Chen, A. Khaligh, I. Penskiy, and S. Bergbreiter, "An ultracompact dual-stage converter for driving electrostatic actuators in mobile microrobots," *IEEE Trans. on Power Electronics*, vol. 29, no. 6, pp. 2991-3000, Jun. 2014.
- [5] H. Wang, Y. Tang, and A. Khaligh, "A bridgeless boost rectifier for low voltage energy harvesting applications," *IEEE Trans. on Power Electronics*, vol. 28, no.11, pp. 5206-5214, Jan. 2013.
- [6] Y. Tang and A. Khaligh, "A novel bridgeless high-frequency resonant ac-dc converter," in *Proc. IEEE Applied Power Electronics Conf. and Expo.*, Fort Worth, TX, Mar. 2014, pp. 125-130.
- [7] C. Chen, Y. Tang, A. Khaligh, and R. W. Newcomb, "A low-power and high-gain converter for driving dielectric elastomer actuators," in *Proc. IEEE Applied Power Electronics Conf. and Expo.*, Long Beach, CA, Mar. 2013, pp. 2755-2760.
- [8] Z. Yang, Y. Tang, P. Zeng, and A. Khaligh, "Reducing detent force while harvesting energy from center of gravity: an 11-poles, 12-slots generator design," in *Proc. IEEE Energy Conversion Congress and Exposition*, Sept. 2012, pp. 380-387.